2020

Spatial patterning in albedo and biogenic carbon exchange in urban areas

https://hdl.handle.net/2144/39878

Boston University

BOSTON UNIVERSITY

GRADUATE SCHOOL OF ARTS AND SCIENCES

Dissertation

SPATIAL PATTERNING IN ALBEDO AND BIOGENIC CARBON EXCHANGE IN URBAN AREAS

by

ANDREW LEE TRLICA

B.A., University of California at Berkeley, 2004
M.S., University of Washington, 2010

Submitted in partial fulfillment of the

requirements for the degree of

Doctor of Philosophy

2020

Approved by

First Reader
Lucy R. Hutyra, Ph.D.
Associate Professor of Earth & Environment

Second Reader
Mark Friedl, Ph.D.
Professor of Earth & Environment

Third Reader
Pamela Templer, Ph.D.
Professor of Biology

Fourth Reader
Nathan Phillips, Ph.D.
Professor of Earth & Environment

For my dad, who died early,

and Tony Janetos, who did too.

ACKNOWLEDGMENTS

I would like to first acknowledge the generous support, advice, and time provided by my committee members, Drs. Mark Friedl, Lucy Hutyra, Nathan Phillips, and Pam Templer, as well as the late Dr. Tony Janetos, who even after his cancer diagnosis was active in dissertation committee meetings into his final weeks. I would also like to thank Drs. Ian Sue Wing (who served as my examination chair), Rachael Garrett (now at ETH Zurich), Anne Short, Sally Brown (at the University of Washington), and Rachel Cook (at North Carolina State University) for their ongoing advice, fellowship, and inspiration in working through the PhD process over these years. I also wish to acknowledge the Pardee Center for the Study of the Longer-Range Future, the Hariri Center for Computing and Computational Science & Engineering, the Boston Area Research Initiative, the BU Initiative on Cities, the National Aeronautics and Space Administration (NASA) and the National Oceanographic and Atmospheric Administration (NOAA) for financially supporting this dissertation research.

I also must thank the many collaborators and teachers with whom I have had the benefit of working during the course of this research. This list includes my collaborators Jonathan Wang (now at UC Irvine), Crystal Schaaf and Angela Erb (UMass Boston), Ian Smith, Luca Morreale, Andy Reinmann (now at the City University of New York), Steve Raciti (now at Hofstra University), Steve Decina, and Dan O’Brien (Northeastern). My thanks also go to Drs. Curtis Woodcock and Josh Grey (now at North Carolina State University) for their roles as my formal instructors in the tools of satellite remote sensing. I could not have accomplished the computational and remote-sensing aspects of this

dissertation without the generous assistance of the many gifted practitioners at BU, including Drs. Eli Melaas, Damien Sulla-Menashe, Chris Holden, and Will Kearney, as well as the advice and tutelage of Jackie Getson and Keith Ma on the use of GIS and the shared computing cluster. I want to also specifically thank Dr. Alexey Shiklomanov, Dr. Conor Gately, and Betsy Cowdery at BU, who out of their own patience and time taught me to use the R programming language. I must also express my gratitude to the dedicated staff of the department, including Alissa Beideck Landry, Fred George III, Matt Dicintio, Lauren Consalvo, and Will Edwards, whose support at every step was indispensable.

I must finally offer my deepest gratitude to the people who formed the supportive intellectual community of which I was lucky enough to find myself a part at BU: The Biogeoscience Program and its students; Dr. Garrett’s Land and Food group; Drs. Valerie Pasquarella, Chloe Anderson, and Sarah Farron — Virgils through the underworld on countless occasions; the Earth & Environment graduate student community, including my cohort Alexey Shiklomanov, Radost Stanimirova, Paolo Arévalo, and Betsy Cowdery; the Hutyra group Luca Morreale, Sarah Garvey, and Julia Marrs; the brilliant path carved by the ones who came before me, including Kira Sullivan-Wiley, Drew Christ, Emily Schottenfels, Margaret Hendricks, Conor Gately, Brady Hardiman, Steve Raciti, Andy Reinmann, Jon Wang, Sarabeth Buckley, Eric Bullock, and Dan Gianotti; the fellowship of the graduate students across the street in the Department of Biology, including Nick, James, Nate, Tim, Lucy, and Johnny; my friends from the Pardee Summer Fellowship Kira, Sahar, Seulgie, Marta, Kristen, and Zoey, as well as Cynthia Barakatt and the other good people that keep the Center an active and inviting place; the Earth & Environment Graduate Student Association; and the Keeling Curveballs softball team.

I must finally express my humble gratitude to my partner Ana and to my friends and family, without whose love, encouragement, and support I could not have begun or finished this work.

SPATIAL PATTERNING IN ALBEDO AND BIOGENIC CARBON EXCHANGE IN URBAN AREAS

ANDREW LEE TRLICA

Boston University Graduate School of Arts and Sciences, 2020

Major Professor: Lucy R. Hutyra, Associate Professor of Earth & Environment

ABSTRACT

Urbanization alters surface energy and biogenic carbon (C) exchange processes which can exacerbate increases in near-surface temperature and complicate municipal-scale efforts to address the local causes and impacts of climate change. This dissertation integrates field- and remote-sensing datasets to evaluate the magnitude of and spatial patterns in albedo and biogenic C fluxes in the urban landscape, focusing on the region of Greater Boston, Massachusetts.

Using surface reflectance measurements from the Landsat and MODIS satellites, we show mean albedo in the Boston metropolitan region was significantly lower in core population centers than nearby rural areas, corresponding to reduced tree cover, greater impervious surface area, and higher surface temperatures. These results establish albedo decline as a gradient in landscape-scale features of urbanization, and offer context for efforts to mitigate extreme urban temperatures through raising the albedo of built surfaces.

Pairing field measurements of tree growth with LiDAR-based data on tree biomass and canopy cover, we estimate the distribution of annual woody biomass C uptake in the city of Boston. A substantial portion of tree C uptake occurred in densely developed residential areas dominated by open-grown trees as well as remnant forest fragments. Our results show that estimates based on rural tree growth may under-predict C uptake by up to approximately 50%, and quantifies the scope for policy interventions aimed toward increasing ecosystem services output from the urban forest.

Fusing measurements of soil respiration and net vegetation productivity in lawns and trees with high-resolution land surface data, we develop an improved estimate of annual biogenic net carbon fluxes in Boston at a 30 m resolution. We find forested areas of the city may be a modest net sink for C (median 2.7 GgC yr^{-1}), but also estimate substantial C flux from intensively managed landscapes in residential areas. Estimated city-wide biogenic C was relatively small (median 600 MgC yr^{-1}), potentially offsetting less than 1% of estimated annual fossil fuel emissions. Our results imply net biogenic C flux likely will contribute little towards efforts to reduce local net greenhouse gas emissions, but may significantly influence urban atmospheric CO_2 concentrations at certain times and places.

TABLE OF CONTENTS

ACKNOWLEDGMENTS v

ABSTRACT viii

TABLE OF CONTENTS x

LIST OF TABLES xiii

LIST OF FIGURES xvii

LIST OF ABBREVIATIONS xxii

CHAPTER ONE: Introduction and Overview 1

- 1.1 Dissertation Structure and Objectives 7

CHAPTER TWO: Albedo, land cover, and daytime surface temperature variation across an urbanized landscape 11

- *Abstract* 11
- 1. Introduction 12
- 2. Materials and Methods 17
  - 2.1 Data processing 18
  - 2.2 Statistical analysis 21
- 3. Results and Discussion 23
  - 3.1 Albedo distribution and effect of LULC class 23
  - 3.2 Albedo trends with land cover characteristics 25
  - 3.3 Data quality assessment 29

3.4 Regional effects of albedo on surface energy balance and LST........................30

3.5 Effect of spatial scale in analysis........................34

4. Conclusions........................36

Acknowledgments........................40

Supplemental Information for *Albedo, land cover, and daytime surface temperature variation across and urbanized landscape*........................49

CHAPTER THREE: Current and future biomass carbon uptake in Boston's urban forest........................60

Abstract........................60

1. Introduction........................61

2. Methods........................66

2.1 Study area geodata........................66

2.2 Tree growth data........................67

2.3 Growth modeling........................68

2.4 Policy Projections........................69

2.5 Statistical analysis........................70

3 Results and Discussion........................71

3.1 Urban forest structure and distribution........................71

3.2 Biomass gain in urban growth contexts........................72

3.3 Effect of biomass density areal basis........................74

3.4 Estimates of annual biomass C uptake........................75

3.5 Policy effects on ecosystem function........................76

4 Conclusions 79
Acknowledgments 82
Supplemental Information for *Current and future biomass carbon uptake in Boston's urban forest* 90
CHAPTER FOUR: Annual biogenic C exchange in an urban landscape 106
Abstract 106
1 Introduction 107
2 Methods 110
2.1 Data sources and processing 110
2.2 Carbon flux modeling 111
2.3 Statistical analysis 115
3 Results 115
4 Discussion 119
Acknowledgments 128
Supplemental Information for *Annual biogenic C exchange in an urban landscape* . 134
CHAPTER FIVE: Conclusions 146
5.1 Summary of work 147
5.2 Directions for future work 150
BIBLIOGRAPHY 155
CURRICULUM VITAE 181

LIST OF TABLES

Table 2.1: Day-of-year for scenes used in 30 m summer albedo. 47

Table 2.2: Results of spatial autoregressive GAM analysis of albedo versus land cover metrics (aggregated to 500 m). Mean modeled effect for each development intensity interval shown with central 95th percentile spread. 48

Table 2.S1: Within-pixel measures of variability (median ± 95% confidence interval) in white-sky albedo based on bootstrap resampling of 1,000 randomly selected pixels per LULC category. Column headings refer to the median number of separate observations represented, standard deviation, standard error of mean, median value, spread of central 95% of sample, and difference from the single-scene July 26, 2006 observation benchmark. 52

Table 2.S2: Median albedo (central 95-percentile) in single-day albedo data for bootstrap resampling of 1,000 randomly selected pixels per LULC category. 53

Table 2.S3: Fractional area of selected land-use/cover classes, presented with mean values for other land surface parameters at town scale for selected towns in the Boston study area (land cover metrics filtered for open water pixels prior to calculation of town-scale means). Abbreviations: IS, Impervious Surface %; LST, Land Surface Temperature; VL- L- M- H-DR, Very Low- Low- Medium- High-Density Residential; Ind., Industrial; Comm., Commercial; Trans., Transportation.54

Table 3.1: Estimated city-wide annual biomass C uptake, and distribution of median per-pixel rate of C uptake (central 95%). Relative areas of LULC types are Forest: 8%;

Developed: 38%; HD Resid.: 39%; LD Resid. 2%; Other Veg.: 11%; Water: 2%; Total area: 12,455 ha (See Table 3.S5). 89

Table 3.S1: LULC cover classes used in this study (MassGIS, 2005). 100

Table 3.S2: Model summaries for stem- and areal-basis growth rate. Values in parentheses show coefficient standard error. RSD indicates model residual standard deviance. * significant at p<0.05, ** significant at p<0.01, *** significant at p<0.001 by Chi-squared test versus model excluding the term. Significance of coefficients for Urban Forest plot annual growth tested via Student's t test (H_0: B_i=0), and RSD is indicated for model fit determined using mean model coefficients. Model intercepts were not evaluated for significant difference from zero. Random effects for stem annual growth were: Urban Forest – Plot, Stem ID (intercept + DBH slope); Street Trees – Taxon (intercept + DBH slope); Rural Forest – Plot, taxon, sample year (intercept). Radom effects for plot annual growth: Urban forest – none; Rural Forest – Plot, Sample year (intercept). 101

Table 3.S3: Rural and Urban Forest taxa present in stem DBH samples. All equations taken from Chojnacky et al. (2014) unless noted. Numbers in parentheses for Urban Forest indicate number of increment cores represented. Specific gravity (spg) in g cm^{-3}. 102

Table 3.S4: Street Tree taxa present in Street Tree sample, number of stems represented, and biomass allometric equations applied. Allometric equations taken from MacPherson et al. (2016), wood density from Zanne et al. (2009). 103

Table 3.S5: Land cover configuration in the Boston study area. 105

Table 4.1: Estimated map-wide biogenic C flux strength by LULC in Boston (median and central 95%). All figures in MgC ha^{-1} yr^{-1}, representing the sum of C flux for pixels of a given LULC divided by LULC area, summarized across model realizations. Negative values indicate flux of C from atmosphere, positive values represent flux of C to atmosphere..133

Table 4.S1: Total area (ha) of different cover types in the LULC classes used in this study. Fraction of total study area shown in parentheses. Tree biomass not shown. 141

Table 4.S2: Factors used to calculate components of biomass growth in open-grown and street tree records used in annual growth simulations (see Trlica et al. [2020]). Taxon-specific allometric equations (Northeast region) for aboveground wood volume, foliar biomass and factors for foliar dry weight (dw) were taken from McPherson et al. (2016), and wood density factors were taken from Zanne et al. (2009), except where noted. Root biomass was set to default of 0.28 of predicted aboveground biomass, following McPherson et al. (2016). Aboveground biomass was calculated via wood volume, predicted as volume (m^3) = B0*DBH^{B1}, with DBH in cm, except where noted..142

Table 4.S3: Total city-wide C flux by LULC (median and central 95% of estimates), GgC yr^{-1}. Negative values indicate net C sink, positive values indicate net C source. 144

Table 4.S4: Summary of metrics comparing forest biogenic C dynamics in >85% canopy covered pixels in Boston study region compared (by LULC and for Total map area),

and results of 15 years of field monitoring at Harvard Forest (HF) EMS site. Street refers to pixels modeled using alternative urban-specific allometric equations. Figures indicate median and central 95% of data except for HF, which shows mean and total range of reported observations. 145

LIST OF FIGURES

Figure 2.1: Data sources used in this study: A) Albedo (showing Massachusetts state outline and Interstate 495 study area boundary); B) Town municipal boundaries; C) Census-designated places (CDP); D) Tree canopy fraction (%); E) Impervious cover fraction (%); F) Population density (km^{-2}); G) Mean summer land surface temperature (°C). 41

Figure 2.2: Land cover features inside approximate MODIS 500 m pixel boundaries re-projected to UTM 19N (green box) in Watertown-Newton, MA (clockwise from top 42

Figure 2.3: Distributions of 30 m pixel values for albedo (top) and canopy fraction (bottom) across the most common land-use/-cover classes in the study area (Cropland, Forest, Forested wetland, Very low density residential, Low density residential, Medium density residential, High density residential, Multi-family residential, Commercial Industrial, Transportation, Water), representing approximately 84% of total area. Bar widths show relative frequency of class, dotted lines show medians for whole study area; pixels more than 1.5 times interquartile range beyond 1st and 3rd quartiles not shown. 43

Figure 2.4: Scatterplots of 30 m Landsat albedo values spatially aggregated to an approximate 500 m MODIS grid (excluding pixels classed as water), versus (clockwise from top left) canopy fraction, impervious fraction, land surface temperature (°C), and population density (km^{-2}, log scale). Shading shows pixel density; solid lines show cubic regression splines without spatial autoregressive

term; dotted lines show 95% confidence interval along a moving window; blue lines indicate pivot points along land cover metric according to GAM analysis accounting for spatial autocorrelation. Blue background dots show comparable 30 m pixel scatters with scales clipped to include central 99% of values. 44

Figure 2.5: Mean albedo versus (left) impervious fraction and (right) tree canopy fraction, Landsat 30 m data aggregated by town (selected towns labeled, open water pixels excluded). Color ramp corresponds to mean mid-morning land surface temperature, dot size corresponds to mean population density. 45

Figure 2.6: (L) Orthophoto Waltham (R) and Weston (L) Massachusetts approximately 64 km^2 (photo courtesy of Google Earth); (R) Unsupervised classification results for (a) 30 m albedo; (b) 500 m albedo; (c) 30 m LST; and (d) 500 m LST for the same region (excluding water). Scale bars show mean values for each cluster class (LST in °C). 46

Figure 2.S1: Scatterplots of 30 m values of albedo vs. (clockwise from top left) canopy fraction, impervious fraction, surface temperature (°C) and population density (km^{-2}, log scale). Shading indicates pixel density; solid lines indicate fitted cubic regression spline; dotted lines show 95% confidence interval of the albedo mean along a moving window. Scales are clipped to include central 99% of albedo values. 56

Figure 2.S2: Geary's *c* autocorrelation indices for albedo (left) and LST (right) for the full study area and scenes limited to the municipal boundaries of urban Boston and rural Berlin. 57

Figure 2.S3: Scatterplots of 500 m MODIS composite summertime albedo (excluding pixels with >10% area water), versus (clockwise from top left) canopy fraction, impervious fraction, land surface temperature (°C), and population density (km^{-2}, log scale), aggregated to the 500 m grid. Shading indicates pixel density; solid lines indicates fitted cubic regression spline prediction; dotted lines show 95% confidence interval of the albedo mean along a moving window. Blue background dots show comparable 30 m pixel scatters with scales clipped to include central 99% of values. 58

Figure 2.S4: Mean albedo versus (left) impervious fraction and (right) tree canopy fraction, MODIS 500 m data aggregated by town (selected towns labeled, pixels >10% water area excluded). Color ramp corresponds to mean surface temperature, dot size corresponds to mean population density. 59

Figure 3.1: Boston study area showing canopy distribution (green) and study area outline (image courtesy of Google Earth). 83

Figure 3.2: Land-use/land-cover and distribution of canopy area by distance from canopy edge in Boston study area. 84

Figure 3.3: Stem DBH and DBH increment for Rural Forest (L), Urban Forest (C) and Street Tree (R) contexts. Thick dashed lines show predicted mean response with fixed effects, thin dashed lines show central 95% of predictions given model error. 85

Figure 3.4: (A) Distribution of vegetation and cover in the study area; (B) Aerial photo of inset area in South End neighborhood (courtesy of USDA National Agriculture

Imagery Program); (C) Vegetation and cover type in inset: Canopy over pervious, canopy over impervious, non-vegetated impervious, non-vegetated pervious, vegetated pervious (non-canopy), and open water. Text figures correspond to features of inset area. 86

Figure 3.5: Pixel median biomass C uptake rate (MgC ha^{-1} yr^{-1}) for Hybrid Urban model (dark) and Rural Forest model, canopy basis (light). Box width is proportional to total area and show central 50% of data in each LULC category (other data not shown). 87

Figure 3.6: Median projections of annual net C uptake (top), total tree biomass (middle) and change in canopy area from 2006–2040 (bottom) in non-forested Developed, HD Residential, and LD residential pixels. Scenarios tested were Business-as-usual (BAU), Preserve Largest (PL) and Street Tree Planting (STP) from 2006–2040..... 88

Figure 3.S1: Example of identified plantable space (purple) along residential roads (gray), with space allowed for 4m buffer to nearest existing tree canopy (light green). 99

Figure 4.1: Median pixel estimate for NEE in city of Boston, MgC ha^{-1} yr^{-1}. Negative values indicate net C uptake, positive values indicate net C emissions. Pixel size is 30 m. 130

Figure 4.2: Distribution of per-pixel median estimated NEE (MgC ha^{-1} yr^{-1}). Inset shows relative areas of different LULC classes, and boxplot widths are also proportional to areas (Water values not shown).. 131

Figure 4.3: Median pixel Landsat July EVI (2010–2012) versus median pixel NEE estimate (MgC ha^{-1} yr^{-1}), by LULC. Color shading indicates concentration of pixel frequency. GAM prediction line shown in red. Bottom right shows histogram of pixel median NEE estimates for all LULC classes...132

LIST OF ABBREVIATIONS

ANPP	Aboveground Net Primary Productivity
AGWI	Aboveground Woody Increment
BAU	Business-as-usual
BRDF	Bi-directional Reflectance Distribution Function
C	carbon
CO_2	carbon dioxide
CDP	Census Designated Place
d	day
DBH	Diameter at Breast Height
ETM+	Enhanced Thematic Mapper
EVI	Enhanced Vegetation Index
GAM	Generalized Additive Model
g	gram
Gg	gigagram
GPP	Gross Primary Productivity
h	hectare
kg	kilogram
km	kilometer
km^2	square kilometer
LST	Land Surface Temperature
LULC	Land Use/Land Cover

m	meter
m^2	square meter
m^3	cubic meter
Mg	megagram/metric tonne
MODIS	Moderate Resolution Imaging Spectroradiometer
NDVI	Normalized Difference Vegetation Index
NEE	Net ecosystem exchange
NPP	Net primary productivity
PL	Preserve largest
R_s	Soil respiration
RSD	Residual standard deviance
SD	Standard deviation
SOC	Soil organic carbon
spg	Specific gravity
STP	Street tree planting
TM	Thematic Mapper
W	watt
yr	year

CHAPTER ONE: Introduction and Overview

Driven by population movements and economic development, urban land cover could by 2030 expand to triple its worldwide extent in 2000, posing multiple interrelated challenges for maintaining environmental quality and human well-being (Seto et al., 2012). Expansion of developed land cover is often the result of conversion of surrounding forest and cropland (DeFries et al., 2010; Olofsson et al., 2016), and can diminish the regional biogenic carbon sink (Hutyra et al., 2011; Imhoff et al., 2004; Zhao et al., 2012). Urban areas are also the demand sink for much of the world's materials and energy consumption and are host to concentrated outflows of greenhouse gases and other waste products (Dhakal, 2010; Kennedy et al., 2009). A better understanding of the changes in landscape-scale ecosystem function in urbanized areas is vital to predicting and managing the local and global environmental consequences of urbanization, and to supporting the health and well-being of the billions of people who will call cities home in the 21st century (Groffman et al., 2017)

Urbanization is a specific change in the terrestrial ecosphere occurring as part of the broader shift into the Anthropocene era, in which human activity has begun to affect the planet on geologic spatial and temporal scales (Zalasiewicz et al., 2010). As hybrid systems combining human artifacts and semi-spontaneous biophysical systems, urban areas can be conceptualized as "socio-ecological" systems that function in some cases radically differently from ecosystems under less intensive human impact (Golubiewski, 2012). Cities, for instance, host novel eco-evolutionary communities of species, experience altered weather patterns compared to surrounding rural areas, meld human and non-human materials and energy flows and regulatory processes, and may exhibit bioclimatic variability and a high degree of internal spatial heterogeneity, as well as cross-city homogeneity in certain landscape patterns and management routines (Alberti, 2015; Arnfield, 2003; Bai, 2016; Ossola and Hopton, 2018a; Polsky et al., 2014). Urban areas, in short, represent the replacement of less human-impacted ecosystems with ecosystems profoundly shaped by human activities and preferences. The ecosystem functions of urban areas are as a result both comparable to and critically different from rural and less human-dominated ecosystems. It is the goal of this dissertation to elucidate some of these functional shifts in the urban landscape, and better predict their implications for the future well-being of urban dwellers and the quality of their environment.

The first ecosystem function considered is surface energy exchange, and its influence on near-surface temperatures in urban landscapes. Conversion from vegetated surface to densely built impervious cover in cities is responsible for creating a suite of localized climate shifts, including generally warmer near-surface temperatures, termed the urban heat island (UHI) effect and noted nearly universally in cities (Rizwan et al., 2008). The UHI effect has been associated with wide-ranging changes in local weather patterns and plant phenology (Dixon and Mote, 2003; Melaas et al., 2016), and may offer a preview of future climate under more severe anthropogenic disruption (Meehl and Tebaldi, 2004). The local and regional climate impact of urban land conversion partly flows from alteration in the effective surface albedo (fraction of solar shortwave radiative energy reflected) due to both the introduction of darker building and road materials along with the effect of the complex vertical topography of the “urban canopy” in built-up cover (Fortuniak, 2008). Beside the immediate local effects of the UHI, albedo changes could be an important component of the total climate forcing effect of current and future urban land cover expansion (Bounoua et al., 2015; Reinmann et al., 2016). Conversely, the potential to counteract global and UHI temperature effects by albedo manipulation has been the subject of widespread discussion and numeric modeling studies (e.g. Akbari et al., 2012; Li et al., 2014; Vahmani and Ban-Weiss, 2016). However, though albedo is treated in numeric models of global and urban climate (Cheng and Byun, 2008; Falasca et al., 2016; Hafner and Kidder, 1999), few studies have empirically assessed the variability of land surface albedo across an urban-rural gradient, or examined the relationship of albedo to other land cover characteristics at spatial resolution below 500 m. Some 30 m-resolution work characterizing urban albedo has been conducted (Brest, 1987; Haashemi et al., 2016; Mackey et al., 2012), but to date no study had been made of the spatial variability of albedo, its potential controlling features in other land cover metrics, or its potential impact on surface temperature. A greater understanding of albedo variation across urban landscapes, and the land cover factors influencing albedo, could aid progress in estimating ongoing and future large-scale climate impacts due to expansion of urban centers (Barnes and Roy, 2010; Bounoua et al., 2015) and better inform studies on the possible effects of wide-scale urban albedo modification (Akbari et al., 2012).

The next ecosystem function to be considered uptake of atmospheric C to long-lived urban tree biomass, and the potential for policy-directed changes in tree C uptake and canopy cover. Though conversion of land from native vegetation cover to built-up development predictably lowers the overall vegetation density, developed areas may still retain and provide living space for considerable biomass (Hutyra et al., 2011; Raciti et al., 2012a) and corresponding capacity for biogenic C drawdown, potentially near to the undisturbed background in low-density development (Zhao et al., 2012). Many conditions that affect plant growth such as air quality, temperature, water availability, and nutrient availability and deposition can vary in urban areas in ways that both enhance (O'Brien et al., 2012) and degrade (Quigley, 2004) the relative growth rate of plants under urban conditions. Urban heat island temperature alterations can further affect tree growth rates (Searle et al., 2012) and the length of the growing season (Melaas et al., 2016). Moreover, vegetation density and net primary productivity (NPP) in developed areas can vary both positively and negatively relative to the local rural background depending on region and seasonal timing due to urban influences like supplemental irrigation and UHI effects on growing season length (Imhoff et al., 2004), and in combination with the effects of global climate change (Pretzsch et al., 2017). Field and experimental research in several urbanized regions has shown that, even under the combined influence of the many critical growth factors altered by the urban environment, tree productivity may often be enhanced (Briber et al., 2015; Gregg et al., 2003; Takagi and Gyokusen, 2004). Potentially corroborating these field findings, recent work based on MODIS observations of urbanized regions in China have suggested a nearly ubiquitous increase in Enhanced Vegetation Index (EVI) in developed areas over what would be expected based on vegetation areal losses due to development (Zhao et al., 2016). Reinmann and Hutyra's (2017) study based on field observations in the Boston area has suggested that the creation of broken canopy edges with development may impact biomass density and C uptake potential along these edge gradients due to greater light availability and temperature variability. It is thus becoming clear that the approaches of either treating urban regions as devoid of significant biomass (Kennedy et al., 2012; Running and Zhao, 2015) or as analogous to patches of undisturbed-forest-in-miniature (Reinmann et al., 2016) are likely insufficient to accurately assess the ecosystem function of vegetation in cities. Resolving uncertainty about underlying ecosystem processes like urban vegetation growth is critical to better understanding the spatial patterning of ecosystem services in cities, now widely considered a priority in both the science of urban ecology and in urban environmental policy (Niemelä, 2014).

The third ecosystem function to be considered was net biogenic C exchange and sequestration processes at work across the urban surface. Urban areas are host to large but variable fossil CO_2 emissions fluxes as well as biologically productive vegetation (Crawford et al., 2011; Velasco and Roth, 2010). Cities are leading the way in efforts to reduce carbon emissions, yet effective emissions policies will require increasingly sophisticated means of monitoring and attributing urban C flux components resolved in both space and time (Gately and Hutyra, 2017; Hutyra et al., 2014; Pataki et al., 2006). There is also an abiding interest among urban policymakers in offsetting local fossil C emissions to help meet climate change mitigation goals, including through local forest C uptake (Poudyal et al., 2010). However, both fossil C emission and biological C exchange processes in the urban landscape vary strongly across short spatial and temporal scales, posing challenges for accurately measuring, modeling, or attributing fluxes in the urban atmosphere. Moreover, though biogeochemical processes are an important aspect of the land-atmosphere C exchange in urbanized landscapes (Hardiman et al., 2017), lessons drawn from research in less intensively impacted areas may not map neatly onto seemingly comparable processes at work in cities. Effectively monitoring emissions from cities will require the modification of existing approaches and development of new techniques that can accurately parse in space and in time not only fossil C emissions sources, but also biological uptake and release processes, as well as account for the unique conditions, heterogeneity, and human interventions that prevail in the urban ecosystem. A variety of approaches have been used to measure and attribute fossil and biogenic C flux in urban environments, including eddy covariance measurement campaigns (Velasco and Roth, 2010), bottom-up inventorying (Gately et al., 2013; Raciti et al., 2012a; Strohbach et al., 2012) and atmospheric inversion modeling (McKain et al., 2012; Sargent et al., 2018), but all face difficulties in accurately estimating any spatially and/or temporally resolved biogenic C flux contributions to overall C exchange. Hardiman et al. (2017) modeled biogenic C exchange in the urbanized Boston region while taking into consideration factors such as impervious cover (Raciti et al., 2012b) and localized UHI temperature effects (Wang et al., 2017), but it remains unclear how well approaches based on coarse spatial resolution and calibrations derived from rural forest monitoring can be cleanly applied to urban landscapes. Adding increasing complexity, recent research in the Boston metropolitan region has shown that human modifications to N and organic matter deposition in urban soils may significantly alter the pattern and scale of organic matter distribution and the rate of soil C respiration (Decina et al., 2016; Templer et al., 2015). Other urban biogenic C budgets, where they have been attempted, lack either spatial or temporal resolution and have not taken edge- and management-related effects on plant productivity and ecosystem respiration into account (Nowak et al., 2013).

1.1 Dissertation Structure and Objectives

To address some of these key gaps in our understanding of urban ecosystem function, the research of this dissertation seeks to examine metrics of selected ecosystem functions across a highly urbanized landscape. Treating the city foremost as an ecosystem, these studies work to resolve and describe variation in functional indicators in space through a combination of publicly available geospatial data sets and field measurements taken as parts of other studies.

In Chapter 2 we quantified the variation of albedo across an urbanized region using remote sensing data, and explored its relationship to land surface temperature and other land cover metrics (Trlica et al., 2017). This study focused on the contiguous area of municipalities between Interstate 495 and Boston, Massachusetts, USA. A 30 m Landsat-based surface albedo map (Shuai et al., 2011) and land surface temperature map (Sobrino et al., 2004) prepared by our co-authors was combined with geospatial data on tree canopy fraction, impervious surface fraction, daytime population density (1 km), land-use/land-cover (LULC) classification, and town municipal boundaries. Data were filtered to remove "Water" classed pixels and were examined at several spatial scales, with coarser analysis performed by aggregating the 30 m data to 1) the approximate boundaries of the MODIS 500 m grid, and 2) the boundaries of the municipalities that made up the study area. Generalized additive modeling of the relationship between albedo and the other surface parameters at 30 m showed weak correlation due to intrinsically high heterogeneity in the landscape. Aggregating data to 500 m showed clear trends of lower albedo at the upper end of the range of indicators of urbanization (reduced canopy, increased impervious cover, and increased population density). Aggregated to town-boundaries, there were strong linear associations between reduced albedo in the most densely populated, impervious, and devegetated parts of the metropolitan region. In contrast to the 30 m albedo data, the independent 500 m MODIS observations still apparently contained significant signal from nearby open water even after carefully excluding pixels with partial water exposure. Overall, the most intensively urbanized parts of the Boston metropolitan region had albedo that was 0.035 lower than the most rural segments, and was associated with mid-morning surface temperature increases 12.6 degrees higher. This study provides important empirical boundaries for the albedo of highly developed landscapes, and verifies the general supposition that greater sunlight absorption in urban areas is likely a partial cause of the local urban heat island.

In Chapter 3 we estimated annual carbon uptake to long-lived woody tissues across the highly urbanized landscape of Boston on a spatially explicit basis, as well as the future consequences of differing municipal policy affecting tree mortality and planting through 2040 (Trlica et al., 2020). Using a previously developed 1 m-map of tree canopy and biomass (Raciti et al., 2014), and local field measurements of tree growth rates in a variety of contexts, this work estimated C uptake at a 30 m grid resolution while also accounting for empirical forest edge growth enhancement and the faster growth rates measured in open-grown street trees. Our results showed that when modeled based on local growth measurements, urban forest C uptake was approximately double the estimate based on growth rates derived from rural forest measurements. High-density residential neighborhoods hosted a large fraction of the total biomass and annual C uptake of the city. Another large portion of annual C uptake took place in smaller areas of forest fragments which tended to have higher C uptake rate per m^2, though some non-forest areas contained comparable tree C uptake rates. A large majority of canopy area within the Boston city limits was within 10 m of a canopy edge, and thus subject to potentially higher growth rates. Overall C uptake to long-lived biomass was a small fraction of estimated annual fossil C emissions. However, policy was capable of maximizing differing ecosystem functions, with greater overall standing biomass and canopy expansion by 2040 under a policy of reducing large-tree mortality, versus greater annual C uptake rate achievable by expanding street tree planting in available road buffer areas. Our results showed that a large fraction of urban forest C uptake likely takes place in the scattered canopy setting of residential neighborhoods. Our study further implied that “green infrastructure” policy focused exclusively on ecosystem function in parks, forests, and other recognizable green spaces is likely to be limited in in effect compared to policy that deals with urban trees in non-forest locales.

In Chapter 4 we followed up on the work of Chapter 3 in constructing a model of total photosynthetic C uptake in both trees and turf grass, as well as an estimate for management-sensitive rates of soil respiration, to estimate net ecosystem exchange (NEE) at 30 m resolution across the city of Boston. Net C uptake in tree woody biomass, roots, and leaves was estimated via urban-specific allometric equations, while uptake to turfgrass lawns was modeled based on measured carbon exchange reported for other studies of in turfgrass systems. Soil respiration was estimated following the work of Decina et al., (2016) the same region, using high-resolution data on land-use/land-cover and other surface characteristics to allocate soil respiration efflux factors. We estimated an insignificant NEE C sink for the city as a whole. Forest-classed areas acted as a net C sink while residential areas acted as a net C source. This partitioning was largely due to the high efflux of C with soil respiration from landscaped areas or residential zones. Non-residential developed areas were predicted to host relatively low biogenic C fluxes in general. On a spatial basis, estimated NEE was not reliably related to satellite metrics of vegetation cover (EVI), even when accounting for land-use/land-cover. This lack of relationship was due in part to both significant and spatially heterogeneous differences in plant productivity and soil respiration flowing from altered urban ecosystem function that were not directly revealed by vegetation density alone. Our work implied that urban policy geared towards maximizing local biogenic carbon sequestration is unlikely to play a significant role in offsetting current local fossil fuel C emissions without significantly increasing the amount of Forest-classed land cover.

Together these studies advance our understanding of ecosystem function in the highly modified conditions characteristic of today’s urban regions. These studies also provide empirical grounding for understanding the spatial arrangement of key ecosystem function in the city, and highlight remaining needs for data and analysis to better inform decisions touching on the management of these ecosystems to promote the well-being of their inhabitants.

CHAPTER TWO: Albedo, land cover, and daytime surface temperature variation across an urbanized landscape

Abstract

Land surface albedo is a key parameter controlling the local energy budget, and altering the albedo of built surfaces has been proposed as a tool to mitigate high near-surface temperatures in the Urban Heat Island. However, most research on albedo in urban landscapes has used coarse-resolution data, and few studies have attempted to relate albedo to other urban land cover characteristics. This study provides an empirical description of urban summertime albedo using 30 m remote sensing measurements in the metropolitan area around Boston, Massachusetts, relating albedo to metrics of impervious cover fraction, tree canopy coverage, population density, and land surface temperature (LST). At 30 m spatial resolution, median albedo over the study area (excluding open water) was 0.152 (0.112–0.187). Trends of lower albedo with increasing urbanization metrics and temperature emerged only after aggregating data to 500 m or the boundaries of individual towns, at which scale a -0.01 change in albedo was associated with a 29 (25–35)% decrease in canopy cover, a 27 (24–30)% increase in impervious cover, and an increase in population from 11–386 km-2. The most intensively urbanized towns in the region showed albedo up to 0.035 lower than the least urbanized towns, and mean mid-morning LST 12.6°C higher. Trends in albedo derived from 500 m MODIS measurements were comparable, but indicated a strong contribution of open water at this coarser resolution. These results reveal linkages between albedo and urban land cover

character, and offer empirical context for climate resilient planning and future landscape functional changes with urbanization.

1. Introduction

By 2030, urban land cover could expand to triple its extent in 2000, posing multiple interrelated challenges for maintaining environmental quality and human well-being (Seto et al., 2012). Expansion of developed land cover may result in surrounding forest lost (DeFries et al., 2010; Olofsson et al., 2016), diminish the regional biogenic carbon sink (Hutyra et al., 2011; Imhoff et al., 2004), and enhance flooding and stream nitrogen export (Benson-Lira et al., 2016; Groffman et al., 2004). Conversion from vegetated surface to densely built impervious cover is responsible for creating a suite of localized climate shifts termed the urban heat island (UHI) effect, noted nearly universally in cities (Arnfield, 2003; Rizwan et al., 2008). The UHI effect has been associated with wide-ranging changes in local weather patterns and plant phenology (Dixon and Mote, 2003; Krehbiel and Henebry, 2016; Melaas et al., 2016; Zhang et al., 2004), increased hazards to health and quality of life for urban residents (Johnson and Wilson, 2009; Patz et al., 2005), and may offer a preview of future climate under more severe anthropogenic disruption (Meehl and Tebaldi, 2004). The simultaneous expansion of urban land and the ongoing effects of global climate change stands to further expand UHI areas and the number of people affected by extreme temperatures (Georgescu et al., 2012).

The local and regional climate impact of urban land conversion partly flows from alteration in the effective surface albedo (fraction of shortwave radiative energy reflected) due to both the introduction of darker building and road materials along with the effect of the complex vertical topography of the “urban canopy” in built-up cover (Fortuniak, 2008; Kondo et al., 2001). Effective surface albedo can vary at fine spatial scales across the urban landscape as a consequence of the differential influences of cover features like buildings, roads, parks, and urban forests. Decreases in albedo increase radiative energy absorption by the urban land surface, contributing to increases in air and surface temperature that characterize the UHI (Peng et al., 2012; Taha, 1997; Zhou et al., 2014). Beside the immediate local effects of the UHI, changes in land surface albedo with urban development may alter the regional surface energy balance and climate more broadly (Barnes and Roy, 2010), and could be an important component of the total climate forcing effect of current and future urban land cover (Bounoua et al., 2015; Reinmann et al., 2016). Conversely, the potential to counteract global and UHI temperature effects by albedo manipulation, for instance through using more reflective materials on roofs, has been the subject of widespread discussion and numeric modeling studies (Akbari et al., 2012; Jacobson and Ten Hoeve, 2012; Li et al., 2014; Vahmani and Ban-Weiss, 2016).

Numeric models of global and urban climate have incorporated albedo variation using coarse-scale remote sensing measurements (Hafner and Kidder, 1999), by assuming generalized albedo values for different cover categories (Argüeso et al., 2014; Cheng and Byun, 2008), by explicitly modeling solar energy absorption and exchange in the “urban canopy” (Oleson et al., 2008), or a combination of these approaches (Ban-Weiss et al., 2015; Georgescu et al., 2012; Li et al., 2014; Taha, 2008). Studies of the UHI using remote sensing data at <3 m resolution is becoming increasingly possible (Zhang et al., 2016), and retrieval of urban albedo is possible at similar resolution (Kaplan et al., 2016).

Incorporation of high-resolution albedo and other land cover data, such as vegetated and impervious fractional coverage, into urban surface energy exchange models has been shown to improve agreement with observed surface temperature and evapotranspiration flux (Vahmani and Hogue, 2014), and current large-eddy models rely on land cover parameters, including albedo, specified at high spatial resolution (Falasca et al., 2016). Recent work has used very high-resolution remote sensing data to characterize albedo variation among different roof styles to improve urban climate model accuracy (Ban-Weiss et al., 2015).

However, few studies have empirically assessed the variability of land surface albedo across an urban-rural gradient, or examined the relationship of albedo to other land cover characteristics at spatial resolution below 500 m, the scale at which urban land variability and land conversion tends to occur. Point measurements from tower or aerial observations over urbanized landscapes often show lower values in more densely developed locations (Christen and Vogt, 2004; Taha, 1997). Remote sensing-based descriptions of urban albedo have characterized albedo for different LULC classes or identified similar broad declines in albedo in "urban" areas using coarse spatial resolution data, but may also obscure variability across urban areas and details of urban land cover changes over time. Land cover variation often occurs at scales smaller than the 500 m to km range examined in many urban remote sensing studies (Jin and Roy, 2005; Zhou et al., 2014). Higher-resolution studies of urban land cover and surface temperature, often using remote sensing data at 30 m or less resolution, have often not considered albedo (e.g. (Connors et al., 2013; Herold et al., 2005; F. Kong et al., 2014; Zhang et al., 2016). Early high-resolution work characterizing urban albedo by Brest (1987) used Landsat 30 m reflectance to approximate broadband albedo (assuming a simplified Lambertian bi-directional reflectance distribution function, BRDF) in several land cover categories for Hartford, Connecticut. Other studies have examined albedo at high resolution only as it related directly to LST. For instance, a study in Phoenix, Arizona found negative correlation between broadband (Lambertian) albedo and nighttime LST based on 7 m observations, but the linkages between albedo and other land cover metrics were not considered (Jenerette et al., 2016). Mackey et al. (2012) used Landsat 30 m surface reflectance (without specifying surface BRDFs) to estimate broadband shortwave albedo across the Chicago area, finding land surface temperature reductions with greater NDVI and higher albedo, but also did not evaluate albedo covariance with other land cover metrics. Haashemi et al. (2016) found comparable results for LST in Tehran, Iran, using similar Landsat-based albedo estimates. Small (2006) used spectral mixture analysis of Landsat 30 m multispectral data over several cities to describe urban surfaces using the fraction of vegetation, high-albedo "substrate" (soil, pavement, rock), and a "dark" end-member classes. While this work showed a clear inverse relationship of temperature with vegetation fraction, the separate effects of albedo on LST could not be determined as the substrate and dark end-members convolved the underlying albedo signature, as well as potentially combining in the dark end-members the effects of several cover types (absorptive surfaces, shadows, water) with radically different biophysical properties.

There is little empirical work available to guide estimates in how albedo may change with urban expansion, and there has been little investigation into the nature of the spatial correspondence of albedo to other land cover metrics. The lack of high-resolution study into the nature of albedo variation across urbanized areas hinders progress in understanding the landscape functional changes produced by urbanization and in modeling surface energy balance shifts under expanded urban land cover. For instance, (Reinmann et al., 2016) used 500 m MODIS broadband shortwave albedo observations to predict future regional-scale changes in surface energy balance in Massachusetts, USA, due to urban expansion, but projections based on these estimates might have been affected by ambiguities in associating albedo values with different settlement density as well as artifacts in the albedo observations over the urban surface on the order of tens of meters. A greater understanding of albedo variation across urban landscapes, and the land cover factors influencing albedo, could aid progress in estimating ongoing and future large-scale climate impacts due to expansion of urban centers (Barnes and Roy, 2010; Bounoua et al., 2015) and better inform studies on the possible effects of wide-scale urban albedo modification (Akbari et al., 2012). Improved understanding the distribution in albedo across urban regions may also on a more local basis improve the ability to to target and scale feasible approaches for surface modifications to mitigate UHI impacts.

The goal of this study was to improve upon previous course-resolution studies of urban albedo with high-resolution geospatial data to quantify urban summertime albedo at 30 m resolution, and to relate these albedo measures to descriptive metrics of urban land cover character (canopy cover, impervious fraction, and population density) and mid-morning summertime LST. The results of this study provide an empirically driven picture of urban albedo based on high-resolution data, as well as an empirical model of drivers of albedo variation in urban land cover and its relation to one aspect of land surface temperature variations.

2. Materials and Methods

The study region was defined as the contiguous area of town boundaries for all municipalities between downtown Boston, Massachusetts, USA, and the Interstate 495 highway that circumscribes the central city at a distance of approximately 50 kilometers (Figure 2.1), a landscape that has experienced considerable forest clearance with expansion of low density development on the periphery of the older urban centers (Olofsson et al., 2016). The study area covered approximately 6,600 km^2 containing 4.2 million residents in the 2010 census, and encompassed the broad range of biological and physical surface features commonly present in this heavily settled region of southern New England.

Geospatial data products included in the analysis were surface albedo, tree canopy fraction, impervious surface fraction, daytime population density, land surface temperature, land-use/land-cover (LULC) classification, census designated places (CDP), and town municipal boundaries. All geospatial data was projected to the local UTM coordinate system and resampled to a common raster grid with 30 m resolution to match the resolution of the albedo measurements.

Given the large seasonal changes in tree canopy cover that occur in this temperate urban environment (Melaas et al., 2016), data on surface features were combined only from daytime measurements made between June 1–August 31 to focus on a period of stable plant phenology combining the effects of maximum leaf extent and minimal snow cover, while also capturing the maximum summertime surface temperature anomaly associated with the UHI (Hu and Brunsell, 2013).

2.1 Data processing

Albedo measurements were retrieved for scenes covering the study area for June 1–August 31 (DOY 152–243) from 2003–2008 (Table 2.1). Surface shortwave broadband albedo were downscaled to 30 m resolution by synthesis of Landsat 7 ETM+ top-of-atmosphere reflectance observations occurring at approximately 10:20 local time (following Shuai et al. [2011]) and the V005 16-day MODIS BRDF product (Schaaf et al., 2002). Radiometric data for each Landsat scene were processed for calibration and atmospheric correction using the Landsat Ecosystem Disturbance Adaptive Processing System (LEDAPS) (Masek et al., 2006) (excluding scenes with >80% cloud cover) and then screened for clouds using Fmask (Zhu et al., 2015). Both “white-sky”/bihemispherical and “black-sky”/directional hemispherical (with solar zenith angle at the time of overflight) were calculated for each pixel using the MODIS BRDF parameters. Albedo values for the Landsat shortwave narrow bands were converted to “broadband” (0.4–2.5 μm) values using the conversion coefficients of (Liang, 2001). Final broadband albedo retrievals were filtered to include values based only the highest two quality classes of concurrent MODIS BRDF retrievals. Albedo values under both white- and black-sky assumptions were combined using the median value for each pixel across all view dates to minimize the effect of extreme outliers (such as from incorrectly unfiltered cloud or cloud shadow pixels). A final “actual” albedo value per pixel under typical summer solar diffuse fraction illumination conditions for the Boston region was calculated as a function of black- and white-sky values (Shuai et al., 2011), weighed assuming a diffuse fraction of 0.558, the long-term average of June–August 2002–2008 solar illumination observations at Logan Airport (NSRDB, 2010). The six-year summer-only compositing window was used to collect enough measurements per pixel to obtain a reliable albedo estimate while being minimally vulnerable to major changes in land cover character due to land conversion or large phenotypic variation across seasons. A similar broadband "actual" albedo of the study area was produced using the MODIS 500 m V005 16-day albedo MD343A3 data product (Schaaf and Wang, 2015) with scenes from the same June–August 2003–2008 window as the Landsat albedo data, projected into the local UTM system and retaining only values using the two highest quality classes of BRDF retrievals. MODIS 500 m albedo data were filtered to exclude pixels with >10% areal coverage of open water using the LULC data layer. Analysis of the precision of individual albedo estimates across Landsat acquisition dates is presented in Supplemental Information.

Tree canopy fraction corresponding approximately to the year 2010 was obtained from the 30 m National Land Cover Database tree canopy product (Homer et al., 2015). Canopy fraction was used in preference to a vegetation index (e.g. NDVI) because fractional vegetation cover has been shown to correspond empirically and functionally more directly to temperature effects in the UHI (Weng et al., 2004). Impervious surface cover classification (as binary impervious/non-impervious) generated from orthophotography data was aggregated to 30 m pixels from a 1 m grid by mean value per pixel in the reference grid (MassGIS, 2005). Daytime population density on a 1 km grid was downscaled by nearest neighbor to the 30 m reference grid (Bright et al., 2013). Land surface temperature was derived from mid-morning summertime observations from Landsat 5 TM (120 m) and Landsat 7 ETM+ (60 m) thermal infrared measurements that were corrected for atmospheric effects using MODTRAN (Barsi et al., 2005), after cloud masking using Fmask (Zhu et al., 2015). Downscaling to 30 m was performed by calculating LST using emissivity values based on surface reflectance data indicating fractional cover of soil, vegetation, and impervious cover at 30 m (Sobrino et al., 2004) similar to Melaas et al. (2016), averaged using mean pixel values across all valid retrievals. A thematic land-use/land-cover (LULC) map based on 2005 aerial orthophotography was rendered as a 30 m raster and aligned with the albedo reference grid, with land cover classed according to maximum combined LULC category area per pixel (MassGIS, 2005). Inside the study area the boundaries of the towns making up the study area and the Census-Designated Places (CDP), identified by the Census as named settled development concentrations, were rendered as 30 m rasters aligned with the reference grid (MassGIS, 2005; U.S. Census, 2010). All rasters were registered to features in the albedo layer using an automated 0th order polynomial transformation in ArcMap and inspected visually for fit. Approximately 7.3M pixels on the 30 m grid were included in the study area.

Conversion of the LULC delineation map to raster, data registration, and some figure production was conducted in ArcMap (ESRI, 2014). All other data processing and analysis was performed using the R software application (R Core Team, 2014) and the packages *mgcv* (Wood, 2011), *raster* (Hijmans, 2017), *regeos* (Bivand and Rundel, 2015) and *rgdal* (Bivand et al., 2015)

2.2 Statistical analysis

Due to heteroscedacity of the data distributions, results are presented with 95% central quantile spreads (2.5–97.5th percentile) based on the mean of bootstrap resampling (1,000 resamples). A generalized additive modeling (GAM) approach using a cubic regression spline algorithm was used to fit models for the relationship between albedo and the other surface parameters on a pixel-by-pixel basis (Faraway, 2006). Population density was log-transformed before analysis to correct for non-normal distribution after adding 0.5 to represent values of 0. Spatial autocorrelation in the raster data was evaluated at scale lags of 30–1200 m using the Geary's *c* statistic, applying a Rook's Rule spatial weighting. An additional spatial autoregressive parameter in each GAM was included as the interaction of the pixel coordinates to explicitly model the spatial dependency of the dependent variable. For analysis, GAM pivot points were identified by changes in the sign of the modeled effect. Albedo, temperature, and other land cover characteristics were also examined according to their LULC delineations and position relative to CDP boundaries. Data at 30 m were filtered to remove "Water" classed pixels (approximately 267,000 pixels, 3.7% of the study area) prior to spatial aggregation to reduce the influence of the relatively low-albedo water pixels. This approach allowed a focus on the influence of non-water land cover features on albedo, which have been presumably more subject to shorter-term alteration with human development activities (approximately 7.1M valid pixels). Univariate relationships between albedo and the other land cover metrics at the town scale were examined using an orthogonal distance regression approach to account for error in both variables, presenting both the mean regression coefficients and their confidence intervals determined based on 1,000 bootstrap resamples, and R^2 values for the line of best fit estimated based on deviation in the y-direction only.

Univariate trends across isolated metrics of surface characteristics or land cover may not adequately capture the nature of interactions among of cover characteristics, which are often strongly covariant (Li and Weng, 2005; Nowak and Greenfield, 2012; Wu, 2004; Zheng et al., 2014), nor allow a consideration of the effect of spatial co-location of surface features in influencing the albedo signature. Spatial autocorrelation of urban surface features and temperature anomalies may also be very strong at high spatial resolutions, obscuring relationships among cover properties that may only emerge at a scale of hundreds to thousands of meters (Song et al., 2014). To examine broader scale patterns in albedo and the other land cover metrics, data were examined at several spatial scales, with coarser analysis performed by aggregating the 30 m using the mean of values of pixels contained within 1) the approximate boundaries of the MODIS 500 m albedo pixels projected to the local UTM system, and 2) within the boundaries of the towns that made up the study area. Analysis at the scale of the MODIS 500 m albedo data allowed a direct comparison of albedo trends between the 30 m Landsat and 500 m MODIS albedo data sets (though it has been noted that the MODIS 500 m BRDF/Albedo product in practice incorporates signal from a somewhat larger area encompassing adjacent pixels (Campagnolo et al., 2016). The boundaries of the towns constituting the study area, while somewhat arbitrary with respect to land cover features, are at a scale likely to reduce the effects of spatial autocorrelation due to scale mismatch between the observations and underlying phenomena, as well as better capture some of the effects of pixel proximity, zoning similarities, and development history, showing broader region-wide patterns in the spatial distribution of land cover and LST features. Spatial clustering patterns of both albedo and LST were also examined by performing separate k-means unsupervised classification, with five final categories, on the albedo and LST data at both the 30 m and 500 m scales.

Many of the differences and trends explored in this study were small, at the scale of approximately 1% within a highly variable classes of urban landscape. The stated accuracy of the underlying MODIS albedo/BRDF retrievals used to estimate the 30 m albedo values used in this study is globally ±5%. Studies have shown root mean-square error in BRDF retrievals of 1–2%, particularly in snow-free regions and where multiple high-quality BRDF retrievals are available (Shuai et al., 2008). Similarly, the accuracy of the MODIS retrievals against tower-based albedo measurements in relatively homogenous natural sites in North America were near 1% (Román et al., 2013). Therefore, though accuracy of below approximately 1% has been demonstrated in the MODIS BRDF product, the small scale of the albedo differences in this study, compared to the stated 5% accuracy of the data products on which it relies, a specific assessment of the precision of these data was performed to evaluate their appropriateness for detecting such low magnitude differences.

3. Results and Discussion

3.1 Albedo distribution and effect of LULC class

Based on 30-m estimates, the median summer albedo in the greater Boston study area was 0.151 (0.053–0.187) with an overall range of 0.007–0.851 and a negative skew. Median albedo excluding water pixels was 0.152 (0.112–0.187). This albedo estimate was comparable to the urban average value of 0.112 reported for 1 km albedo estimates from measurements by the Advanced Very High Resolution Radiometer (Strugnell and Lucht, 2001), and 0.157 for U.S.-average albedo values in urban cover based on 500 m MODIS readings (Barnes and Roy, 2010). Median albedo for the study area was also similar to aerial measurements over other temperate-zone cities such as 0.12–0.20 for Los Angeles; 0.12–0.13 for Hamilton, Ontario; 0.13–0.15 for Vancouver, British Columbia; and 0.16 for Munich, Germany, but differed substantially from cities such as Lagos, Nigeria, with albedo of 0.45 (Taha, 1997). Median albedo for the Boston study area was also somewhat lower than recent Landsat-reflectance based values of 0.21–0.24 reported for the semi-arid city of Tehran, Iran (Haashemi et al., 2016), and the 0.152–0.181 reported for mesic Chicago, Illinois (Mackey et al., 2012), but higher than Landsat-based summertime values of 0.105–0.147 reported for the urban core of mesic Hartford, Connecticut (Brest, 1987). The higher resolution of the 30 m albedo data captured considerably more of the intrinsic albedo variability due to short-scale differences in land cover compared to the coarser-resolution MODIS 500 m dataset (Figure 2.2).

The range of observed albedo by land cover category showed large variability, with median albedos within -12 to +14% of the whole-area median among 11 common land cover types (occupying approximately 80% of the study area) (Figure 2.3). The exception was open water, which showed a low median albedo at 0.031 (0.016–0.151). Three common "non-developed" LULC classes (Forest, Forested Wetland, and Cropland) had median albedo slightly higher than the whole-area median albedo, while the ranges of albedo in selected "developed" use classes did not differ greatly from the whole-area median. Median albedo declined 0.017 from the least- to most-dense residential classes, but albedo distributions in other types of non-residential developed land were comparable to one another. The small differences in albedo between LULC classes were not generally paralleled in the other land cover metrics (e.g. canopy fraction), which showed more distinct differences between use classes. Canopy fraction, for instance, was highest in forested LULC types, near the whole-area mean in the lowest residential density classes, and declined with higher residential densities towards values similar to other developed classes. The large overlap in the range of albedo between LULC classes may be due to the variable biophysical character of land cover present in these broad categories, variable effects of shadowing with built-up surface texture, and the potentially variant spatial scale of clustering or dispersion within the same or similar LULC categories. For instance, pixels in the same LULC category associated with high urbanization intensity might include discontinuous areas containing dark or highly reflective roofs, parking lots, and small areas of tree and grass plantings that are integrated into a single albedo value in coarser 500 m measurements (Figure 2.2). Differences in albedo were negligible between pixels within CDP boundaries (median 0.149, 0.069–0.187) and pixels outside CDP boundaries (median 0.153, 0.044–0.187), which may also reflect the same integration of albedo values from widely differing land cover character inside and outside of designated built-up areas.

3.2 Albedo trends with land cover characteristics

At 30 m resolution, even after exclusion of low-albedo open water pixels, variability was very high and relationships between albedo and other land cover metrics were ambiguous and weak (Figure 2.S1). A GAM including a spatial autocorrelation term for 30 m albedo predicted by canopy, impervious fraction and population density explained 11.1% of total deviance with all terms significant ($p < 0.01$), while a model including only the spatial autoregressive term explained 6.5%. However, when data were aggregated to a coarser 500 m spatial grid (consistent with MODIS pixel size, but excluding water), somewhat clearer trends toward lower albedo with greater indicators of urbanization intensity emerged (Figure 2.4). A spatial autoregressive GAM for the combined effect of canopy, impervious fraction, and population density on albedo explained 36.3% of deviance ($p<0.01$ for all terms), while a model including only the spatial autoregressive terms explained 22%. Univariate GAM analysis including spatial autocorrelation showed small but significant effects across urbanization metrics (Table 2.2). None of the land cover metrics individually or together had a determinative influence over albedo independent of landscape position, but models all predicted lower albedo with greater indicators of urbanization (i.e. higher impervious fraction, lower canopy fraction, higher population density). Modeled effects were modest in the low and medium-intensity development ranges, but were considerably greater in magnitude at the upper extremes of development intensity. The models also predicted lower albedo with impervious fraction below 1% and population density below 2 km^{-2} (possibly wetlands or other uninhabited areas), and increased albedo with high canopy fraction (possibly intact forests with low levels of development).

The best fit spatial autoregressive GAM for albedo predicted by LST at 500 m aggregation (31% deviance explained) showed a negative effect on albedo in pixels with LST below 25.6 °C (mean effect -0.004 [-0.027–0.000]), a slight positive relationship in pixels with LST of 25.6–31.3 °C (mean effect 0.001 [0.000–0.002]), and a negative association above 31.3°C (mean -0.004 [-0.015–0.000]) (Figure 2.4). The association of lower-albedo pixels seen at 30 m and 500 m with both unusually high and unusually low LST pixels could be due to several factors. Pixels with low LST and low albedo may include areas with more shadow or partial exposure to open water, or may be due to the presence of low-albedo but high-thermal admittance materials like stone or asphalt building materials that had not warmed at their surfaces significantly by mid-morning. Higher-LST pixels may represent low-albedo/low-admittance materials such as soil that developed higher surface temperature by mid-morning. Some of the extremely high LST values retrieved may also be partly an artifact of the method used in this study, which relies on atmospheric corrections that may result in over-estimation of true LST during summer months when atmospheric water content is high (Windahl and de Beurs, 2016).

Further aggregating the 30 m pixels to town boundaries (water pixels excluded), with a median area of 40 km^2 (8–111 km^2), showed even more distinct relationships between albedo and the other urban biophysical metrics compared to the data aggregated to a 500 m grid (Figure 2.5). Mean albedo at the town scale fell within the range of 0.162 (0.130–0.191) (Berlin, most rural) and 0.125 (0.095–0.175) (Somerville, most urban), with an overall central 95-percentile range of town mean albedo of 0.134–0.160. Orthogonal distance regression showed a positive trend in albedo with canopy cover ($\beta = 0.34 \pm 0.05 \times 10^{-3}$, $R^2 = 0.62$), and negative trends with impervious fraction

(β = -0.37±0.04×10^{-3}, R^2 = 0.70), log-population density (β = -2.84±0.82×10^{-3}, R^2 = 0.41), and surface temperature (β = -1.86±0.26×10^{-3}, R^2 = 0.65). The strength of these correlations is consistent with the trends identified in the 500 m aggregate analysis showing generally lower albedo with increasing metrics of urbanization intensity. The most intensely urbanized core areas (e.g. Somerville, Cambridge, and Chelsea) had the lowest aggregate mean albedo and canopy cover, with the highest mean impervious cover, population density, and surface temperature. In contrast, low-density rural towns (e.g. Berlin, Rockport, and Dover) tended to have higher albedo, lower impervious cover, greater canopy fraction, and lower surface temperature. Landscape position alone (particularly distance from the coast) did not determine these town-scale features, as relatively densely built-up towns at the periphery of the study area (e.g. Lowell and Lawrence) were similar in terms of albedo and other surface characteristics to comparably urbanized towns inside the central urban core. At the town scale within the range of mean measured albedo (0.125–0.162) a 0.01 decrease in mean albedo was associated with an approximately 29 (25–35)% decrease in canopy cover, a 27 (24–30)% increase in impervious cover, and a 5.4 (4.7–6.3)°C increase in average summer mid-morning surface temperature. An increase of population density from approximately 11 km^{-2} to 386 km^{-2} (i.e. from 29–1,000 persons $mile^{-2}$, the U.S. census lower boundary for urban-classified areas) was also associated with an approximate 0.01±0.006 decline in mean albedo. Maximum mean albedo differences of approximately 0.035 (0.030–0.039) between towns in this study were associated with mean surface temperature differences of approximately 12.7 (11.9–13.7) °C, considerably larger than the average 3.4 °C surface temperature decrease measured in one neighborhood in

Chicago following an overall albedo change of +0.07, but also related to much more dramatic differences in land cover character between the constituent towns (Mackey et al., 2012). Some of the differences in albedo previously reported across other large urban basins (e.g. Brest, [1987]; Hafner and Kidder [1999]) may have been similarly due to comparable underlying effects of gradients in land cover character and spatial co-occurrence measured in this study. Other studies have demonstrated a cooling effect with greater tree cover and a warming effect with greater impervious cover in urbanized areas in this bioclimatic region (Rogan et al., 2013) and elsewhere (Estoque et al., 2017; Small, 2006), but the results of this study provide evidence of an embedded albedo component to the surface temperature consequences of these gradients in urbanization intensity.

3.3 Data quality assessment

While it was not possible to judge retrieval accuracy against an independent data source (e.g. tower albedo measurements) in this study, the precision of individual retrievals at each pixel location in the combined multi-year data appeared to be considerably higher than the stated error of the MODIS albedo/BRDF product (Table 2.S2). Data coverage at each pixel location was generally high, with a median of 13 (8–25) good-quality retrievals at each pixel. Overall dispersion at the 30 m pixel level showed a median standard deviation of 0.014 (0.007–0.035), considerably lower than the stated ±0.05 accuracy standard set for the MODIS BRDF/Albedo retrievals but generally in accord with the RMSE of high-quality retrievals over a variety of snow-free landscape types (Shuai et al., 2008). The median standard error of the mean for retrievals was 0.004 (0.002–0.010), indicating that the precision of the estimate of the mean albedo retrieval at most locations would be below

±0.01. Measures of precision were also consistent across LULC category, indicating dispersion of well below ±0.05 in individual categories. The difference between the within-pixel median value for all included data and a single-day relatively cloud-free albedo retrieval (26 July 2006) were also near zero, and did not vary greatly by LULC type. Differences between the multi-year average albedo and single-day clear scenes was minimal, but may have indicated a slightly lower albedo overall in the early part of the season (Table 2.S3). Trends in albedo with other land cover metrics were similar between the multi-year average and the selected single-date data when aggregated to both 500 m and to the town boundaries (see Supplemental).

Results of this error sensitivity analysis show that variability across scenes was generally lower than 0.01 and did not show systematic changes in albedo, or its relationship to other land cover metrics, across the temporal range of observations or among different LULC types. The narrow range of albedo retrieval at each pixel location, the small differences in retrievals between acquisition dates, the large number of available pixels, and the restriction of albedo retrievals to snow-free areas with higher-quality concurrent BRDFs argue that the trends and differences identified in this study, though within the stated global accuracy of 0.05 for the MODIS albedo/BRDF product, are nevertheless likely to be robust.

3.4 Regional effects of albedo on surface energy balance and LST

Differences in albedo between LULC categories at the 30 m pixel scale were relatively weak, but mean albedo at the town scale was associated with broad differences in the distribution of LULC fractions, with higher fraction of "undeveloped" LULC types in rural low-density towns and higher fraction of "developed" LULC types in more intensively urbanized towns (Table 2.S1). In contrast, the water areal fraction (%) at the town scale did not show a clear urban-rural gradient and had differing effects on albedo and surface temperature, where a weak negative trend in mean albedo (including water) with greater fraction of water coverage (β = -1.06±0.52×10^{-3}, R^2 = 0.16) showed no corresponding link between water cover fraction and mean surface temperature (β = -0.03±1.64×10^3, R^2 = 0.00). This lack of trend between water fraction and surface temperature is in contrast to studies identifying both positive and negative UHI temperature relationships to the areal fraction of open water (F. Kong et al., 2014; Steeneveld et al., 2014; Sun and Chen, 2012; Weng et al., 2004). While open water fraction in the metropolitan Boston study area did affect town-scale mean albedo, it did not appear to exert a strong influence on town-scale mean LST.

A spatial autoregressive GAM of the relationship of 30 m LST to albedo, canopy cover, and impervious fraction (excluding water pixels) predicted 75.9% of deviance (27.2% of deviance in spatial autoregression only). The modeled effect on LST was generally negative for canopy cover, positive for impervious fraction, and variable for albedo, with negative effects at the extremely low and moderately high values, and little effect near the overall average albedo, (not shown). The total range of the potential modeled effect was highest for albedo (-6.9–6.1 °C), followed by impervious fraction (-1.0–5.4 °C) and canopy (-2.9–3.1 °C). However, the median effect for albedo was negligible at 0.1 (-0.6–0.3) °C, compared to -1.0 (-1.0–5.1) °C for impervious fraction and 0.3 (-2.6–2.9) °C for canopy fraction. Therefore, though a few exceptional pixels with very high and very low albedo showed a strong influence on the modeled LST, for most pixels at 30 m impervious fraction and canopy showed the strongest influence in the simultaneous model. These results were similar to findings in other remote-sensing based studies showing a positive effect on impervious cover on urban daytime LST with a negative effect of canopy cover and weak effect of albedo (Chen et al., 2006; Haashemi et al., 2016; Jenerette et al., 2016; F. Kong et al., 2014; Zhang et al., 2016). These results further support analysis of the 500 m aggregated data showing that both low and high albedo corresponded with low LST (possibly due to effects of thermal admittance), but also show a limited effect of increasing LST in the <0.01% of pixels with albedo above approximately 0.50. Cluster analysis based on k-means unsupervised classification showed that at both 30- and 500 m coherent areas of higher temperature tended to associate with areas of lower albedo, though coherence in LST was apparently higher than albedo at either scale, probably due to the greater scale length of the LST measurement and the UHI temperature anomaly (see discussion below) (Figure 2.6).

Though the absolute albedo differences at the town scale in this study were small compared to the fine-scale variability in albedo across the study area, these differences have potentially important implications for regional energy balance and climate. Assuming a 24-hour average June–August solar irradiance of 219.4 W m^{-2} for the region (as measured 2002–2008 at Boston Logan Airport), the mean albedo difference between the five most densely populated towns (with a combined 2010 population of approximately 875,000) and that of the 20 least densely populated towns resulted in an average of 4.7 (3.4–5.9) W m^{-2} increase in solar energy input, concentrated in the relatively small area of the most intensively urbanized segments of this study area. The additional shortwave radiative forcing due to albedo change in the most intensively urbanized areas in this study was smaller than values of up to 51 W m^{-2} reported during peak daytime irradiance for Basel, Switzerland (Christen and Vogt, 2004), was comparable to modeled decreases in continent-scale shortwave forcing achievable by urban albedo modification (Menon et al., 2010), and was considerably greater than the current radiative forcing estimated for albedo shifts with historic land use change (-0.367–0.334 W m^{-2}) over broader ecoregions of the U.S. (Barnes and Roy, 2010). Mean LST was also elevated by 10.5 (9.6–11.6) °C in these most urbanized towns compared to the same rural background, though with the caveat that the LST retrievals for the study period may have a positive bias (Windahl and de Beurs, 2016). Near-surface air temperature is of greater importance than LST in terms of human health and comfort, which in the case of Boston have been reported from 0.13 °C (spring daytime) up to 2.9 °C (summer nighttime) higher in urban areas compared to rural (Wang et al., 2017). The relationship between LST and near-surface air temperature in the UHI is complex, and can vary greatly depending on diurnal and seasonal timing and on characteristics of the underlying land surface fabric (Krehbiel and Henebry, 2016; Wang et al., 2017). Given these complexities, the specific contribution of albedo changes to land- or near-surface temperature differences across this region cannot be precisely modeled with the data prepared for this study. However, the spatial coincidence of lower albedo and higher LST imply that an increase in shortwave energy absorption could form a portion of the measured increases in LST due to the small-scale decreases in albedo with increased urbanization intensity, which may further help to drive higher near-surface air temperatures. These results also demonstrate a clear tradeoff between canopy and impervious cover at the town-scale, with albedo as a co-factor in this tradeoff. These correlated trends in land cover properties corresponded to a gradient of potential albedo-related radiative forcing with the potential to affect surface temperature.

3.5 Effect of spatial scale in analysis

Positive spatial autocorrelation as measured by Geary's *c* across the full study area was very high at short spatial lags (30 m) in both the albedo (0.10) and surface temperature data (0.02) (where values closer to 0 indicate increasing correlation), but differed in rate of decrease with increasing lag (Figure 2.S2). At a scale of 480 m (approximately the scale of MODIS pixels) albedo had Geary's *c* of 0.71, increasing to 0.84 at 1200 m lag, while in contrast surface temperature had Geary's *c* of 0.42 at 480 m, increasing to 0.55 at 1200 m. The sharp decline in autocorrelation of the albedo data with increasing spatial lag (scale) partly explains the reduced variability and more discernible land cover and surface temperature trends when the data were aggregated to the coarser 500 m and town-scale units for analysis, with highly similar neighboring pixels aggregated into less variable and less autocorrelated spatial units. The scale of clustering in albedo features was apparently somewhat greater than the 30 m measurement scale, but was in large part smaller than the 500 m and larger aggregations scales. Autocorrelation in LST was higher than albedo, and the slower decline in autocorrelation in LST with increasing spatial lag may reflect both the larger measurement scale of the thermal infrared observations (60- and 120 m), as well as the larger length scale of transitions between temperature features compared to shorter-scale features in albedo. Spatial autocorrelation may also have decayed more quickly with lag in more homogenous rural segments of the study area compared to more intensively developed segments. For instance, in rural Berlin the Geary's *c* metrics had reached a plateau of relatively low autocorrelation by lags of 0.90 and 0.73 at lag of 450 m for albedo and LST, respectively, while at the same positions the respective Geary's *c* values for Boston were 0.72 and 0.38. Other studies of the UHI have noted high spatial autocorrelation in features of urban land cover and surface temperatures in 30 m data, with clearest trends between cover metrics tending to emerge at aggregation scales (200–700 m) that were variable but higher than the native Landsat resolution (Estoque et al., 2017; Song et al., 2014). The aggregation of fine-scale measurements into larger spatial blocks reduced overall variability, helping to highlight trends among the land cover metrics, but also creates the potential for ambiguity in interpretation due to the Modifiable Areal Unit Problem (Jelinski and Wu, 1996) given the arbitrary boundaries of the units of spatial aggregation. Fully addressing this problem is beyond the scope of the current work, but the analysis of trends across multiple aggregation scales and quantification of spatial autocorrelation provide some insight into the potential impact of this problem on the conclusions of this study.

Variability in albedo across all land cover metrics was considerably lower in both the 500 m aggregated Landsat data and the MODIS 500 m data compared to the unaggregated 30 m data, likely due to the averaging of variable but spatially autocorrelated 30 m albedo and other land cover metrics into the larger pixel signal, particularly in the more urbanized regions where autocorrelation was higher. Albedo measured in the 500 m MODIS data showed comparable trends of increasing metrics of urbanization intensity to the 30 m Landsat-derived data aggregated to 500 m, but were displaced in albedo by about -0.017, possibly due to signal contamination with proximity to low-albedo adjacent water or to instrument calibration differences (Figure 2.S3). However, because of the effect of open water on the albedo signature and the scale mismatch between LULC patches and the MODIS 500 m albedo data, it was necessary to first exclude pixels with significant exposure to open water (>10% coverage per pixel) for analysis of the MODIS 500 m data to be comparable to the aggregated Landsat 30 m data. This filtration resulted in the elimination of albedo data over extensive margins of urbanized land along coastal and inland water margins where a significant fraction of the densest urban development was located. Even after exclusion of these potentially affected pixels, 500 m MODIS data aggregated at the town scale showed that small coastal towns and towns near large lakes or rivers displayed unrealistically low albedo signatures given their other metrics of development intensity, compared to the relationships shown based on the 30 m Landsat observations (Figure 2.S4). Given the likely incorporation of adjacent water cover into pixels along water margins due to variability of the effective resolution of the MODIS 500 m BRDF/albedo data (Campagnolo et al., 2016), the unusually low albedo seen in coastal towns in the region shown in the MODIS 500 m albedo data is likely due to this unaccounted-for water signal.

4. Conclusions

This study addresses an empirical gap in knowledge on the variation in surface albedo across heterogeneous urban areas, the relationship of albedo to other urban land cover characteristics, and the potential link between lower albedo and increased temperature across an urbanized landscape. Our results demonstrate that mean albedo was reduced by up to 0.035 (0.030–0.039), to a minimum of 0.125, in more densely developed areas with lower tree canopy cover, higher impervious fraction, and greater population density, with the most distinct albedo effects at the extreme end of the development intensity spectrum. These differences in land cover character and albedo were also associated with a shift towards higher coverage of more intensively constructed urban LULC cover types and reduction in more highly vegetated cover classes. Areas with lower albedo also showed higher mean mid-morning LST (up to 10.5 °C warmer than the rural background). The measured albedo gradient was also associated with gradients in canopy, impervious fraction, and population density, each with possible correlation with or influence over latent cooling, convective heat transfer, and longwave radiation absorption and release processes. Our results provide empirical constraint on albedo as part of the suite of covarying land cover characteristics that together are associated with increased summertime LST and increasing urbanization in our study region.

Results of analysis of the 30 m data aggregated based on town boundaries and 500-m MODIS pixel footprints demonstrate that the scale of spatial patterning in the albedo and land cover metrics used in this study was generally larger than the 30 m Landsat resolution, and clear patterns in albedo and land cover quality did not emerge in direct analysis of the high-resolution data. This scale sensitivity may have been partly due to high variability and spatial autocorrelation in albedo and LST at scales of below roughly 500 m, suggesting that a larger aggregated scale was most appropriate to reveal the linkages between land cover properties, albedo, and land surface temperatures patterns. In contrast, a priori LULC categories and broad-scale statistical indicators of “settled area” like the CDP boundaries explained less variation in albedo, as predefined cover categories captured only some degree of the spatial cohesion of these features and included a wide range of underlying biophysical cover conditions.

A key influence on surface albedo was the presence of open water. Given that urban areas are very often located near surface water features, controlling for the influence of open water will be critical in accurately assessing the albedo of urban land cover. Though a larger spatial lens was needed to detect linkages between the land cover metrics, albedo, and surface temperature, high-resolution data were needed to provide sufficient control over which pixel populations were included (i.e. excluding open water pixels) in the aggregate statistical analysis. Courser data, such as MODIS (500 m), are at risk of confounding the low-albedo features like open water with other lower-albedo urban land cover features.

Urban microclimate models use a variety of approaches to parameterize albedo in order to simulate energy exchange at the land surface. Our results indicate that parameterizing albedo in urban climate modeling using generalized values for different LULC classes can result in considerable error given the wide range of albedo values measured between classes. The net change in albedo in the most intensively urbanized areas may be considerably smaller and more varied over space than has been assumed in some numerical modeling approaches for urban climate (e.g. Falasca et al., 2016). Analysis of trends between albedo and other land cover metrics in the study area show that on a regional basis (several km scale) albedo gradients across an urban-rural gradient may be broadly predicted, opening the potential for further study on the implications for surface energy balance of urban land expansion (Reinmann et al., 2016). Further work will be necessary to investigate the generality of these albedo/land-cover relationships in other urbanized regions with varying development histories, land use patterns, and local ecological and climatic context.

Though urban land cover is concentrated over 1–2% of the earth's land surface, if lower albedo is a feature of urban land more generally, albedo shifts with urbanization may form meaningful a component of both local and global climate forcing (Akbari et al., 2009). The potential exists for local UHI temperature mitigation through albedo manipulation (e.g. "cool roofs", Li et al., 2014), with the prospect for relatively large regional cooling effects, but with potential tradeoffs such as increased wintertime heating demand and reduced precipitation (Georgescu et al., 2014). In the case of the Boston area, the findings of this study provide context for the feasibility, targeting and scaling of albedo manipulation. Urban-rural albedo decline in the study area was of a similar order to albedo increases that have been achieved through use of reflective building materials elsewhere (Mackey et al., 2012) and with surface albedo measurably lower than some of the highly reflecting coatings that might be deployed on exposed surfaces like roofs (Rosenfeld et al., 1995). These findings also suggest that meaningful albedo increases would likely be more easily achieved in the most densely developed urban areas.

This study provides a potential empirical constraint for the radiative description of urban surfaces for numerical studies of surface energy flux or for urban climate models that simulate energy exchange in the complex urban canopy (Frey and Parlow, 2009;

Groleau and Mestayer, 2013; Krayenhoff and Voogt, 2010; Oleson et al., 2008). The interacting effects of climate change and the UHI phenomenon, and the risk posed by rising temperatures in urban environments and altered surface energy balance with urban expansion more broadly, underscores the need for a greater understanding of the albedo drivers behind this land cover change process, and the scope for albedo modification as a future mitigation tool.

Acknowledgments

The authors wish to acknowledge important input from Boston University colleagues Elizabeth Cowdery, Conor Gately, Jackie Getson, Christopher Holden, Keith Ma, Valerie Pasquarella, Andrew Reinmann, and Damien Sulla-Menashe. This research was supported by NASA NNX12AM82G, NSF DEB-1149471, the Pardee Center for the Study of the Longer-Term Future, and seed funds from the Hariri Institute and the Boston Area Research Initiative. The development of the Landsat-scale albedo retrieval was supported by NASA NNX14A173G and USGS G12PC00072. The authors declare no conflicts of interest in conducting this research. The data used are listed in the references and are available in the Boston Area Research Initiative Dataverse repository (DOI: 10.7910/DVN/GLOJVA) at https://dataverse.harvard.edu/dataset.xhtml?persistentId=doi%3A10.7910%2FDVN%2FGLOJVA. The authors also wish to acknowledge the extensive and helpful comments provided by the three anonymous reviewers of this article

Figure 2.1: Data sources used in this study: A) Albedo (showing Massachusetts state outline and Interstate 495 study area boundary); B) Town municipal boundaries; C) Census-designated places (CDP); D) Tree canopy fraction (%); E) Impervious cover fraction (%); F) Population density (km^{-2}); G) Mean summer land surface temperature (°C).

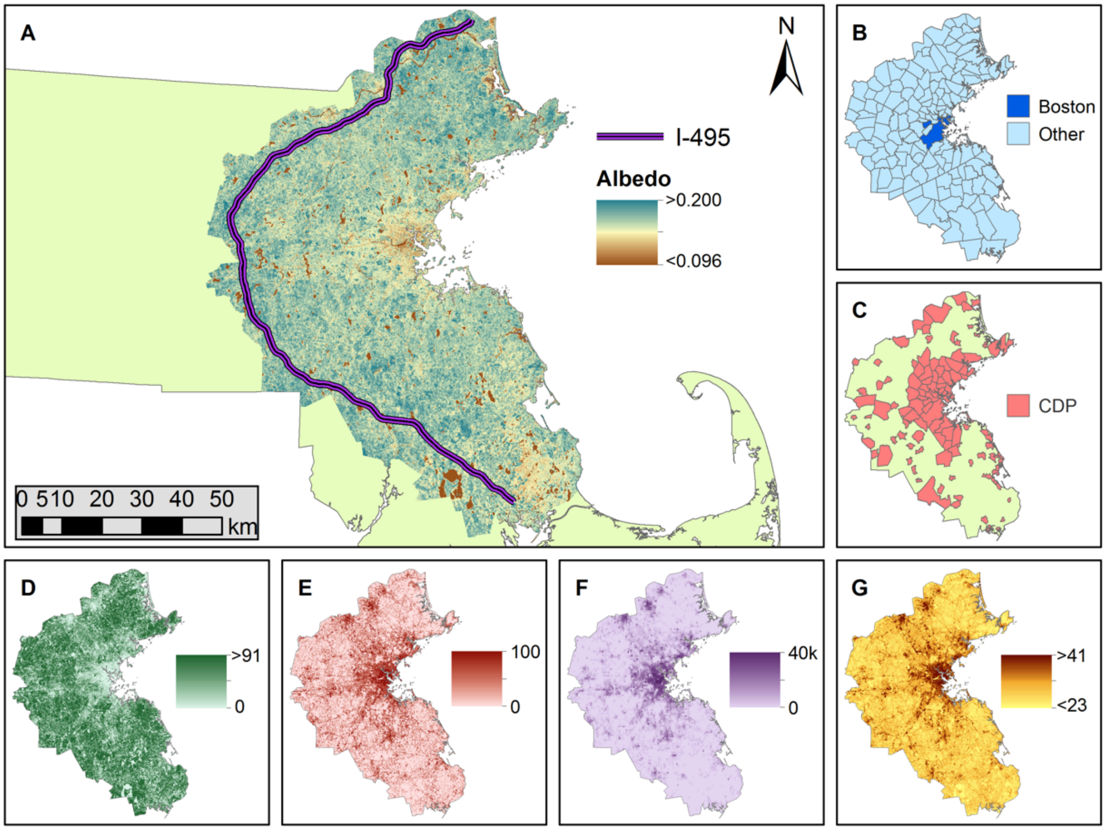

Figure 2.2: Land cover features inside approximate MODIS 500 m pixel boundaries re-projected to UTM 19N (green box) in Watertown-Newton, MA (clockwise from top left): Landsat-derived 30 m albedo (July–August 2003–2008); MODIS 500 m albedo (July–August 2003–2008); land-use/-cover classification map (ca. 2005), and; high-resolution orthophoto (ca. 2005).

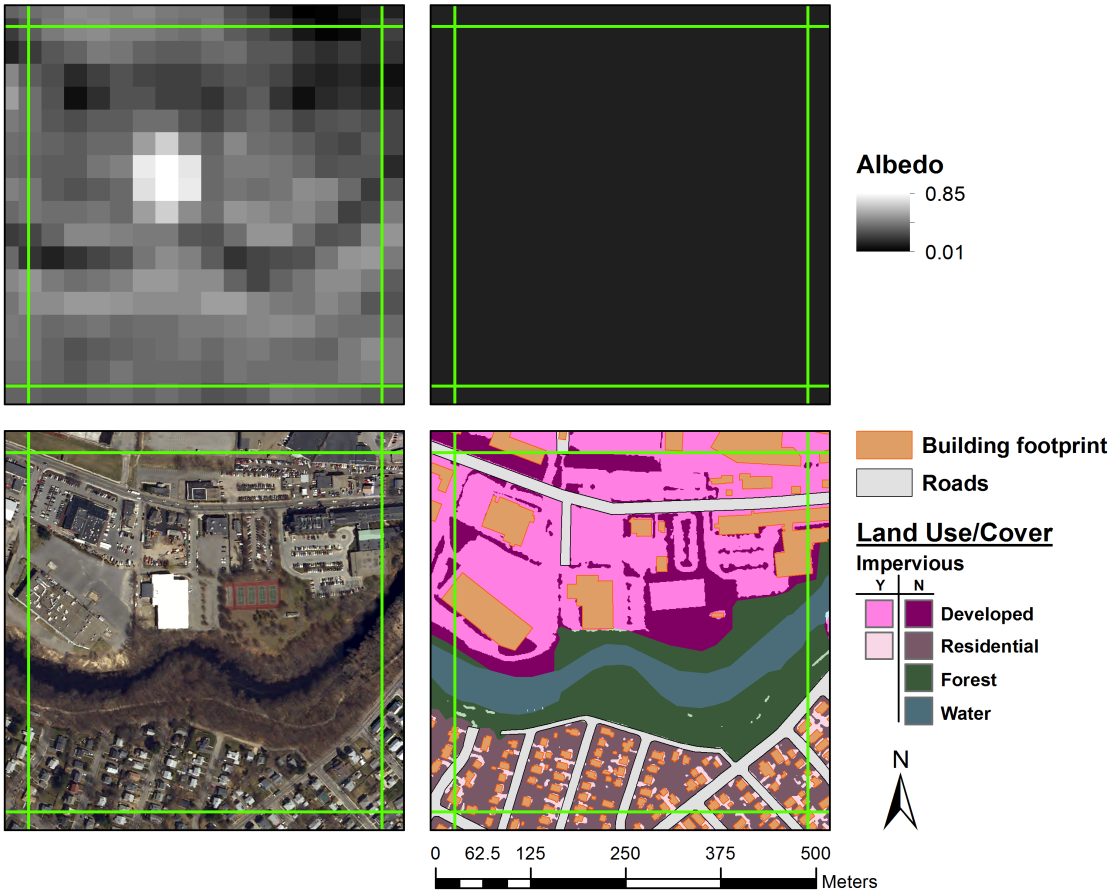

Figure 2.3: Distributions of 30 m pixel values for albedo (top) and canopy fraction (bottom) across the most common land-use/-cover classes in the study area (Cropland, Forest, Forested wetland, Very low density residential, Low density residential, Medium density residential, High density residential, Multi-family residential, Commercial Industrial, Transportation, Water), representing approximately 84% of total area. Bar widths show relative frequency of class, dotted lines show medians for whole study area; pixels more than 1.5 times interquartile range beyond 1st and 3rd quartiles not shown.

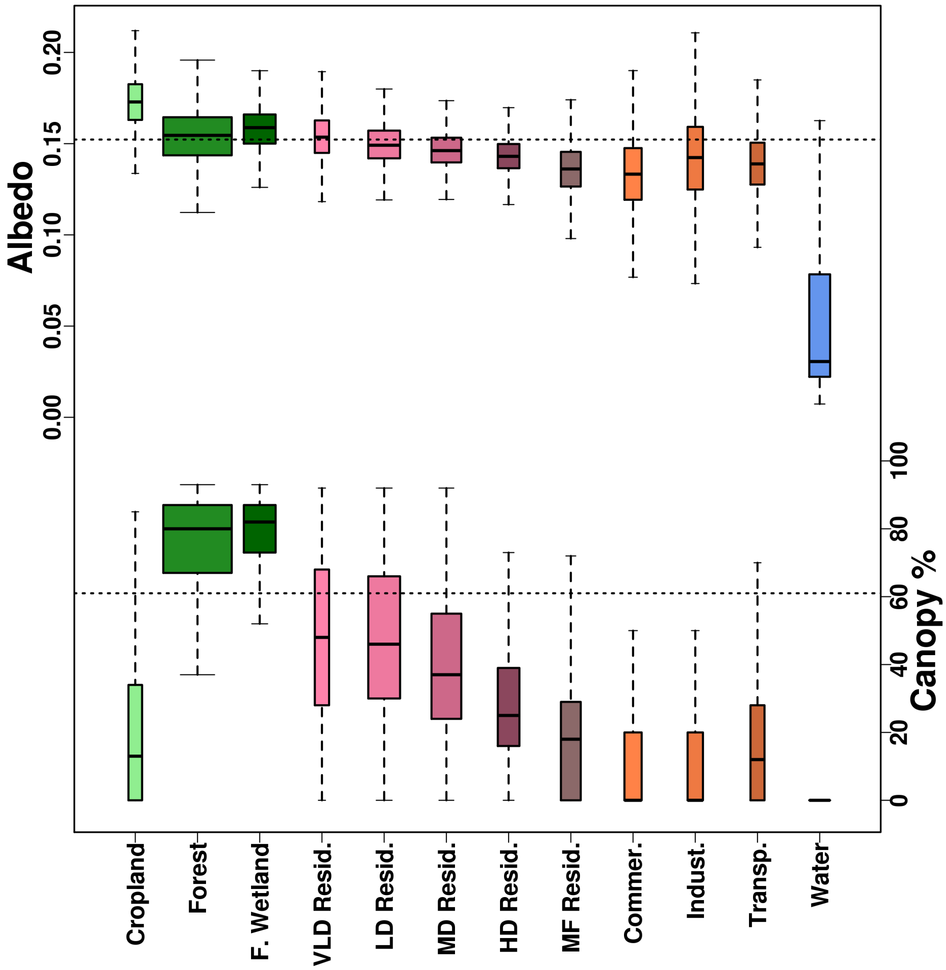

Figure 2.4: Scatterplots of 30 m Landsat albedo values spatially aggregated to an approximate 500 m MODIS grid (excluding pixels classed as water), versus (clockwise from top left) canopy fraction, impervious fraction, land surface temperature (°C), and population density (km^{-2}, log scale). Shading shows pixel density; solid lines show cubic regression splines without spatial autoregressive term; dotted lines show 95% confidence interval along a moving window; blue lines indicate pivot points along land cover metric according to GAM analysis accounting for spatial autocorrelation. Blue background dots show comparable 30 m pixel scatters with scales clipped to include central 99% of values.

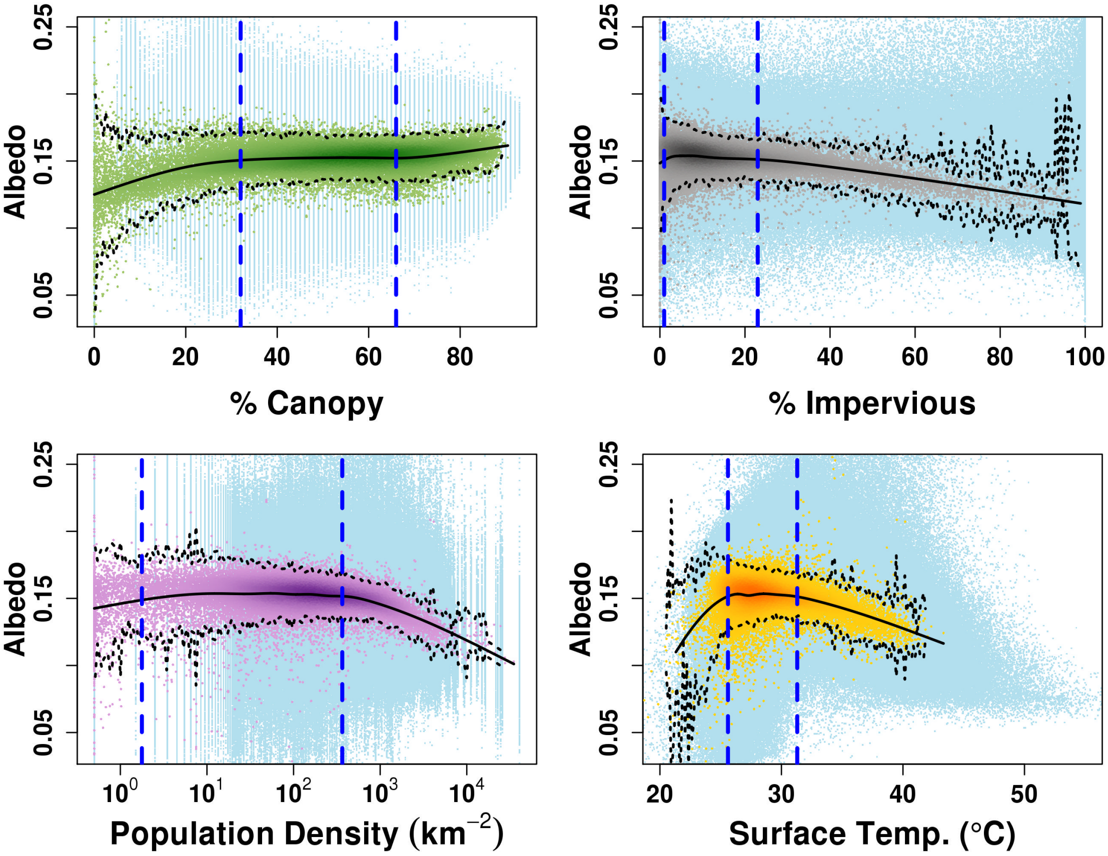

Figure 2.5: Mean albedo versus (left) impervious fraction and (right) tree canopy fraction, Landsat 30 m data aggregated by town (selected towns labeled, open water pixels excluded). Color ramp corresponds to mean mid-morning land surface temperature, dot size corresponds to mean population density.

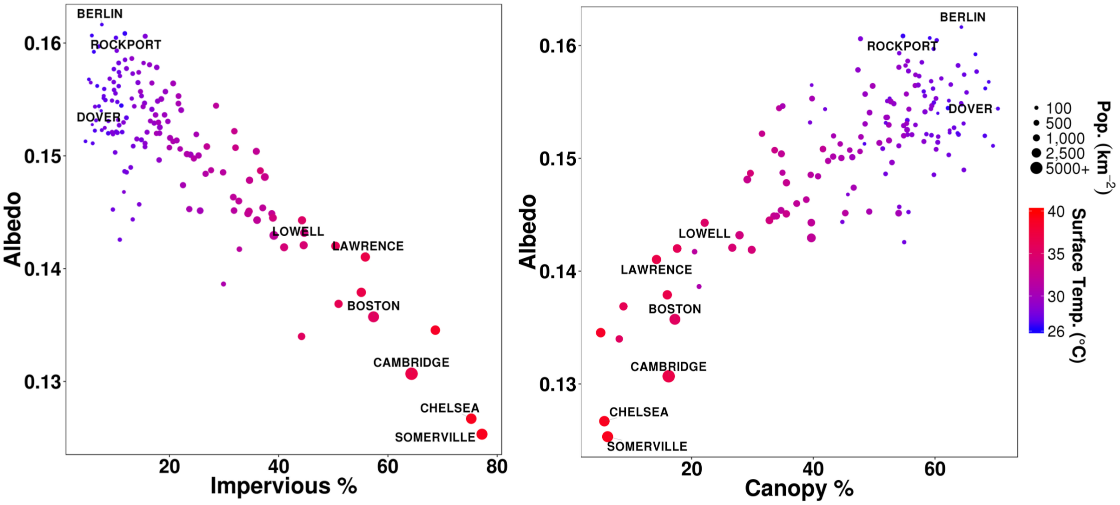

Figure 2.6: (L) Orthophoto Waltham (R) and Weston (L) Massachusetts approximately 64 km^2 (photo courtesy of Google Earth); (R) Unsupervised classification results for (a) 30 m albedo; (b) 500 m albedo; (c) 30 m LST; and (d) 500 m LST for the same region (excluding water). Scale bars show mean values for each cluster class (LST in °C).

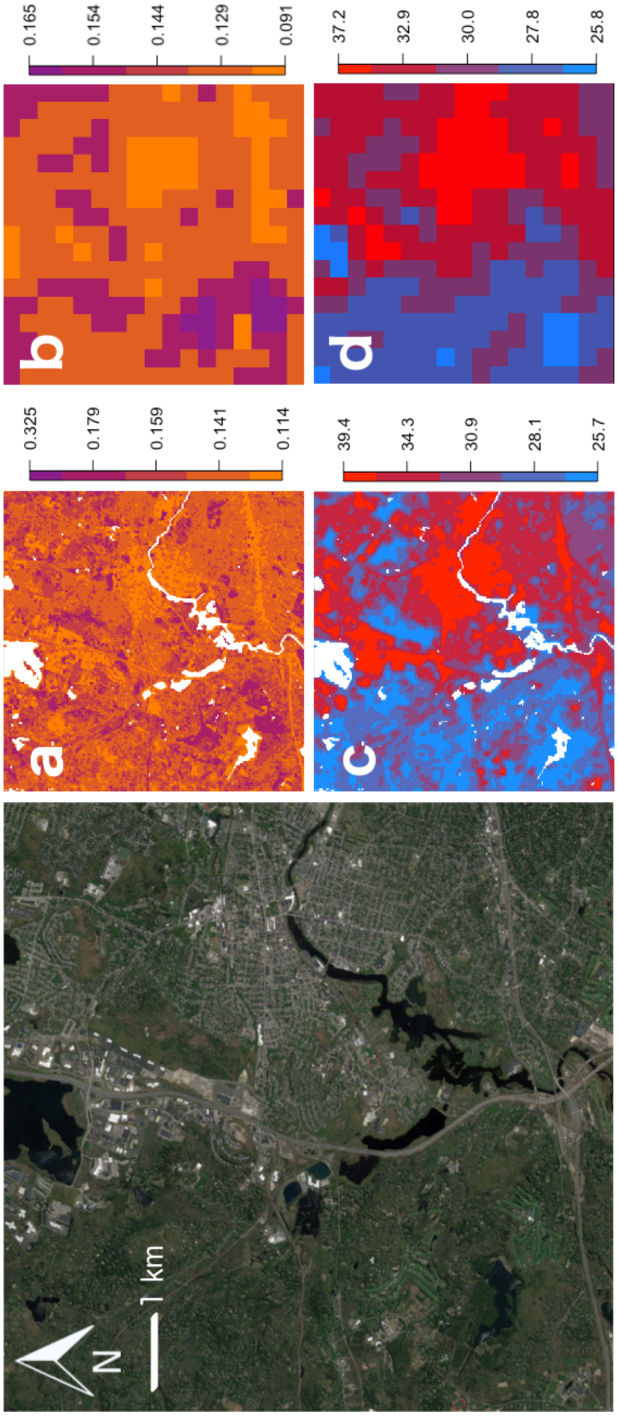

Table 2.1: Day-of-year for scenes used in 30 m summer albedo.

Year	Landsat 7 ETM+
Path 12, Row 30	
2003	231
2004	170, 186, 202, 218
2005	156, 204
2006	191, 207, 223
2007	162, 178, 194, 210, 226, 242
2008	165, 197, 213, 229
Path 12, Row 31	
2003	199, 215, 231
2004	154, 186, 202
2005	156, 204
2006	191, 207, 223
2007	162, 178, 194, 210, 226, 242
2008	165, 181, 197, 213, 229

Table 2.2: Results of spatial autoregressive GAM analysis of albedo versus land cover metrics (aggregated to 500 m). Mean modeled effect for each development intensity interval shown with central 95th percentile spread.

Land cover metric		**Development Intensity**			**Deviance explained**
		Low	**Medium**	**High**	
Canopy %	Threshold	*0–32%*	*32–66%*	*66–100%*	33.1%
	Effect	-0.007 (-0.023–0.000)	0.001 (0.001–0.001)	0.003 (0.001–0.008)	
Impervious %	Threshold	*0–1%*	*1–23%*	*23–100%*	27.4%
	Effect	-0.001 (-0.002–0.000)	0.002 (0.000–0.003)	-0.005 (-0.017–0.000)	
Population density	Threshold	*0–2 km*$^{-2}$	*2–365 km*$^{-2}$	*>365 km*$^{-2}$	26.9%
	Effect	-0.003 (-0.004–0.000)	0.002 (0.000–0.003)	-0.004 (-0.015–0.000)	

Supplemental Information for *Albedo, land cover, and daytime surface temperature variation across and urbanized landscape*

This Supplemental Information contains tables and figures referred to but not presented in the article text, as well as the methodology and results of the Albedo Data Quality Assessment

2.S1. Albedo Data Quality Assessment

Albedo in this study was analyzed as the median value of several year's worth of summertime albedo retrievals at each pixel location, such that multiple retrievals per pixel are available to measure the dispersion of albedo estimates at each location. Though these retrievals incorporated interannual land cover changes, transient atmospheric effects, and random or systematic instrument error, their dispersion can be used to indicate the precision of the albedo retrievals and the effect of LULC type on retrieval. Within-pixel dispersion, while not a direct measure of accuracy in retrievals against another measurement source, can provide a sense of the reliability and internal consistency of these retrievals and indicate potential for systematic uncertainties. To assess within-pixel dispersion, we evaluated several metrics of dispersion within the population of all available high-quality albedo retrievals (standard deviation, standard error of mean, and width of the central 95% of data) for the most prominent LULC types at every pixel location for the range of June–August, 2003–2008. The median within-pixel value was also compared to the value retrieved in a single mid-range scene (26 July 2006) to gauge the bulk deviation of the mulit-year average from a particular one-time retrieval.

In constructing an average albedo dataset, there was also the potential for error to be introduced in combining retrievals that differed between scenes (e.g. land cover change) or took place at differing phenological stages (though all data was restricted to retrievals based on high-quality summertime observations). To examine these inter-temporal effects, three single-day scenes with high retrieval quality and low cloud contamination from across the annual and seasonal window were analyzed for comparison to the multi-year combined albedo. Selected scenes were 5 June 2005 (DOY 156), 26 July 2006 (DOY 207), and 30 August 2007 (DOY 242).

Table 2.S1 shows the bootstrap median estimate 95% confidence intervals for several metrics of within-pixel variance for all white-sky retrievals based on MODIS and Landsat ETM+ observations from 2003–2008 (July 1–August 31), as well as the median within-pixel difference between the multi-year composite average and a relatively cloud-free single-day retrieval from near the middle of seasonal observation range (July 26, 2006). Land-use specific figures were determined from a random sample of 1,000 pixels within each category, while whole-area metrics were determined from all available pixels.

Albedo in the single-date scenes was somewhat lower for 5 June (median 0.141 [0.038–0.177]) and 30 August (median 0.147 (0.058–0.187)), but nearly identical to mid-summer observations from 26 July (median 0.151 (0.067–0.184)). All scenes showed albedo distributions with a similar negative skew to the multi-year composite. Albedo by LULC type at both dates was comparable to results for the multi-year composite, with extremely low values for open water but generally overlapping ranges for other cover types. Temporal differences between albedo retrievals were of a similar range across LULC types, and were with a few exceptions well below 0.01. Aggregating single-day retrievals to the MODIS 500 m scale yielded similar shapes for the generalized additive models for both dates and the multi-year combined data (not shown). Orthogonal distance regression of town-scale data derived from the June 5, 2005, observations showed somewhat lower coefficients, but results were comparable to those shown in analysis of the multi-year composite for canopy ($\beta = 0.26 \pm 0.05 \times 10^{-3}$, $R^2 = 0.35$), impervious fraction ($\beta = -0.21 \pm 0.06 \times 10^{-3}$, $R^2 = 0.24$), log-population density ($\beta = -1.48 \pm 0.95 \times 10^{-3}$, $R^2 = 0.09$) and surface temperature ($\beta = -1.04 \pm 0.32 \times 10^{-3}$, $R^2 = 0.21$), but with lower R^2 values overall. Coefficient values were also comparable in the August 30 albedo retrievals but somewhat closer to the multi-year average figures ($0.31 \pm 0.07 \times 10^{-3}$, $-0.38 \pm 0.04 \times 10^{-3}$, $-3.81 \pm 0.76 \times 10^{-3}$ and $-1.88 \pm 0.29 \times 10^{-3}$), and with generally higher R^2 values (0.47, 0.67, 0.52, and 0.61) for canopy, impervious fraction, log-population density, and surface temperature, respectively.

Table 2.S1: Within-pixel measures of variability (median ± 95% confidence interval) in white-sky albedo based on bootstrap resampling of 1,000 randomly selected pixels per LULC category. Column headings refer to the median number of separate observations represented, standard deviation, standard error of mean, median value, spread of central 95% of sample, and difference from the single-scene July 26, 2006 observation benchmark.

Land Use/Cover	# Obs.	SD	St. Err. Mean	Median	Spread of central 95%	Difference from 26 July
Cropland	12	0.018 (±0.001)	0.005 (±0.000)	0.178 (±0.002)	0.055 (±0.004)	0.001 (±0.002)
Forest	13	0.013 (±0.001)	0.004 (±0.000)	0.162 (±0.003)	0.041 (±0.002)	0.002 (±0.001)
F. Wetland	13	0.014 (±0.001)	0.004 (±0.000)	0.165 (±0.002)	0.045 (±0.002)	0.002 (±0.001)
VLD Resid.	12.4	0.013 (±0.001)	0.004 (±0.000)	0.159 (±0.002)	0.040 (±0.002)	0.000 (±0.001)
LD Resid.	12.6	0.012 (±0.001)	0.003 (±0.000)	0.155 (±0.001)	0.038 (±0.003)	0.000 (±0.000)
MD Resid.	13	0.012 (±0.001)	0.003 (±0.000)	0.152 (±0.001)	0.038 (±0.002)	0.000 (±0.001)
HD Resid.	13	0.012 (±0.001)	0.003 (±0.000)	0.150 (±0.001)	0.038 (±0.002)	0.002 (±0.001)
MF Resid.	13	0.012 (±0.001)	0.003 (±0.000)	0.143 (±0.002)	0.038 (±0.003)	-0.002 (±0.001)
Commercial	12	0.013 (±0.001)	0.004 (±0.000)	0.139 (±0.004)	0.042 (±0.003)	-0.003 (±0.001)
Industrial	12	0.015 (±0.001)	0.004 (±0.000)	0.150 (±0.004)	0.045 (±0.003)	-0.003 (±0.002)
Transport.	12.3	0.013 (±0.001)	0.004 (±0.000)	0.147 (±0.002)	0.042 (±0.003)	-0.005 (±0.001)
Water	13	0.016 (±0.001)	0.004 (±0.000)	0.033 (±0.004)	0.048 (±0.002)	-0.011 (±0.001)
Whole area*	13 (8–25)	0.014 (0.007–0.035)	0.004 (0.002–0.010)	0.158 (0.057–0.194)	0.042 (0.019–0.113)	-0.000 (-0.023–0.015)

* Whole area statistics based on all available pixels

Table 2.S2: Median albedo (central 95-percentile) in single-day albedo data for bootstrap resampling of 1,000 randomly selected pixels per LULC category.

Land Use/Cover	2003–2008 average	5 June 2005	26 July 2006	30 Aug. 2007
Cropland	0.173 (0.141–0.202)	0.161 (0.116–0.200)	0.171 (0.137–0.204)	0.172 (0.139–0.218)
Forest	0.156 (0.122–0.18)	0.144 (0.113–0.171)	0.154 (0.122–0.175)	0.149 (0.116–0.173)
F. Wetland	0.159 (0.120–0.178)	0.143 (0.106–0.164)	0.156 (0.117–0.177)	0.154 (0.116–0.173)
VLD Resid.	0.155 (0.129–0.182)	0.147 (0.123–0.176)	0.156 (0.128–0.184)	0.151 (0.12–0.182)
LD Resid.	0.149 (0.128–0.173)	0.144 (0.122–0.169)	0.150 (0.127–0.177)	0.146 (0.121–0.173)
MD Resid.	0.145 (0.127–0.168)	0.141 (0.121–0.163)	0.145 (0.125–0.17)	0.142 (0.117–0.167)
HD Resid.	0.143 (0.125–0.165)	0.138 (0.119–0.157)	0.142 (0.121–0.166)	0.138 (0.118–0.165)
MF Resid.	0.133 (0.102–0.164)	0.129 (0.103–0.161)	0.135 (0.099–0.166)	0.128 (0.094–0.164)
Commercial	0.132 (0.09–0.214)	0.129 (0.091–0.204)	0.135 (0.087–0.171)	0.129 (0.077–0.218)
Industrial	0.139 (0.083–0.259)	0.137 (0.089–0.249)	0.140 (0.085–0.182)	0.139 (0.077–0.269)
Transportation	0.139 (0.091–0.194)	0.131 (0.093–0.183)	0.143 (0.092–0.183)	0.140 (0.083–0.188)
Water	0.024 (0.015–0.121)	0.019 (0.011–0.109)	0.040 (0.022–0.15)	0.025 (0.008–0.139)
Whole area*	0.151 (0.049–0.187)	0.141 (0.038–0.177)	0.151 (0.067–0.184)	0.147 (0.058–0.187)

* Whole area statistics based on all available pixels

Table 2.S3: Fractional area of selected land-use/cover classes, presented with mean values for other land surface parameters at town scale for selected towns in the Boston study area (land cover metrics filtered for open water pixels prior to calculation of town-scale means). Abbreviations: IS, Impervious Surface %; LST, Land Surface Temperature; VL- L- M- H-DR, Very Low- Low- Medium- High- Density Residential; Ind., Industrial; Comm., Commercial; Trans., Transportation.

Town	Albedo	Canopy	IS	Pop.	LST	Forest	Water	VLDR	LDR	MDR	HDR	MFR	Ind.	Comm.	Trans.
		%		km^{-2}	°C	%									
SOMERVILLE	0.125	6.2	77	3883	39	0	0	0	0	0	0	54	12	12	8
CHELSEA	0.127	5.7	75	3350	39	1	0	0	0	0	5	35	16	16	12
CAMBRIDGE	0.131	16.2	64	5300	37	2	11	0	0	1	10	25	7	13	2
WINTHROP	0.134	8.1	44	1199	36	0	1	0	0	0	26	28	0	5	15
EVERETT	0.134	5.1	69	2547	39	0	0	0	0	0	4	41	20	9	10
BOSTON	0.136	17.3	57	3784	36	8	2	0	0	2	14	24	4	10	11
LAWRENCE	0.141	14.2	56	2378	37	9	6	0	0	1	21	24	12	9	3
LOWELL	0.144	22.2	44	1613	35	12	6	0	1	2	27	17	7	6	3
ARLINGTON	0.142	26.7	45	1606	34	3	7	0	0	1	48	21	0	7	2
BROOKLINE	0.143	39.7	39	2028	32	14	1	5	8	11	16	18	0	5	1
LYNN	0.143	27.9	45	1744	34	22	6	0	0	5	17	20	7	6	1
NEWTON	0.144	39.7	36	1318	32	12	2	0	2	21	25	12	1	5	2
WALTHAM	0.145	32.8	39	1367	34	22	8	0	0	6	19	11	6	9	2
BRAINTREE	0.149	39.6	30	719	32	25	5	0	3	20	9	4	5	7	3
W. BRIDGEWATER	0.159	54.1	10	154	28	29	1	0	12	3	1	0	2	2	2
HAMILTON	0.16	59.8	7.1	120	27	42	3	3	5	6	1	0	0	0	0
MERRIMAC	0.161	60.3	10	139	27	54	4	2	9	5	1	1	0	1	2
AMESBURY	0.161	47.8	16	271	28	33	10	2	6	8	4	3	2	2	2
W. NEWBURY	0.161	59.1	5.8	67	26	45	8	6	9	0	0	0	0	0	0
ROCKPORT	0.161	54.7	12	198	26	45	2	1	6	11	7	2	0	2	0
BERLIN	0.162	64.3	7.6	52	27	60	2	4	6	0	0	0	0	1	1

Figure 2.S1: Scatterplots of 30 m values of albedo vs. (clockwise from top left) canopy fraction, impervious fraction, surface temperature (°C) and population density (km^{-2}, log scale). Shading indicates pixel density; solid lines indicate fitted cubic regression spline; dotted lines show 95% confidence interval of the albedo mean along a moving window. Scales are clipped to include central 99% of albedo values.

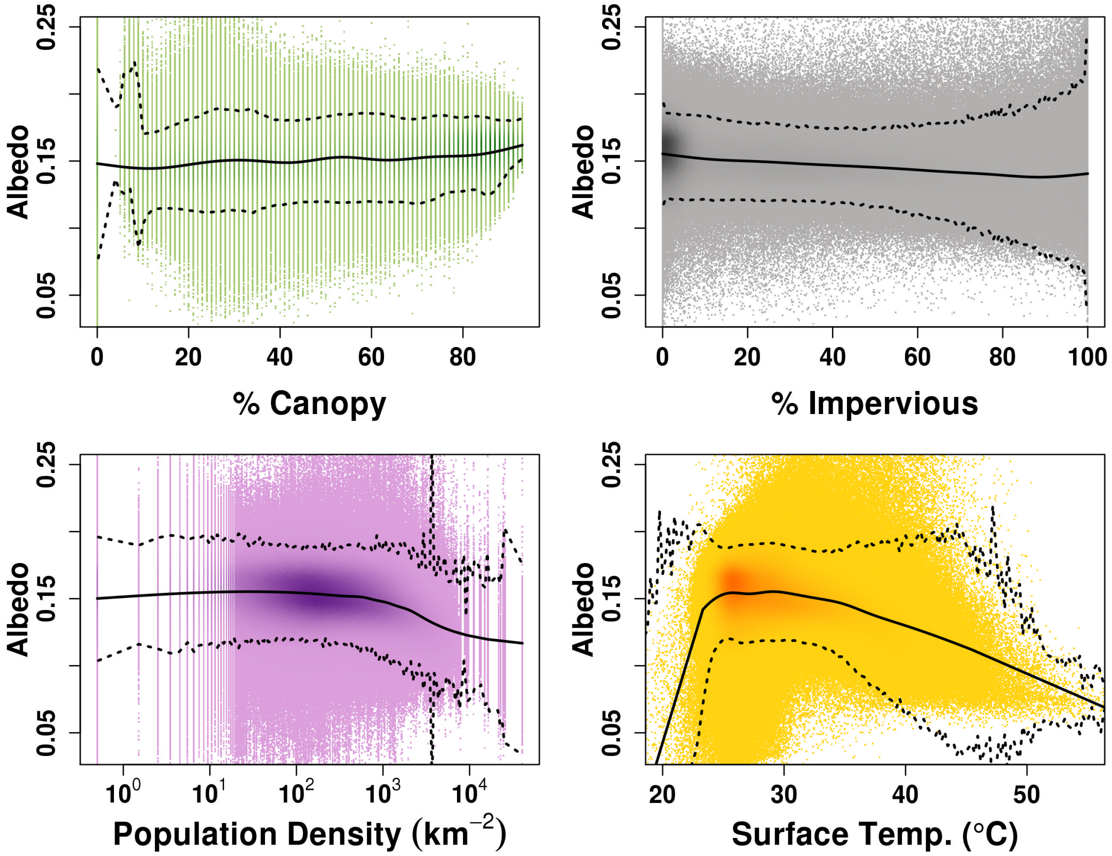

Figure 2.S2: Geary's *c* autocorrelation indices for albedo (left) and LST (right) for the full study area and scenes limited to the municipal boundaries of urban Boston and rural Berlin.

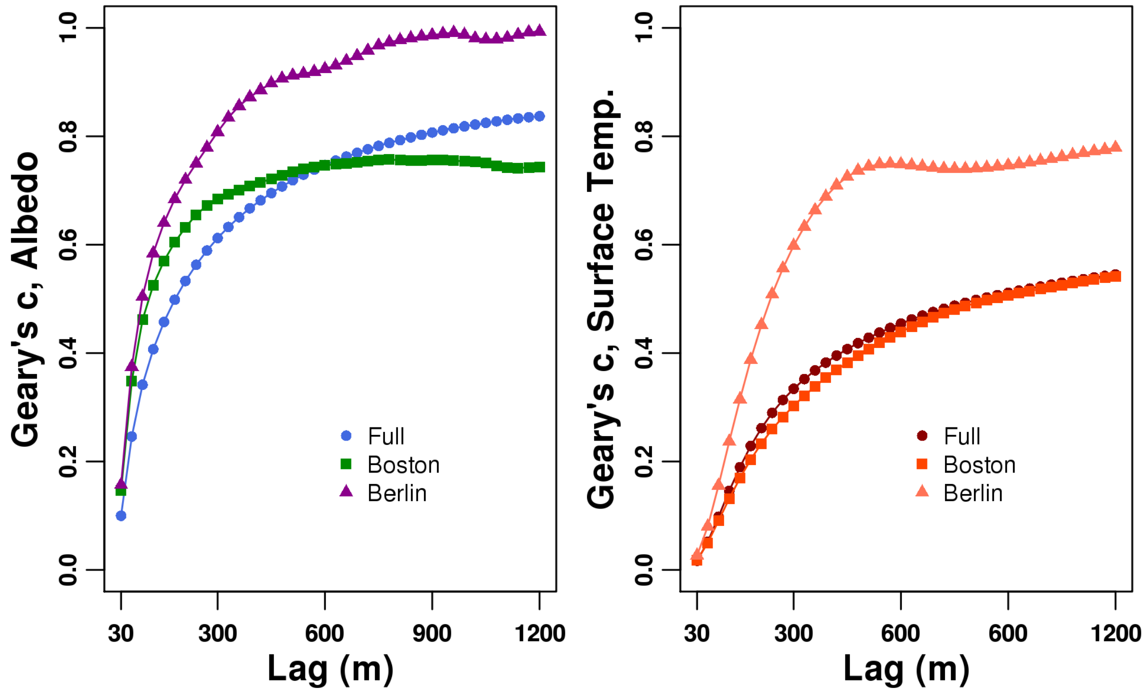

Figure 2.S3: Scatterplots of 500 m MODIS composite summertime albedo (excluding pixels with >10% area water), versus (clockwise from top left) canopy fraction, impervious fraction, land surface temperature (°C), and population density (km^{-2}, log scale), aggregated to the 500 m grid. Shading indicates pixel density; solid lines indicates fitted cubic regression spline prediction; dotted lines show 95% confidence interval of the albedo mean along a moving window. Blue background dots show comparable 30 m pixel scatters with scales clipped to include central 99% of values.

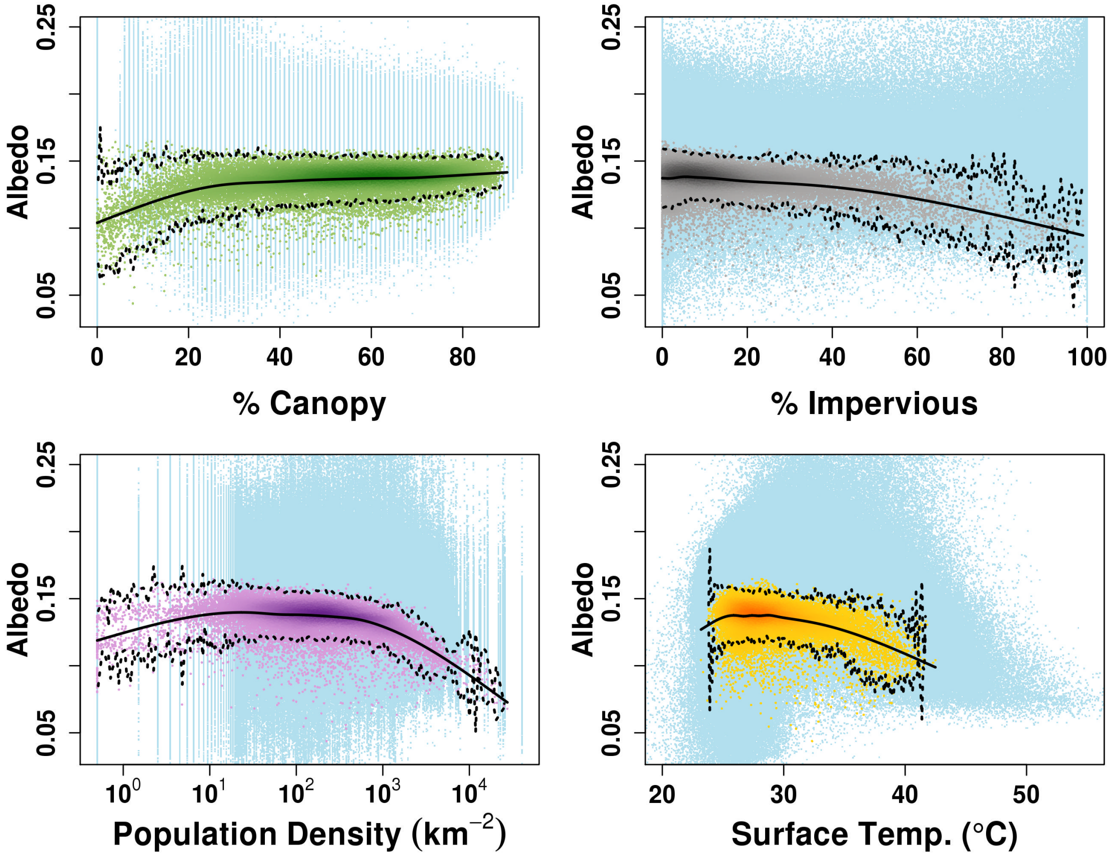

Figure 2.S4: Mean albedo versus (left) impervious fraction and (right) tree canopy fraction, MODIS 500 m data aggregated by town (selected towns labeled, pixels >10% water area excluded). Color ramp corresponds to mean surface temperature, dot size corresponds to mean population density.

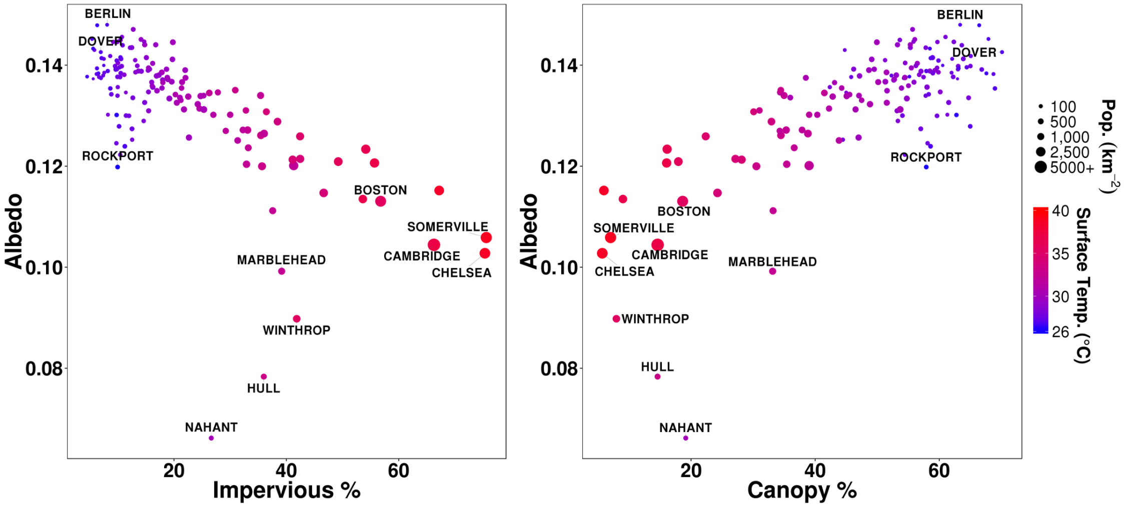

CHAPTER THREE: Current and future biomass carbon uptake in Boston's urban forest

Abstract

Ecosystem services provided by urban forests are increasingly included in municipal-level responses to climate change. However, the ecosystem functions that generate these services, such as biomass carbon (C) uptake, can differ substantially from nearby rural forest. In particular, the scaled effect of canopy spatial configuration on tree growth in cities is uncertain, as is the scope for medium-term policy intervention. This study integrates high spatial resolution data on tree canopy and biomass in the city of Boston, Massachusetts, with local measurements of tree growth rates to estimate the magnitude and distribution of annual biomass C uptake. We further project C uptake, biomass, and canopy cover change to 2040 under alternative policy scenarios affecting the planting and preservation of urban trees. Our analysis shows that 85% of tree canopy area was within 10 m of an edge, indicating essentially open growing conditions. Using growth models accounting for canopy edge effects and growth context, Boston's current biomass C uptake may be approximately double (median 10.9 GgC yr^{-1}, 0.5 MgC ha^{-1} yr^{-1}) the estimates based on rural forest growth, much of it occurring in high-density residential areas. Total annual C uptake to long-term biomass storage was equivalent to <1% of estimated annual fossil CO_2 emissions for the city. In built-up areas, reducing mortality in larger trees resulted in the highest predicted increase in canopy cover (+25%) and biomass C stocks (236 GgC) by 2040, while planting trees in available road margins resulted in the greatest predicted annual C uptake (7.1 GgC yr^{-1}). This study highlights the importance of

accounting for the altered ecosystem structure and function in urban areas in evaluating ecosystem services. Effective municipal climate responses should consider the substantial fraction of total services performed by trees in developed areas, which may produce strong but localized atmospheric C sinks.

1. Introduction

As urban populations expand worldwide, pressure is rising on local ecosystem services to both provide a livable environment in cities and to address the drivers and effects of global climate change (Seto et al., 2012). Urban vegetation performs a suite of these ecosystem services, including key regulatory functions like carbon (C) uptake and storage, moderation of temperature extremes (McDonald et al., 2019), and potentially air pollution mitigation through ozone and particulate matter capture (Roy et al., 2012). Municipal authorities are increasingly assuming a role in mounting a social response to climate change (Castán Broto, 2017), and policy-makers and researchers show growing interest in better quantifying and managing the multiple ecosystem services provided by green spaces and urban vegetation (Kremer et al., 2016; Lovell and Taylor, 2013; Niemelä, 2014). Toward this end, researchers have recently called for more intensive study of these novel and heterogeneous socio-ecological systems and their spatiotemporal organization, both in their own right and in the interest of maintaining the well-being of growing and at-risk urban populations (Alberti, 2015; Groffman et al., 2017; Hutyra et al., 2014; Zhou et al., 2019).

Services related to urban vegetation and their role in climate change adaptation and emissions mitigation have attracted particular policy interest (Gómez-Baggethun and Barton, 2013; Larondelle and Haase, 2013; Lovell and Taylor, 2013). In line with several other cities and municipal alliances like the C40 coalition developing climate responses (Broto and Bulkeley, 2013), Boston, for example, has included the expansion of green spaces and tree canopy cover as strategies in its climate adaptation and emissions reductions plans (Walsh, 2014). However, despite prominent campaigns in several US cities to plant additional urban trees, canopy cover has declined in many urban areas (Nowak and Greenfield, 2012). And in the wake of broad-scale tree planting and other "urban greening" proposals, researchers have highlighted persistent uncertainties in estimating the amount and value of services, the quality and specificity of data and modeling used to estimate services, potential tradeoffs with other disservices such as increased water consumption and allergen production, and the capacity of vegetation C uptake to meaningfully offset comparatively large local fossil C emissions (Pataki, 2013; Pataki et al., 2011; Pincetl et al., 2013). There is moreover little support, beyond fairly generalized models such as UFORE/i-Tree Eco (Nowak et al., 2008), to help urban decision makers assess current forest services, predict the impacts of urban greening policies on net greenhouse gas emissions, or optimize the production of multiple services against their tradeoffs and costs (Escobedo et al., 2011).

Ecosystem services are a product of ecosystem functions, like evapotranspiration or C uptake, that serve human wellbeing, and as such take place in a specific spatiotemporal setting (Escobedo et al., 2011). Many of the services performed by urban ecosystems relevant in climate change mitigation and resiliency planning are related to the amount of live tree biomass present, its rate of growth, and canopy cover and volume (Nowak et al., 2008; Ziter et al., 2019). These services are generated within heterogeneous forest or "savannah-like" ecosystems, the structure and function of which are determined by biophysical setting, human socioeconomic spatial patterns, and inherited legacies of historic and ongoing human activity (Dobbs et al., 2017; Ossola and Hopton, 2018b; Roman et al., 2018). Given its complexity and recency as a study domain, our understanding of urban forest function and its spatial distribution contains considerable uncertainty, reflected in results from urban studies that contradict expectations derived from rural analogues. Despite some ambiguity in definition, "urban" ecosystems can contain substantial biomass concentrations, varying widely with land cover and use (Davies et al., 2011; Raciti et al., 2012c; Rao et al., 2013a). Tree canopy morphology may differ notably in the same species grown in different cities and between urban- and rural-grown individuals (McPherson and Peper, 2012). Growth rates in street- and park trees can exceed or fall short of comparable trees in nearby rural settings (Briber et al., 2015; Gregg et al., 2003; Pretzsch et al., 2017; Searle et al., 2012), while mortality rates tend to be higher in smaller diameter- and street trees (Roman et al., 2014; Smith et al., 2019). Tree growth in remnant urban forest fragments can be significantly enhanced near canopy edges (Reinmann and Hutyra, 2017). Growing seasons under the influence of the urban heat island effect may be longer than nearby rural areas (Melaas et al., 2016).

Existing studies of urban forest growth and C uptake contain uncertainties in accounting for local urban-specific growth rates and the spatial arrangement or extent of tree cover. Several studies estimating services from urban trees have used the Urban Forest Effects (UFORE) model (Nowak et al., 2008), scaling plot-level tree measurements to the broader urban landscape using spatial proxies like mapped land use/cover classes and applying generic corrections for urban-related growth effects (Escobedo and Nowak, 2009; Nowak et al., 2013; Strohbach et al., 2012). A study of tree C storage and sequestration in Los Angeles and Sacramento scaled plot-level biomass inventories to canopy coverage as determined from 2.4 m resolution satellite observations, but lacked error estimation and relied upon generalized growth projections to determine annual C uptake (McPherson et al., 2013). Other studies have only partially estimated C storage and uptake via inventory of sub-populations of urban trees such as street trees or greenspaces (Brack, 2002; Russo et al., 2014; van Doorn and McPherson, 2018). As part of their CO_2 emissions inventory for Salt Lake City Pataki et al. (2009) used a simple age cohort-based growth model for tree biomass C uptake derived from local tree inventory data, with forest extent determined from 30 m spatial resolution Landsat imagery. Other research has estimated temporal change in urban C storage with historical land conversion (Hutyra et al., 2011), and projected future functional shifts under varying mortality and recruitment scenarios for specific tree sub-populations (Smith et al., 2019).

Working from a photosynthetic light-use efficiency framework, several other studies have attempted to model urban vegetation C uptake based in part on light absorption: Miller et al. (2018) estimated gross primary productivity (a C flux not accounting for plant respiration losses) across the city of Minneapolis, Minnesota, based on limited sapflow and eddy covariance measurements corresponding to broad vegetation functional groups (e.g. deciduous trees, turfgrass). They then scaled results spatially based on high-resolution classification maps of vegetation and land cover. Urban micrometeorological studies have partitioned C fluxes limited to the vicinity of measurement towers into vegetation components by adjusting for photosynthetic light absorption (Bellucco et al., 2017; Crawford et al., 2011). Urban vegetation C uptake has been estimated across urbanized areas via light-use models driven by coarse-scale remote-sensing data, but without reference to local observations of vegetation C uptake (Hardiman et al., 2017; Imhoff et al., 2004). However, a complete and adequately spatially resolved understanding of urban ecosystem function, incorporating empirical measures of urban forest extent, productivity, and structure, remains elusive. In addition, this knowledge gap impedes a clear understanding of the potential to optimize urban ecosystem functions via policy.

Effective municipal climate preparedness and protection of urban environmental quality requires a more precise understanding of the local ecosystem functions like C storage and canopy coverage that drive critical services provision. Improved estimates of urban ecosystem function require knowledge of the spatial distribution and growth dynamics of the urban forest. This study combines local observations of tree growth and its relationship to canopy fragmentation with high-resolution maps of biomass and canopy distribution to estimate annual long-lived biomass C uptake in the urban landscape of Boston, Massachusetts. For contrast to estimates grounded in rural forest ecosystem function, we compare our urban-specific results to estimates based on tree growth measured in nearby rural forests. We finally simulate three policies differentially affecting the recruitment and mortality of urban trees to predict future potential trajectories of C uptake, biomass, and canopy cover change through 2040. Improving estimates of these indicators will deepen our understanding urban ecosystem functioning, and highlight the potential effects of green infrastructure policies on climate mitigation and preparedness, with the city of Boston as a specific test case.

2. Methods

2.1 Study area geodata

To develop our estimate of biomass C storage in Boston's urban trees, we employed a 1 m resolution gridded map of aboveground woody biomass and canopy presence for the municipal boundaries of Boston, Massachusetts, prepared using satellite multispectral and aerial LIDAR observations in the summer of 2006–2007 (Figure 3.1) (Raciti et al., 2014). We classified canopy pixels according to their pixel buffer distance from canopy patch edges using the Expand tool in ArcMap 10.4 (ESRI, 2014), with all pixels within 10 pixels (approximately 10 m) of a canopy edge classified as "edge" canopy. We combined biomass, canopy, and canopy edge maps with 1 m maps of land-use/land-cover (LULC) classification and impervious surface presence/absence prepared from aerial photographs (MassGIS, 2005). The LULC categories were Forest, Developed (non-residential), High Density Residential, Low Density Residential, Other Vegetated, and Water, simplified from the LULC classification scheme used by MassGIS (2005) (Table 3.S1). To represent tree-scale and larger ecosystem dynamics, we then aggregated the data to generate 30 m spatial resolution gridded maps of total biomass, fractional canopy and canopy edge area, fractional impervious area, and LULC classification by greatest combined class area per pixel. We also examined the sensitivity of estimates to differing spatial methods for evaluating pixel-level biomass density. We calculated biomass density at the 30 m pixel scale (MgC ha^{-1}) as (1) the biomass C present versus pixel area under tree canopy (canopy basis) (e.g. Nowak et al., 2013); (2) biomass C versus total pixel area (ground basis) (e.g. Ouimette et al., 2018); and (3) biomass C versus non-paved pixel area (pervious basis).

2.2 Tree growth data

A linear mixed-model framework was used to estimate the relationship between stem diameter at breast height (DBH, cm) and growth rate (cm $tree^{-1}$ yr^{-1}) for measurements of trees growing in rural forests (Rural Forest), urban forest fragments (Urban Forest), and open-grown street, park, and backyard trees (Street Tree) (Table 3.S2). The Rural Forest growth model was based on repeated stem DBH measurements (n = 6,710 stems) from 2003–2015 in plots monitored under the USDA's Forest Inventory Analysis (FIA) program (USDA, 2019). The Urban Forest model was based on measurements in 2015 from eight forested test plots (n = 425 stems) located in nearby suburbs of Boston, subdivided based on their distance from long-lived canopy edges (<10m, 10–20 m, 20–30 m) (Reinmann and Hutyra, 2017). Rate of DBH change for Urban Forest was determined based on increment cores taken from a subset of stems in each plot (n = 195 cores). The Street Tree growth model was based on repeated measurements of stem DBH obtained for healthy live trees (n = 2,592 stems) growing along public rights-of-way in several zones across the city of Boston in 2006 and 2014 (Smith et al., 2019). Complete data collection protocols and discussion of model construction are available in the Supplemental.

2.3 Growth modeling

We used stem growth rates taken from the Rural Forest and Urban Forest models with the measured DBH of living stems present, via allometric equations, to determine the relationship between areal aboveground woody biomass density per test plot (MgC ha^{-1}) and its corresponding relative biomass gain rate (MgC yr^{-1} per MgC-biomass) (Tables 3.S2 and 3.S3; See Supplemental for allometric equations used and discussion of areal-basis growth model estimation). We then used the areal-basis growth models to predict annual rate of C gain in aboveground woody biomass for each 30 m map pixel by estimating relative biomass gain rate based on pixel biomass density, then multiplying the predicted biomass gain rate by pixel tree biomass C (MgC) to determine pixel annual biomass C gain (MgC pixel^{-1} yr^{-1}), with 1,000 bootstrap resamples of coefficients in the areal-basis models to estimate error. For the Urban Forest model, growth factors and biomass gain were estimated for the canopy edge (<10m) and interior (10–30 m) biomass component of each pixel separately, using only the per-ha-canopy areal basis for biomass density.

Because of the sampling design of the Street Tree observations it was not possible to directly estimate an areal-basis model for biomass growth. As an alternative, for each pixel a collection of trees was simulated by randomly drawing (with replacement) a selection of stems from the Street Tree DBH measurements taken in the city of Boston (2,592 tree records) to approximate total pixel biomass. Tree number was not fixed but tree collections were constrained to a maximum basal area of 40 m^2 ha^{-1}. This simulation method was repeated to obtain 100 valid collections per pixel, recording DBH and taxon for each tree in each collection. (See Supplemental on simulation of pixel-level stem collections). The Street Tree stem growth model was then applied to a randomly chosen pixel stem collection, using urban-specific allometric equations to estimate biomass change (McPherson et al., 2016) (Table 3.S4). This estimation approach was repeated for every pixel with 1,000 bootstrap resamples of the simulated stem collections and coefficients of the stem growth model, with the same growth model applied to all pixels in each resample. To complete the map-wide estimate of annual biomass C uptake, a composite "Hybrid Urban" estimate was generated by combining outputs of the Urban Forest model in pixels classed as "Forest" or containing >111 MgC ha^{-1} biomass with outputs of the Street Tree model for all other non-forest pixel types. This cutoff corresponded approximately to the biomass density of local rural forests (Fahey et al., 2005; Magill et al., 2004), and the threshold past which estimation based on the Street Tree simulation approach became computationally impractical. The Hybrid Urban results were contrasted to the annual biomass C uptake estimated using the Rural Forest model under both the canopy basis and ground basis for calculating biomass density.

2.4 Policy Projections

Three alternate scenarios for policies affecting urban ecosystem function were projected for 2006–2040 based on the simulated collections of street tree stems contained in Developed, HD Residential, and LD Residential pixels with <111 MgC ha^{-1} (77,955 pixels total). The three scenarios were: 1) Business as Usual (BAU) in which the 2006–2007 pixel simulations were projected to 2040 under assumptions of mortality risk and stem growth rate described above; 2) Preserve Largest (PL), in which mortality for all trees >40 cm DBH was reduced by 50% relative to their measured size-based annual mortality risk (Smith et al., 2019); and 3) Street Tree Planting (STP) in which approximately 170,000 small (5 cm DBH) street trees were added to the map total over the first 10 projection years, the maximum plausible ceiling of new trees that could be added based on the total non-canopied area available adjacent to Boston's surface streets. (See Supplemental for discussion of identifying plantable road buffer space).

For each pixel a randomly selected simulated stem collection was subjected to annual size-based mortality risk (Smith et al., 2019) and predicted growth rate based on the Street Tree growth model. In pixels that simulated a tree mortality, or pixels under the STP scenario that simulated a new tree planting, new or replacement trees were simulated with 5 cm DBH and a taxon randomly selected from a stem record in the Street Tree survey. The trajectory of annual biomass growth, total biomass, stem number, and canopy area was projected for each policy for each scenario year. Each scenario timeline was run with 100 bootstrap resamples of the stem growth model coefficients applied uniformly across scenarios to provide an uncertainty distribution for each metric while remaining computationally tractable (See Supplemental for discussion of on procedures used for policy projection).

2.5 Statistical analysis

We evaluated the significance of fixed effects in mixed models using a drop-one Chi-square test, with final models including the lowest-order polynomial with all terms significant ($p < 0.05$) (Zurr et al., 2011). Random effects for available covariates were fit for intercepts, as well as for slope terms whenever possible (Table 3.S2). All data processing was performed in *ArcMap* 10.4 (ESRI, 2014) and in the *R* software package (R Core Team, 2017) including the packages *lme4* (Bates et al., 2015), *raster* (Hijmans, 2017), *data.table* (Dowle and Srinivasan, 2017), and *rgdal* (Bivand et al., 2017). Due to skewed distributions, median values were reported with upper and lower limits of the central 95% of values, and growth models were reported with Residual Standard Deviance (RSD) as an indicator of fit.

3 Results and Discussion

3.1 Urban forest structure and distribution

Between LULC types there were distinct differences in the distribution of canopy area, degree of canopy fragmentation, and tree biomass, all of which can be expected to influence the annual rate of long-term C uptake to biomass. Canopy covered 25% of the total study area, of which 85% was within 10 m of an edge, the approximate equivalent of the width of 1–2 mature tree crowns (Pretzsch et al., 2015) (Figure 3.2). Developed and High-Density Residential areas covered 38% and 39% of the study area, respectively, containing 15% and 46% of total canopy area, of which 97% and 98% was within 10 m of an edge (Table 3.S5). Areas classed Forest occupied only 8% of the study area, but contained 26% of the total urban canopy and 32% of total biomass, of which only 50% was within 10 m of an edge.

The distribution of biomass and canopy coverage implies that while small tracts of Forest-classed land in Boston provide a disproportionate share of services related to canopy and biomass, trees present in the more extensive areas of human-dominated land cover also make a large contribution. Unlike in Forest-classed land, however, trees distributed in these developed and residential areas are likely to function nearly entirely under scattered open-grown condition. Additionally, 50% of biomass in even relatively intact Forest areas still may be under the influence of canopy edge effects. The co-occurrence of both fragments of clustered forest with extensive canopy edges and open-canopy scattered trees suggests that both types of growing contexts need to be accounted for in estimating urban forest ecosystem function.

3.2 Biomass gain in urban growth contexts

Local stem growth measurements showed growing context had an effect on annual rate of biomass gain per stem, indicating that urban trees may be expected to exhibit different C uptake dynamics depending on setting, and differing from local closed-canopy rural forests. Tree stem growth rate was highest and most variable in Street Trees, with median annual growth rate of 0.73 (-0.49–2.22) cm tree^{-1} yr^{-1} corresponding to median DBH of 25.9 (7.6–71.1) cm. The best-fit mixed model for Street Tree stem growth (RSD = 0.59) showed a significant decline in annual DBH increment with increasing DBH (Figure 3.3; Table 3.S2). In Urban Forest trees, median DBH increment of edge (<10 m) and interior stems was 0.45 (0.09–1.10) and 0.30 (0.06–0.71) cm tree^{-1} yr^{-1}, corresponding to median DBH of 18.7 (6.3–64.1) cm and 18.8 (7.3–40.7) cm, respectively. The Urban Forest model (RSD = 0.08) predicted faster stem growth than the Rural Forest model, and included a significant predicted increase in growth in stems growing within 10 m of a canopy edge. Growth rates in Street Trees and Urban Forest stems were comparable to the range observed for other trees growing along streets and in green spaces in Bolzano, Italy, (Russo et al., 2014); Leipzig, Germany (Strohbach et al., 2012); and Boston, USA (Briber et al., 2015).

In contrast to the urban-specific growth models, the Rural Forest model (RSD = 0.19) predicted slower stem growth than Urban Forest or Street Trees, with median growth rate of 0.20 (0–0.64) cm tree^{-1} yr^{-1}, corresponding to median DBH 22.6 (13.0–52.1) cm. The range and median of stem DBH in each growth context were similar, except for a lack of trees 5–12 cm DBH range in the Rural Forest due to sampling design. Unlike the Rural- and Urban Forest samples, the Street Tree sample included few conifers and a relatively large fraction of non-local taxa, including members of *Ginkgo, Gleditsia, Pyrus, Tilia* and *Zelkova* (Table 3.S4).

Projecting modeled stem growth rates for stems ≥5 cm DBH, median areal-basis growth rate in Urban Forest plots was 0.035 (-0.009–0.062) MgC yr^{-1} per MgC-biomass in edge subplots (<10 m) and 0.024 (-0.010–0.054) MgC yr^{-1} per MgC-biomass in interior subplots (10–30 m) (Table 3.S2). These growth rates corresponded to plot biomass density of 103.7 (87.8–292.4) and 87.5 (53.8–167.0) MgC ha^{-1} in edge and interior subplots, respectively, based on the total biomass in stems ≥5 cm DBH measured in 2015 in each plot. Both edge and interior subplots showed a significant negative effect of biomass density on areal-basis growth rate, with a significantly lower intercept for interior plots. In Rural Forest plots, areal-basis biomass growth rate was 0.018 (0.004–0.069) MgC yr^{-1} per MgC-biomass with median plot biomass density of 86.4 (33.6–193.0) MgC ha^{-1}. Rural Forest plots showed a significant negative effect in log-biomass growth rate with increasing plot biomass density.

3.3 Effect of biomass density areal basis

This study used areal biomass density (MgC ha^{-1}) to predict local C uptake rate to long-lived biomass. In non-urban forest ecosystems this areal biomass density is in part a product of stand age and successional status, which are also predictive of the rate of net biomass gain in the stand (Ryan et al., 1997). In the scattered canopy and mixed impervious cover of Boston's urban forest, however, the areal basis used in determining biomass density for any given pixel faced potential ambiguity, making the calculated C uptake sensitive to the areal standard chosen. An example of typical discontinuous urban canopy in the study area shows that at moderate levels of both canopy and impervious cover, estimates of biomass density in a given area varied from 22.4 MgC per ha-ground to 89.0 MgC per ha-canopy to 179.3 MgC per ha-pervious (Figure 3.4). In the same sample area mean Landsat 30 m NDVI was 0.40 (0.22–0.57), comparable to partially vegetated areas, though the area contains appreciable biomass. The comparatively low biomass density on a per-ha-ground basis stood in contrast to the per-ha-pervious density basis, showing unrealistically high biomass density probably resulting from large areas of tree biomass growing over impervious cover.

Because of this areal-basis ambiguity, Rural Forest results using the ground-basis (raw pixel area) for biomass density gave a higher total estimate for biomass C uptake than canopy-basis calculations (Table 3.1). This result, while closer to the Hybrid Forest model accounting for urban growth rates and growing context, likely does not reflect underlying urban-affected ecosystem dynamics but is rather an artifact of the calculation basis. The lower biomass density calculated on the ground-basis would tend to generate higher predicted rates of relative biomass gain per pixel, with growth parameters more akin to an early stage of forest succession containing more, smaller, faster-growing trees rather than reflecting the true condition of fewer, discontinuous, larger trees.

3.4 Estimates of annual biomass C uptake

Applying the combined Hybrid Urban model to tree biomass distribution across the city of Boston, we estimated considerably higher annual tree biomass C uptake compared to estimates based on rural growth rates (Rural Forest). The Hybrid Urban model estimated C uptake to long-lived biomass of 10.9 (6.7–16.2) GgC yr^{-1}, with a median uptake rate per pixel of 0.5 (0–3.1) MgC ha^{-1} yr^{-1} across the study area (Table 3.1). The largest total biomass gains accrued to the Forest, Developed, and HD Residential land use types. By comparison, applying Rural Forest growth factors to per-ha-canopy biomass density showed lower biomass gain in all land use categories, with a median total of 4.8 (3.6–6.4) GgC yr^{-1} and a greater relative fraction of total biomass gain accruing to Forest-classed areas. This reduced estimate of C uptake, particularly in non-Forest cover types, is partly the result of lower per-stem and per-area biomass gain in Rural Forest context than in Urban Forest or Street Trees. In contrast to C uptake on the basis of ground area, aggregating to the total amount of canopy area city-wide shows annual biomass uptake figures were 3.5 (2.1–5.2) MgC per ha-canopy in the Hybrid Urban compared to 1.5 (1.1–2.0) MgC per ha-canopy in the Rural Forest model. The Hybrid Urban results are somewhat lower than tree C uptake per ha-canopy estimated in Los Angeles and Sacramento (McPherson et al., 2013), but may reflect the effects of different species present, growing season length, and climatic conditions. The California study does, however, confirm the relatively high C uptake potential of trees present in mature residential neighborhoods. In contrast, the C uptake estimates from this study are generally higher than the estimate reported for the city of Boston developed under the UFORE method of 2.3 (1.8–2.8) MgC per ha-canopy (Nowak et al., 2013). The Rural Forest model applied to per-ha-ground biomass density produced somewhat higher map-wide total C uptake estimates (Table 3.1) and higher estimates of C uptake per pixel (not shown), but this was likely an artifact of the biomass density calculation.

The distribution of pixel median estimates was higher in every LULC category under the Hybrid Urban model (Figure 3.5). Much of the variation among LULC categories in per-pixel median C uptake was a result of the underlying distributions of pixel biomass. However, persistently higher growth rates modeled for street trees and urban forest fragments in the Hybrid Urban model also contributed to both greater overall spread in per-pixel estimates and higher median biomass C uptake in each LULC category. Much of the HD- and LD Residential pixel population had estimated C uptake at least as large as Forest-classed pixels, even after accounting for higher growth in forest edge biomass. The potential for large biomass C uptake rates in some high-biomass non-forest pixels implies that parts of urban Boston not recognized as forested may be responsible for as at least as much C uptake per ha as local urban forest fragments.

3.5 Policy effects on ecosystem function

Policies for preserving larger trees (PL) and for expanding street trees numbers in plantable roadside areas (STP) resulted in differential gains in biomass C uptake, total biomass, and canopy cover by 2040 relative to Business-as-usual BAU, had these different policies been implemented starting in 2006 (Figure 3.6). Median projected annual C uptake by 2040 was highest under STP at 7.1 (3.6–11.8) GgC yr^{-1} and rose relatively rapidly over the initial 10 years of simulated tree planting, but also continued to rise under PL up to 6.7 (2.8–14.1) GgC yr^{-1}, compared to BAU which declined slowly to 5.9 (2.9–10.4) GgC yr^{-1}. In contrast, projected biomass and change in canopy cover change relative to 2006 both rose most mostly rapidly under PL, reaching a median of 236 (148–343) GgC and +25% (-6–54%), compared to more modest increases under STP to 191 (129–257) GgC and +15% (-8–37%) by 2040, respectively. Under BAU by comparison, 2040 median projected biomass remained roughly stable at 173 (117–235) GgC, and showed a median stable canopy cover change of 0% (-20–20%). The variability in the projected results reflects the stochastic occurrence of individual tree mortalities in each pixel simulation, variability in the simulated collections of tree stems present at the pixel level, and estimation error in the underlying Street Tree growth model.

Differential changes in urban forest demographics likely caused these divergent policy effects on the ecosystem functional metrics. Under the PL policy, simulator results from 2006–2040 showed the cumulative sum of mortality events was lower (487 × 10^3 [473–508 × 10^3]) and final 2040 city-wide number of living trees was somewhat higher (552 × 10^3 [550–554 × 10^3]) compared to BAU mortalities (583 × 10^3 [578–592 × 10^3]), and final number (546 × 10^3 [545–548 × 10^3]). These results likely reflect the reduction in tree mortality and higher equilibrium tree population expected under PL as the simulated tree populations matured into larger DBH classes >40 cm with lower mortality as a result of the policy. Since the policy simulations all assumed complete replacement of dead trees with new small trees, total mortalities could be comparable to total living trees as the result of this ongoing turnover in the tree population (Supplemental). The greater percentage of high-biomass/high-canopy area trees under PL is therefore likely the cause of the greater projected gains in 2040 biomass and relative canopy change. In contrast, under the STP policy median tree number expanded to 666 × 10^3 (665–668 × 10^3) with 126 × 10^3 (125–126 × 10^3) new live stems installed in suitable areas of road buffer. Though these greater stem numbers lifted total mortalities under STP (700 × 10^3 [694–708 × 10^3]), the addition of new growing biomass also caused median annual biomass C uptake by 2040 to exceed median uptake under PL. However, the addition of smaller trees under STP was not sufficient to surpass the median projected gains in live biomass and canopy cover predicted with the shift to a higher fraction of larger trees under PL. Overall stability, or potential loss, in canopy cover and biomass C uptake in the absence of these policy interventions under BAU, even with prompt and complete replanting of mortalities, could be a product of mortality losses of vulnerable larger trees causing a demographic shift towards smaller more recently planted stems (Smith et al., 2019).

Our assumption of no canopy overlap or other interferences on canopy area growth may tend to overestimate canopy cover at higher biomass or building density and at the extreme upper end of the range of individual stem DBH. The prediction of a continued strong upward trend in growth in canopy area under PL may as a consequence somewhat overestimate the potential for continuous expansion in canopy cover as the result of continuous canopy growth in large-diameter trees across the city. Similarly with annual C uptake and total biomass, there is likely an upper limit to the size and growth rate of large urban trees such that continued positive trends in these metrics under PL may not be maintained over a sufficiently long time scale. Conversely, the positive functional trends under STP represent the outcomes of an aggressive program of tree expansion, simultaneous with the relatively rapid and complete replacement of ongoing tree mortalities. However, the practical implementation of and scope for urban tree planting programs in Boston and elsewhere remain uncertain and the topic of study (Danford et al., 2014; O'Neil-Dunne, 2017). The functional trends under PL and STP may therefore represent the upper envelope for the magnitude of impacts under policies similar to these. While marginal adjustments to the assumptions of the projections might alter the relative performances of PL and STP, the simulation results do suggest, however, that either policy intervention would lead to greater values in these ecosystem functional metrics relative to BAU over time.

4 Conclusions

The results of this study highlight the impact that altered ecosystem functions in urbanized landscapes might have on some of the services performed by urban vegetation. Scaling up local measurements of stem growth rate with reference to canopy configuration, we find that estimated biomass C uptake in the city of Boston could be substantially greater than estimates treating tree growth as similar to rural forest analogues. Accounting for this urban growth context in C uptake requires putting traditional ecosystem metrics like biomass density and canopy edge configuration into its realistic spatial context, given the heterogeneity and fragmented nature of the urban forest. These differences in function have implications for municipal policy toward managing and optimizing their services. Projecting different urban tree policies through 2040, we find that preserving larger trees may tend to maximize the functions of canopy cover and biomass C storage, while new tree planting may help maximize biomass C uptake capacity. The present uncertainties in quantifying urban ecosystem function or in predicting responses to policy call for more complete and frequent monitoring of basic indicators of urban forest function, such as regular urban street tree census and aerial observations of canopy extent (O'Neil-Dunne, 2017).

Though remaining forest fragments in Boston contained a relatively large fraction of total biomass and canopy coverage given their small areas, the bulk of urban tree biomass was present in densely developed residential areas. As such, this type of land cover/use is likely to host to a significant portion of some of the ecosystem services provided by the city's urban trees. The large extent of this open-canopy "urban savannah" dominated by trees in planters, private yards, and along streets implies that municipal-scale policy focused only on identifiable green spaces like parks and preserves will fail to address services provision by a large portion of urban tree biomass and canopy extent—particularly services like temperature moderation whose value is limited by proximity to people (Ziter et al., 2019). The results of our policy projections offer hope that optimizing local ecosystem services could be achieved by addressing uniquely urban factors of tree growth and demographics, such as heightened mortality, uneven stand age structure, and simple lack of trees in available growing space. In addition, the finding of potentially declining functional indicators under a "Business-as-Usual" policy prescription also underlines the reality that urban forests are dynamic systems, facing both the combined effects of changing global climate and intensifying local urban climate effects. Even maintaining present services may require active social intervention over the next few decades.

Our study suggests that though biogenic C uptake in some parts of the city may be comparable to rates in intact forest, these localized C sinks do not in sum amount to a large overall offset to Boston's CO_2 emissions, with annual tree CO_2-equivalent uptake at a maximum of 0.8% of the total 6.9 million tonnes of CO_2-eq emissions for the city in 2016 (City of Boston, 2016). On the other hand, cities that have made emissions reductions pledges also face the need to monitor progress towards these goals. Unfortunately, atmospheric methods under development for monitoring regional urban CO_2 emissions still face considerable ambiguity during the growing season due to interference from poorly quantified and spatially resolved urban biogenic C fluxes (Sargent et al., 2018). Resolving and contextualizing these potent but spatiotemporally localized sinks (Hardiman et al., 2017; Miller et al., 2018), could directly benefit these emissions monitoring efforts. A more complete accounting of urban biogenic C flux would estimate not only short- and long-term C uptake by tree tissues but also non-tree vegetation C uptake, while incorporating auto- and heterotrophic respiration C release processes that also vary in time and space and in response to specific urban conditions (Decina et al., 2016; Wang et al., 2017). Future research should quantify these important urban biogenic C flux components and their relationships with urban forest ecosystem services more broadly to provide an improved spatiotemporal picture of urban biogeochemical C cycling—one that will advance our capacity to monitor anthropogenic C emissions and better assess progress in mounting municipal-scale climate change responses.

Acknowledgments

This work was supported by the National Oceanic and Atmospheric Agency grant NA14OAR4310179 and the National Aeronautics and Space Administration grant NNX16AP23G. The authors acknowledge Dr. Steve M. Raciti for the public availability of the biomass and canopy data as well as consultation he provided on their construction. The authors also acknowledge Dr. Chloe Anderson, Dr. Kira Sullivan-Wiley, and Ana Reboredo Segovia for comments on early drafts of this work.

Figure 3.1: Boston study area showing canopy distribution (green) and study area outline (image courtesy of Google Earth).

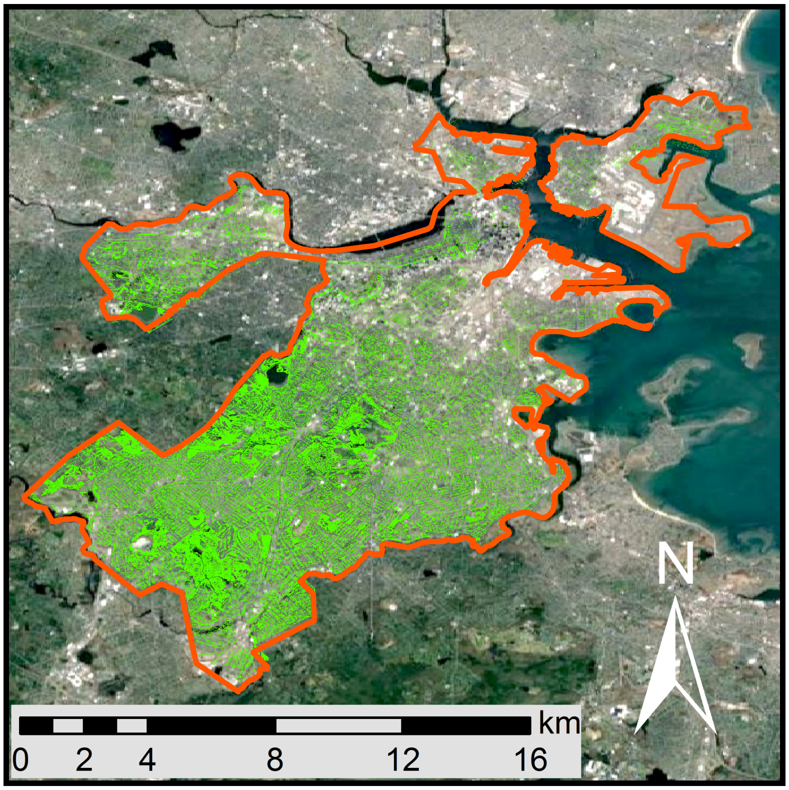

Figure 3.2: Land-use/land-cover and distribution of canopy area by distance from canopy edge in Boston study area.

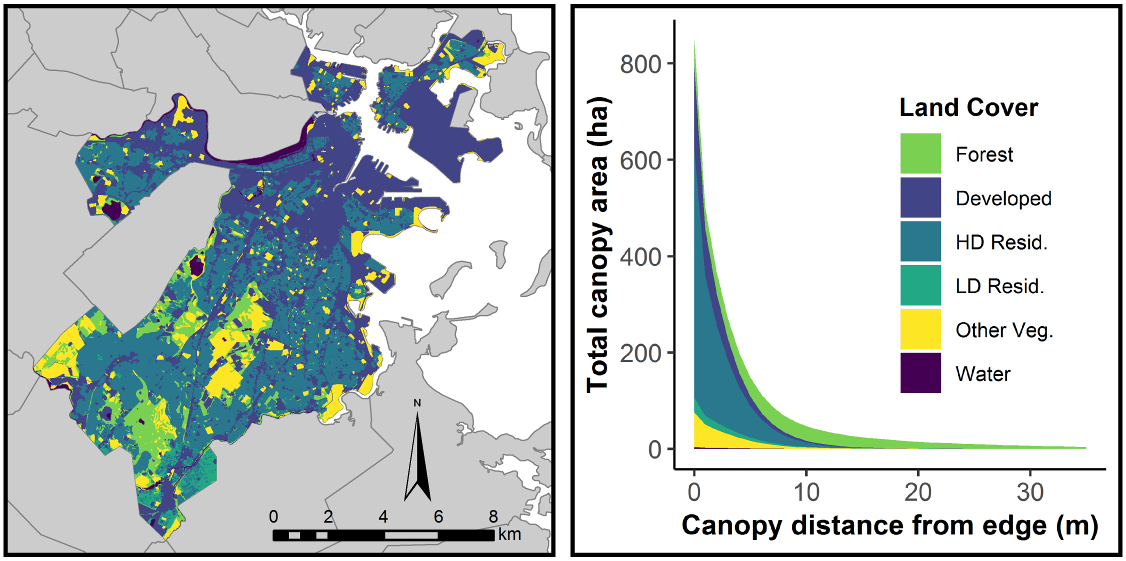

Figure 3.3: Stem DBH and DBH increment for Rural Forest (L), Urban Forest (C) and Street Tree (R) contexts. Thick dashed lines show predicted mean response with fixed effects, thin dashed lines show central 95% of predictions given model error.

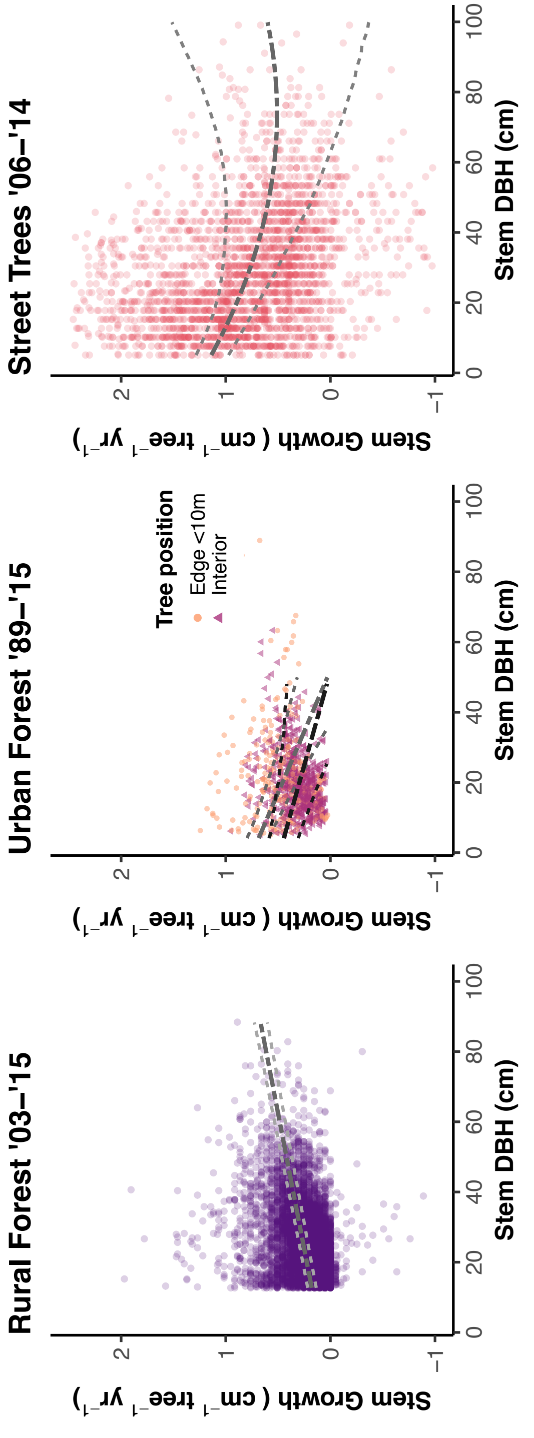

Figure 3.4: (A) Distribution of vegetation and cover in the study area; (B) Aerial photo of inset area in South End neighborhood (courtesy of USDA National Agriculture Imagery Program); (C) Vegetation and cover type in inset: Canopy over pervious, canopy over impervious, non-vegetated impervious, non-vegetated pervious, vegetated pervious (non-canopy), and open water. Text figures correspond to features of inset area.

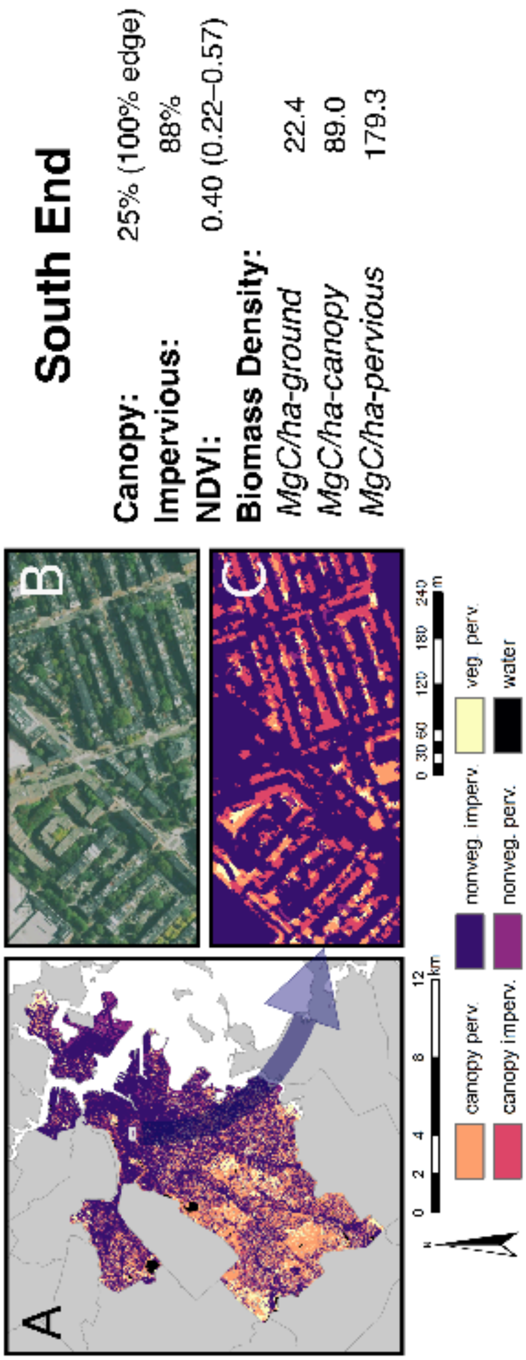

Figure 3.5: Pixel median biomass C uptake rate (MgC ha^{-1} yr^{-1}) for Hybrid Urban model (dark) and Rural Forest model, canopy basis (light). Box width is proportional to total area and show central 50% of data in each LULC category (other data not shown).

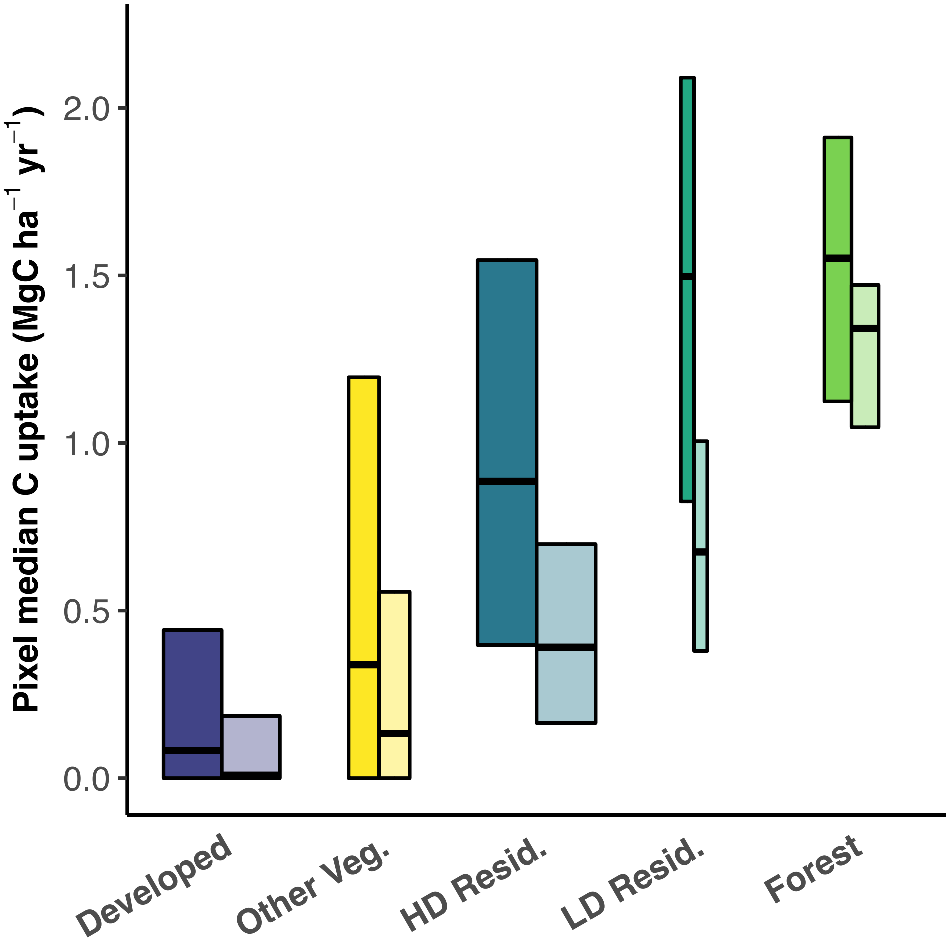

Figure 3.6: Median projections of annual net C uptake (top), total tree biomass (middle) and change in canopy area from 2006–2040 (bottom) in non-forested Developed, HD Residential, and LD residential pixels. Scenarios tested were Business-as-usual (BAU), Preserve Largest (PL) and Street Tree Planting (STP) from 2006–2040.

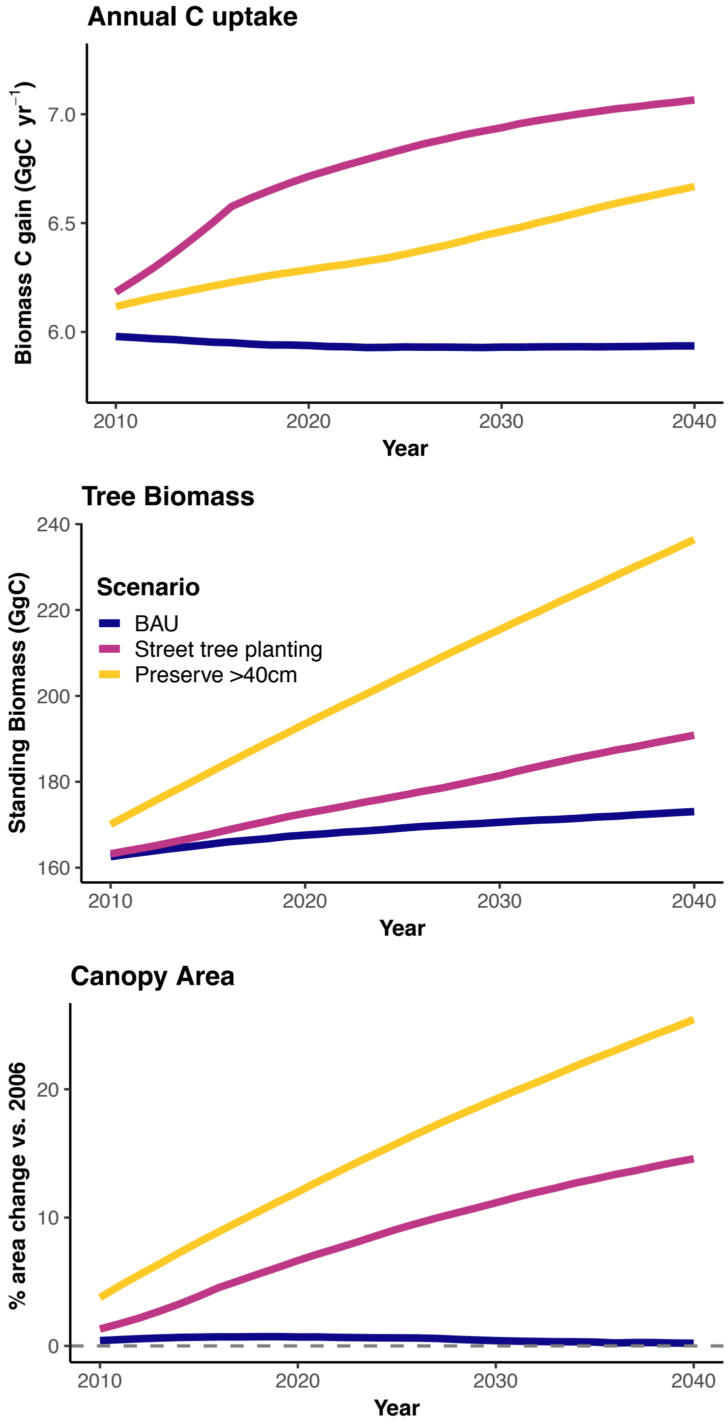

Table 3.1: Estimated city-wide annual biomass C uptake, and distribution of median per-pixel rate of C uptake (central 95%). Relative areas of LULC types are Forest: 8%; Developed: 38%; HD Resid.: 39%; LD Resid. 2%; Other Veg.: 11%; Water: 2%; Total area: 12,455 ha (See Table 3.S5).

Land use/cover	**Biomass C uptake (GgC yr^{-1})**			**Median pixel C uptake (MgC ha^{-1} yr^{-1})**	
	Hybrid Urban	*Rural Forest, canopy basis*	*Rural Forest, ground basis*	*Hybrid Urban*	*Rural Forest, canopy basis*
Forest	2.2 (1.0–5.0)	1.2 (0.9–1.7)	1.4 (1.1–1.9)	2.2 (0.6–3.5)	1.3 (0.3–1.6)
Developed	1.8 (1.0–2.5)	0.7 (0.5–0.9)	1.1 (0.9–1.4)	0.1 (0–2.1)	0 (0–1.0)
HD Resid.	5.3 (2.9–7.8)	2.2 (1.7–3.0)	3.5 (2.8–4.3)	0.9 (0–2.7)	0.4 (0–1.3)
LD Resid.	0.4 (0.2–0.6)	0.2 (0.1–0.2)	0.2 (0.2–0.3)	1.5 (0.2–3.5)	0.7 (0–1.4)
Other Veg.	1.0 (0.6–1.4)	0.4 (0.3–0.5)	0.6 (0.5–0.8)	0.3 (0–3.2)	0.1 (0–1.3)
Water	0.1 (0–0.1)	0 (0–0)	0 (0–0.1)	0 (0–2.5)	0 (0–0.1)
Total	**10.9 (6.7–16.2)**	**4.8 (3.6–6.4)**	**7.0 (5.6–8.7)**	**0.5 (0–3.1)**	**0.2 (0–1.5)**

Supplemental Information for *Current and future biomass carbon uptake in Boston's urban forest*

3.S1 Field data for tree growth rates and growth model development

Growth estimates for typical non-urban forests (Rural Forest) were based on repeated stem DBH measurements from 2003–2015 in plots monitored under the USDA's Forest Inventory Analysis (FIA) program (USDA, 2019). Plots were selected from locations east of Interstate 495 and within 100 km of the metropolitan core of Boston, excluding the Cape Cod region due to its significantly different soil makeup (high sand content) and forest type (*Pinaceae* dominated). Stem DBH within up to four circular 14.6 m diameter subplots in each plot in successive measurement periods was recorded for every healthy live tree ≥12.7 cm DBH, excluding stems in subplots with <5 stems surviving across both intervals (n = 6,710 stems). Biomass change rate at the plot level was calculated as biomass change in hardwood taxa relative to total plot biomass, excluding plots with <25% total hardwood biomass (n = 297 paired plot measurements). In Rural Forest live biomass density and the annualized rate of biomass change was directly estimated for each plot using taxa-specific allometric equations applied to starting DBH and annualized DBH change measures in each plot (Chojnacky et al., 2014; Jenkins et al., 2003) (Table 3.S3).

To represent growing conditions in urban forest fragments (Urban Forest) we used observations from eight forest-edge test plots located in nearby suburbs of Boston, MA, subdivided based on the distance from long-lived canopy edges (<10m, 10–20 m, 20–30 m) (Reinmann and Hutyra, 2017). Stem DBH and distance from canopy edge were recorded in 2016 for all live stems ≥5 cm DBH (n = 425 stems). As repeated DBH measurements were not available in the Urban Forest plots, rate of stem DBH change was estimated using increment cores extracted from a subset of tree stems in each plot (n = 195 cores). Average annualized DBH change across five successive intervals (beginning 2011, 2006, 2001, 1996, and 1989–1991) of approximately five years duration were determined for each core and compared to the starting DBH of each interval to estimate the relationship between DBH and annualized DBH change in stems growing in both edge (<10 m) and interior (10–30 m) plot segments (n = 900 stem increment intervals). This five-year interval was selected for consistency with measurement intervals in the other growth contexts in this study. In Urban Forest, the areal-basis rate of biomass change with respect to subplot biomass density and edge position (<10 m vs. 10–30 m) was projected for the complete stem record measured in 2015 using the Urban Forest stem growth model and allometric equations used for Rural Forest, with 1,000 bootstrap resamples of the stem model coefficients to provide a sampling distribution for areal-basis model coefficients. (Table 3.S3). A single set of areal-basis growth model coefficients was randomly selected from their respective distributions in each model realization to provide a sampling distribution of coefficients under Urban Forest conditions.

To represent conditions for open-grown street, park, and backyard trees (Street Trees), successive measurements of stem DBH were obtained for healthy live trees (n = 2,592) growing along public rights-of-way in several measurement zones across the city of Boston in 2006 and 2014 (Smith et al., 2019). A small number of negative growth estimates are present in this data set, possibly an artifact of ambiguities in replicating measurement height between the two sampling events or occasional errors by volunteers. The relationship between DBH and annualized DBH change was estimated and the model coefficients with sampling distributions were recorded (Table 3.S3). For developing the Street Tree model of stem growth rate, related street tree taxa were grouped and taxonomic groups were used to account for the random effect of taxon. Urban-specific wood volume and density allometric equations were applied to related taxa where possible (Table 3.S4). Wood density for all "Urban General Broadleaf" classed stems was set at 549 kg m^{-3}, the weighted mean of wood densities for each of the constituent taxa included under this heading from the Street Tree growth records (Chave et al., 2009; Zanne et al., 2009). Unlike for the Rural Forest and Urban Forest samples, it was not possibly to directly estimate areal-basis growth models given the spatial distribution of the Street Tree stem measurements (See below for discussion of biomass simulation method).

Model terms were selected parsimoniously to include only significant terms that improved model fit compared to simpler models. Higher order polynomial terms were tested and included only when all coefficients were significant ($p < 0.05$). Random effects (slopes and intercepts) were included where possible to maximize variance accounted for while achieving adequate model convergence. Areal-basis growth model error did not incorporate (unknown) source of error inherent in application of allometric equations for biomass, nor error in estimations of standing biomass at the map level. To prevent application of unrealistically high or low growth factors to map pixels with extreme biomass density values, the predicted pixel-level growth factors in any given realization of the Urban Forest model were restricted to within one standard deviation of the mean of the projected maximum and minimum subplot-level growth with respect to edge distance

(0.005–0.087 MgC yr^{-1} per MgC-biomass for edge biomass, 0.006–0.049 MgC yr^{-1} per MgC-biomass for interior biomass). Biomass density for use in predicting pixel annual biomass grown under the Urban Forest model was determined on the canopy-area basis. Growth factors using the Rural Forest model were similarly restricted to within the minimum and maximum observed subplot-level growth rate (0.002–0.131 MgC yr^{-1} per MgC-biomass).

3.S2 Street tree biomass simulator and growth estimation

Biomass in each 30 m pixel was simulated as a collection of stems randomly drawn with replacement from the 2,592 surviving street trees surveyed in 2006 and 2014 (Table S4). The total biomass of each stem collection was estimated as the sum of stem biomass calculated using taxa-specific urban tree growth allometric equations (McPherson et al., 2016). Simulations of per-pixel number, taxa, and DBH of selected stems in each collection were recorded only when total predicted aboveground biomass was within the smaller of 10% or 100 kg of the pixel biomass, and when total basal area per pixel (determined on basis of pixel area under tree canopy) was below 40 m^2 ha^{-1}, the highest subplot basal area observed in the Urban Forest sample (Reinmann and Hutyra, 2017). Simulation in each pixel was attempted until 100 successful tree collections were recorded or until simulation was deemed impossible. In the final Hybrid Urban model results, biomass growth estimates derived from the Urban Forest model were substituted for any non-forest pixels >20,000 kg biomass (>111 MgC ha^{-1}) and for any non-forest pixels that failed to identify at least 40 successful street tree collections.

3.S3 Policy projections 2006–2040

Every map pixel <20,000 kg biomass (<111 MgC ha^{-1}) and classed as Developed, HD Residential, and LD residential was subjected to projection of policy effects on urban forest function. In every iteration of a given scenario projection, one of the simulated Street Tree stem collections was randomly drawn for each pixel from the central 95% of simulated biomass and a set of Street Tree growth model coefficients was randomly drawn from their respective error distributions. Each pixel stem collection was then subjected to annual growth according to the selected Street Tree model of size-to-growth rate and to a predicted annual mortality risk % (R) based on stem DBH (Smith et al., 2019):

$$(1) \qquad R = 0.0008133 \times DBH^2 - 0.0642407 \times DBH + 4.0614503$$

Trees that simulated a mortality in each pixel simulation were projected to be replaced with 5 cm DBH saplings of a genus randomly selected from the Street Tree record, with a randomly assigned replanting delay of 0–2 years. For each year in the simulation from 2006–2040, total biomass, biomass gain and canopy area were calculated. Biomass and biomass gain in each simulation year were calculated similar to described for the Street Tree biomass simulator approach. Canopy area per pixel was calculated as the sum of per-stem canopy area assuming circular canopy geometry and estimating canopy diameter from DBH in each surviving stem using the taxa-specific urban allometric equations for open grown trees in MacPherson et al. (2016). This approach assumed no canopy overlap and no growth inhibitions due to nearby buildings, other trees, pruning, or other effects. As the absolute value of the canopy area prediction likely represented the maximum case, we normalized within-scenario canopy coverage predicted for 2006 to evaluate the potential for relative canopy area change across the simulation window, rather than absolute canopy area. In each pixel for each simulator year C uptake, total biomass, canopy area, live stem number, mortalities, and stem additions was recorded. Projections for each pixel were repeated 100 times per scenario, with a randomly chosen pixel stem collection and applying a consistent set of randomly selected stem growth model coefficients to each pixel in all three scenarios.

3.S4 Identifying plantable road buffer area

For the Street Tree Planting (STP) scenario, we determined plantable area as follows using ArcMap 10.4: A shapefile for all road centerlines for the city of Boston (MassGIS, 2005) was buffered at 6 and 4 m for roads of class 5, representing small residential roads, and at 10 and 8 m for roads of class 2, 3, and 4, representing larger arterials and multi-lane roads. Roads of class 1 (representing large divided state and federal highways) and class 6 (representing driveways, paths, and alleyways) were excluded from the analysis. Plantable space polygons were defined as the 2 m-wide strip between the inner and outer road centerline buffers, and then converted to a 1 m raster on the same grid as the 1 m canopy cover raster. The tree canopy raster was buffered by 4 pixels (approximately 4 m) using the Expand function and overlaid on the 1 m plantable space and LULC rasters. Plantable space pixels were eliminated that were either within the 4 m buffer of existing tree canopy or were not classified as Developed, HD Residential, or LD Residential. Plantable space pixels were then converted back to simplified polygons, and polygons < 2 m^2 in area were eliminated as too constricted to allow new planting (Figure 3.S1). The amount of new tree stems that could be added to each plantable space polygon was calculated as 1 + the perimeter of the polygon divided by eight, rounded down to the nearest integer, or roughly the number of stems plantable every 8 m along the linear distance of the buffer strip, starting at the end of the polygon. This calculation maintains an approximate 8 m minimum separation between new trees stems and a minimum 4 m radius to any existing tree canopy (Pretzsch et al., 2015). The total number of new potentially plantable street tree stems for the whole city was determined as 170,147, corresponding to 1,197 km of available plantable road buffer space. This estimate is comparable to but somewhat higher than the projection of approximately 120,000 available street margin planting areas based on tree survey data from 2006 (Danford et al., 2014), though our estimate assumed greater tree spacing and allowed for buffering distance from existing tree canopy. During policy simulation of the STP scenario each pixel was randomly assigned a new planting based on results of a binomial draw each year during the first 10 simulation years, with the likelihood of a new stem appearing set to the likelihood required to produce 170,147 new stem appearances in aggregate across all simulated pixels. New street tree stems consisted of an additional 5 cm DBH stem appearing of with a taxon randomly drawn with replacement from the Street Tree data set. After a new stem appeared in a pixel simulation, that stem was subjected to predicted biomass and canopy growth and mortality risk similar to other stems in each pixel collection.

Figure 3.S1: Example of identified plantable space (purple) along residential roads (gray), with space allowed for 4m buffer to nearest existing tree canopy (light green).

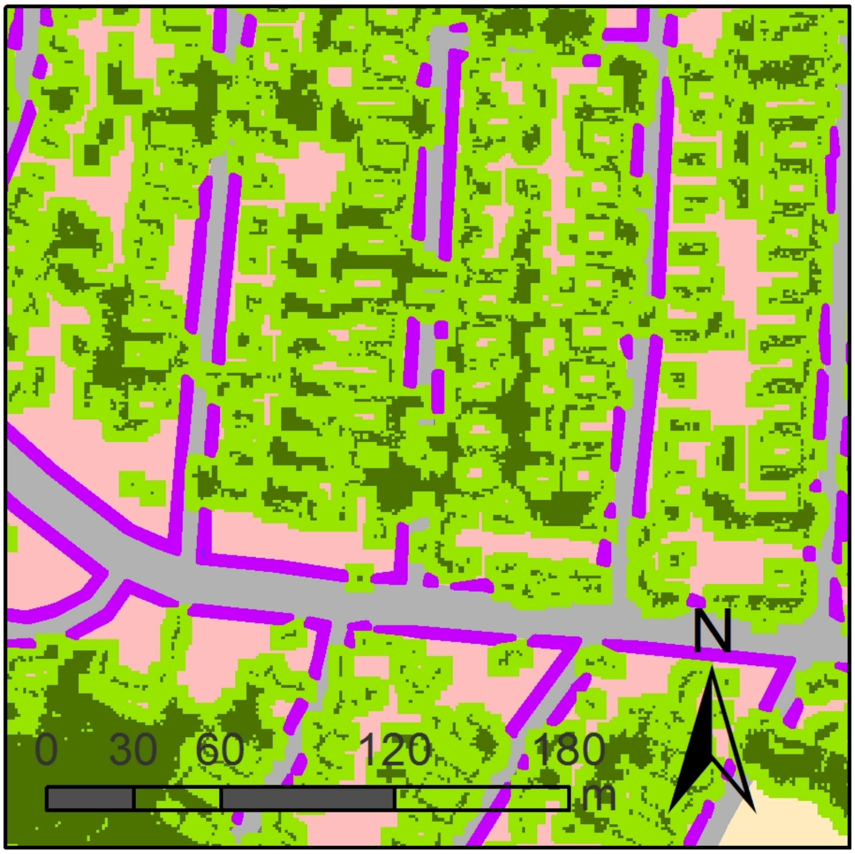

Table 3.S1: LULC cover classes used in this study (MassGIS, 2005).

LULC	Constituent Classes	Key Characteristics
Developed	Mining, Spectator Recreation, Commercial, Industrial, Transitional, Transportation, Waste Disposal, Marina, Urban Public/Institutional, Nursery, Junkyard	Non-residential, dominated by built or disturbed cover
HD Residential	Multi-family Residential, High Density Residential	Residential, apartment buildings or free-standing houses on small lots <1,000 m^2
LD Residential	Medium Density Residential, Low Density Residential, Very Low Density Residential	Residential, free-standing houses on lots up to >4,000 m^2
Forest	Forest, Forested Wetland	Coniferous and deciduous forests, tree canopy >50%
Other Vegetated	Cropland, Pasture, Non-forested Wetland, Open Land, Participation Recreation, Water-based Recreation, Saltwater Wetland, Saltwater Sandy Beach, Golf Course, Brushland/Successional	Non-forest, dominated by pervious and vegetated cover
Water	Water	Open water

Table 3.S2: Model summaries for stem- and areal-basis growth rate. Values in parentheses show coefficient standard error. RSD indicates model residual standard deviance. * significant at $p<0.05$, ** significant at $p<0.01$, *** significant at $p<0.001$ by Chi-squared test versus model excluding the term. Significance of coefficients for Urban Forest plot annual growth tested via Student's t test (H_0: $B_i=0$), and RSD is indicated for model fit determined using mean model coefficients. Model intercepts were not evaluated for significant difference from zero. Random effects for stem annual growth were: Urban Forest – Plot, Stem ID (intercept + DBH slope); Street Trees – Taxon (intercept + DBH slope); Rural Forest – Plot, taxon, sample year (intercept). Radom effects for plot annual growth: Urban forest – none; Rural Forest – Plot, Sample year (intercept).

Model	**N**	**Model Coefficients**	**Formula**	**RSD**
Stem annual growth: DBH increment (cm tree^{-1} yr^{-1}) ~ starting DBH (cm)				
Urban Forest	900	B_0: 0.744 (0.034);	DBH-incr. ~ B_0+B_1*DBH+B_2(interior)+B3(DBH*interior)	0.08
		B_1: -0.014*** (0.003);		
		B_2: -0.261 (0.050)***;		
		B_3: 0.005 (0.002)*		
Street Trees	2,592	B_0: 1.234 (0.008);	DBH-incr. ~ B_0+B_1*DBH+B_2*DBH^2	0.587
		B_1: -0.020 (0.004)**;		
		B_2: 1.33 E-04 (3.37 E-05)***		
Rural Forest	6,710	B_0: 0.096 (0.022);	DBH-incr. ~ B_0+B_1*DBH	0.194
		B_1: 0.006 (0.0003)***		
Plot annual growth: Relative growth (MgC yr^{-1} per MgC-biomass) ~ biomass density (MgC ha^{-1})				
Urban Forest	24	B_0: 0.056 (0.012);	Rel. growth ~ B_0+B_1*Density+B_2(interior)	0.01
		B_1: -1.69 E-04 (4.93 E-05)***;		
		B_2: -0.016 (0.008)***		
Rural Forest	297	B_0: -3.325 (0.098);	Log(Rel. growth) ~ B_0+B_1*Density	0.225
		B_1: -0.008 (0.001)***		

Table 3.S3: Rural and Urban Forest taxa present in stem DBH samples. All equations taken from Chojnacky et al. (2014) unless noted. Numbers in parentheses for Urban Forest indicate number of increment cores represented. Specific gravity (spg) in g cm^{-3}.

Taxon	N	Allometric equation
Rural forest		
Acer rubrum	2,153	Aceraceae, <0.50 spg
Acer saccharum	78	Aceraceae, >=0.50 spg
Betula alleghaniensis	115	Betulaceae, 0.50-0.59 spg
Betula lenta	206	Betulaceae, >0.60 spg
Betula papyrifera	98	Betulaceae, 0.40-0.49 spg
Fraxinus americana	101	Oleaceae, <0.55 spg
Pinus rigida	23	Pinus, >=0.45 spg
Pinus strobus	1,447	Pinus, <0.45 spg
Prunus serotina	78	Rosaceae
Quercus alba	296	Fagaceae, deciduous
Quercus coccinea	209	Fagaceae, deciduous
Quercus rubra	665	Fagaceae, deciduous
Quercus velutina	344	Fagaceae, deciduous
Tsuga canadensis	388	Tsuga, <0.40 spg
Other spp.	509	Mixed Hardwood (Jenkins et al., 2003)
Urban Forest		
Acer rubrum	27 (2)	Aceraceae, <0.50 spg
Acer saccharum	1	Aceraceae, >=0.50 spg
Betula pendula	2	Betulaceae, 0.40-0.49 spg
Betula populifolia	12	Betulaceae, 0.40-0.49 spg
Fraxinus americana	3	Oleaceae, <0.55 spg
Juniperus virginiana	56	Cupressaceae, >=0.40 spg
Pinus rigida	21 (7)	Pinus, >=0.45 spg
Pinus strobus	47 (16)	Pinus, <0.45 spg
Prunus serotina	20	Rosaceae
Quercus alba	8 (3)	Fagaceae, deciduous
Quercus coccinea	35 (33)	Fagaceae, deciduous
Quercus rubra	39 (29)	Fagaceae, deciduous
Quercus velutina	144 (105)	Fagaceae, deciduous
Tsuga canadensis	1	Tsuga, <0.40 spg
Other spp.	9	Mixed Hardwood (Jenkins et al., 2003)

Table 3.S4: Street Tree taxa present in Street Tree sample, number of stems represented, and biomass allometric equations applied. Allometric equations taken from MacPherson et al. (2016), wood density from Zanne et al. (2009).

Taxon	N	Category for random effect	Wood volume allometry	Wood density (kg m^{-3})
Acer campestre	29	Sapindaceae	Acer platanoides	520
Acer platanoides	575	Sapindaceae	Acer platanoides	520
Acer pseudoplatanus	1	Sapindaceae	Acer platanoides	520
Acer rubrum	79	Sapindaceae	Acer platanoides	520
Acer saccharum	13	Sapindaceae	Acer platanoides	520
Aesculus hippocastanum	3	Sapindaceae	Urban General Broadleaf	549
Carya ovata	1	Fagales	Urban General Broadleaf	549
Catalpa spp.	1	Other	Urban General Broadleaf	549
Celtis occidentalis	2	Other	Urban General Broadleaf	549
Crataegus spp.	1	Malus	Urban General Broadleaf	549
Fagus grandifolia	3	Fagales	Urban General Broadleaf	549
Fraxinus spp.	19	Fraxinus	Fraxinus pennsylvanica	530
Fraxinus pennsylvanica	168	Fraxinus	Fraxinus pennsylvanica	530
Ginkgo biloba	55	Ginkgo	Urban General Broadleaf	549
Gleditsia triacanthos	319	Fabaceae	Gleditsia triacanthos	600
Koelreuteria amurensis	1	Sapindaceae	Urban General Broadleaf	549
Koelreuteria paniculata	1	Sapindaceae	Urban General Broadleaf	549
Liquidambar spp.	1	Other	Liquidambar styraciflua	460
Liquidambar styraciflua	4	Other	Liquidambar styraciflua	460
Maackia amurensis	3	Fabaceae	Urban General Broadleaf	549
Magnolia spp.	1	Other	Magnolia grandiflora	460
Malus spp.	46	Malus	Urban General Broadleaf	549
Pinus resinosa	1	Other	Urban General Conifer	410
Platanus x acerifolia	124	Platanus	Platanus hybrida	500
Prunus spp.	60	Prunus	Urban General Broadleaf	549

Pyrus spp.	81	Pyrus	Urban General Broadleaf	549
Quercus macrocarpa	7	Fagales	Urban General Broadleaf	549
Quercus michauxii	1	Fagales	Urban General Broadleaf	549
Quercus palustris	23	Fagales	Urban General Broadleaf	549
Quercus rubra	62	Fagales	Urban General Broadleaf	549
Robinia pseudoacacia	1	Fabaceae	Urban General Broadleaf	549
Sophora japonica	1	Other	Urban General Broadleaf	549
Syringa reticulata	11	Other	Urban General Broadleaf	549
Tilia americana	16	Tilia	Tilia cordata	549
Tilia cordata	629	Tilia	Tilia cordata	420
Ulmus spp.	60	Ulmus	Urban General Broadleaf	549
Ulmus crassifolia	2	Ulmus	Urban General Broadleaf	549
Unknown spp.	1	Other	Urban General Broadleaf	549
Zelkova spp.	186	Zelkova	Zelkova serrata	520

Table 3.S5: Land cover configuration in the Boston study area.

Land Use/Cover	Study Area		Canopy		Edge Canopy		Impervious		Biomass	
	ha	% total	ha	% total	ha	% canopy	ha	% area	GgC	% total
Forest	1022	8	830	26	411	50	88	9	114	32
Developed	4734	38	477	15	462	97	3721	79	46	13
HD Residential	4815	39	1443	46	1416	98	2950	61	154	43
LD Residential	247	2	110	3	104	95	82	33	12	3
Other Veg.	1338	11	269	9	255	95	279	21	29	8
Water	258	2	15	0	14	91	7	3	2	0
Total	**12455**	**100**	**3144**	**100**	**2663**	**85**	**7138**	**57**	**357**	**100**

CHAPTER FOUR: Annual biogenic C exchange in an urban landscape

Abstract

Urban municipalities are setting greenhouse gas emissions reductions goals as aspects of climate policy, but current techniques for monitoring anthropogenic carbon dioxide (CO_2) emissions are complicated by biogenic C exchange processes that differ from rural counterparts and are at present poorly constrained in time and space. This study uses high-resolution data on land cover characteristics in the city of Boston, Massachusetts, to spatially model estimates of annual C fluxes from soil respiration and net vegetation photosynthesis. We find a median of approximately 38.4 GgC yr^{-1} in photosynthetic uptake of C by urban trees and turfgrass lawn areas, even in residential areas not obviously identifiable as "green spaces". However, high soil respiration C rate (median 38.0 GgC yr^{-1}), much of it from intensively managed landscaping, matched nearly the entire annual vegetation C sink, resulting in a non-significant median NEE of 0.6 GgC yr^{-1} city-wide. Urban forest fragments were estimated to remain a net C sink, but overall biogenic C uptake was predicted to offset only approximately 0.05% of the estimated 1290 GgC yr^{-1} fossil C directly emitted in the city. These results suggest that climate mitigation efforts for large cities like Boston need to focus on direct fossil C emissions reductions, as urban biogenic C uptake will not offer a natural solution to meaningfully offset emissions in the city. Our work highlights the need for additional research to better quantify the distribution and timing of these fluxes both to better understand urban biogeochemical cycling, and to improve our ability to resolve and track urban fossil C emissions.

1 Introduction

Cities produce an estimated 70% of global greenhouse gas emissions (UN, 2012), but also are increasingly leading the way in developing policies for managing the local causes and consequences of climate change (Broto and Bulkeley, 2013; Kennedy et al., 2009; Moran et al., 2018). Recognizing the role played by urban areas in global climate change, a number of cities in the U.S. and abroad have pledged to reach net carbon neutrality within the next few decades (Pichler et al., 2017). In parallel with these reduction goals, there is a need for effective and routine means of inventorying city-scale emissions and verifying reductions progress (Gurney et al., 2015). Research is underway in several U.S. cities to develop methods for monitoring and attributing fossil fuel CO_2 emissions in both time and space (Feng et al., 2016; McKain et al., 2012; Nathan et al., 2018; Sargent et al., 2018). A variety of approaches have been used to measure and attribute CO_2 flux in urban environments, including eddy covariance (Crawford et al., 2011; Crawford and Christen, 2015; Velasco et al., 2014) and bottom-up emissions inventorying (Gately and Hutyra, 2017; Gurney et al., 2009). A suite of top-down inverse atmospheric methods are also available based on ground-, aircraft-, and satellite-based measurements of localized gas concentrations over cities (Lauvaux et al., 2016; Mays et al., 2009; Newman et al., 2013; Sargent et al., 2018; Wu et al., 2018).

Monitoring urban fossil CO_2 emissions through atmospheric observations is complicated by the influence of heterogeneous and poorly constrained urban biogenic C fluxes to and from soil and vegetation (Hutyra et al., 2014). The effect of biogenic CO_2 fluxes on atmospheric CO_2 levels tends to be largest during the growing season, when plant photosynthesis and soil respiration are at their maximum (Sargent et al., 2018; Turnbull et al., 2015; Velasco and Roth, 2010). Complicating matters, biogenic C flux processes in urban areas appear to differ from their rural counterparts: Photosynthetic C uptake in urban trees is influenced by altered growing conditions such as increased temperature (Rizwan et al., 2008), changes in growing season length (Melaas et al., 2016), fertilizer, nutrient and pollutant deposition (Decina et al., 2018; Ollinger et al., 2002), and human interventions like tree planting and removal of trees and organic matter (Smith et al., 2019; Templer et al., 2015). Open-grown urban trees have been reported to have enhanced growth rates (Briber et al., 2015; Gregg et al., 2003; O'Brien et al., 2012; Takagi and Gyokusen, 2004), and mortality rates (Roman et al., 2014; Smith et al., 2019) compared to rural trees. Forest fragmentation edges also affects ecosystem carbon dynamics (Reinmann and Hutyra, 2017; Smith et al., 2019). The introduction of managed turfgrass lawns alters biogenic C cycling and belowground C storage compared to local native grasslands (Golubiewski, 2006). Studies of soil respiration in urban backyards suggest that highly managed soils can produce considerably greater C flux than unmanaged soils, in places comparable in magnitude to local fossil C fluxes (Decina et al., 2016).

Previous studies on urban biogenic C fluxes have made indirect estimates based on measures of land cover properties and function, by extrapolation of limited in-situ field sampling, or some combination of these methods. Hardiman et al. (2017) estimated hourly net biogenic C flux in the urbanized regions of Massachusetts using an approach derived from the Vegetation Photosynthesis and Respiration Model (VPRM) (Mahadevan et al., 2008). This approach employed an empirical model based on light-use efficiency and informed via time series of remotely sensed data on vegetation and temperature. Their work accounted for pavement and urban heat island effects on plant C uptake and respiration across the growing season (Wang et al., 2017). However, the coarse spatial resolution (500 m) of the UrbanVPRM approach did not permit adjustment for patch-scale productivity effects noted in local field studies (Reinmann and Hutyra, 2017). The UrbanVPRM was also parameterized based on C flux measurements taken in rural forests. Other studies have estimated components of urban biogenic C flux but not the net of uptake and emissions. Miller et al. (2018) modeled gross primary productivity (GPP) via scaling estimates of plant productivity based on light-use efficiency in a neighborhood of Minneapolis, Minnesota. Using a combination of satellite land cover data, tree sapflow, and eddy covariance measurement of lawn C flux, they were able to assess the spatial distribution of vegetation photosynthetic C uptake, but did not attempt to model soil respiration C efflux. Several additional studies have also estimated photosynthetic C uptake in urbanized regions taking a light-use efficiency approach based on satellite vegetation index data, but have generally applied rural-derived photosynthesis parameters and used land cover data with coarse (1 km) landscape- and continent-scale resolution (Imhoff et al., 2004; Zhao et al., 2016, 2012, 2007). A streamlined modeling process (UFORE), has been applied to estimate tree biomass and C uptake rate with measurable error in several North American and European cities (Nowak et al., 2013; Strohbach et al., 2012), but uses multiple simplifying assumptions for the sake of generalizability across urban areas. Other studies have paired remotely sensed land surface observations with simultaneous field sampling to inventory urban biomass C (Davies et al., 2011; Raciti et al., 2014; Rao et al., 2013a) and its dynamics with land conversion (Hutyra et al., 2011). However, no study we are aware of has attempted to estimate the distribution of both C uptake of vegetation and soil respiration C release in these landscapes using higher-resolution land cover character and emissions factors derived from field measurements in an urban context.

The presence of potentially large but poorly characterized biogenic C fluxes leaves significant uncertainty in estimating urban biogenic C flux across space and time. Uncertainty about the influence of biogenic C fluxes on urban atmospheric CO_2 concentrations injects uncertainty into efforts to accurately monitor urban fossil C fluxes. Our lack of granularity in the distribution of biogenic C fluxes also obscures important processes of energy and biogeochemical cycles operating in urban ecosystems. This study combines data on land cover characteristics in the city in Boston, Massachusetts, with urban-specific models of biogenic C flux processes to spatially resolve annual estimates of biogenic C fluxes and net ecosystem exchange (NEE) at a 30 m resolution. Finally, we evaluate biogenic C fluxes in their land use- and cover context, and compare them against satellite measures of vegetation cover and local estimates of fossil fuel C flux.

2 Methods

2.1 Data sources and processing

The study area was the city limits of Boston, Massachusetts, excluding sparsely inhabited offshore islands (see Trlica et al., 2020). Geospatial data at 1 m surface resolution for presence of impervious cover (MassGIS, 2005), tree biomass and canopy extent (Raciti et al., 2014) were combined to classify cells as either tree canopy, open impervious, open non-photosynthetic pervious ("barren", NDVI<0.25), or "turfgrass" (non-canopy, NDVI≥0.25). Cover data at 1 m were aggregated to 30 m cells coincident with the local Landsat grid. A map of land use/land cover classification (MassGIS, 2005) was also rendered to the same 30 m grid by maximum combined area (ESRI, 2014). Each 30 m grid cell was processed to determine the following cover characteristics: Simplified LULC class (Trlica et al., 2020), fraction impervious cover, fraction tree canopy (including fraction of sub-canopy area with pervious cover), fraction barren, fraction turfgrass, and total tree biomass (Table 4.S1). These metrics were combined with data from Landsat 5 TM and Landsat 7 ETM+ from the month of July in 2010–2012 (Dwyer et al., 2018), which were processed to produce a median EVI summer greenness estimate for each 30 m grid cell (Huete et al., 2002).

2.2 Carbon flux modeling

An estimate of annual net ecosystem exchange (NEE) for 30 m grid cells was calculated by combining estimates of soil respiration flux to the atmosphere (by convention denoted as positive sign). Estimated photosynthetic capture and biomass incorporation of C from the atmosphere (negative sign convention), included productivity in both woody (tree) and herbaceous (turfgrass) plants. Total annual net primary production (NPP) in herbaceous vegetation and trees was modeled to include to the extent possible all net biomass C increment in aboveground leaves and stems and belowground root growth. These estimates excluded intra-annual herbivore losses, and did not consider the longevity or depositional fate of the biomass once produced, much of which may be collected, moved, processed, and quickly re-oxidized (Falk, 1976; Templer et al., 2015). No life cycle of biomass C components was conducted in this study. Flux components were estimated for each pixel by sampling each flux factor at random from its respective sample distribution, applying a consistent set of factors across the map pixels for each model realization and repeating the process 1,000 times.

Soil respiration (R_S) rates were modeled using the results of Decina et al. (2016) according to pixel non-impervious area, soil management, and land use context. In each 30 m grid cell, total soil respiration was calculated as the sum of respiration from three types of non-impervious cover classed as either “turfgrass”, “landscaped” or “forest”. An empirically derived soil flux factor of 0.840 (SD 0.002), 1.239 (SD 0.002), and 0.472 (SD 0.001) kgC m^{-2} yr^{-1}, respectively, was applied to each cover class. Season-total mean soil flux factors and uncertainty were estimated by fitting a cubic spline GAM to the measured time series of R_S in each land cover context (from Decina et al., 2016), then randomly resampling from the predicted GAM error distribution in each daily bin. Soil flux factors were applied to pixel pervious area according to LULC class: In Forest classed pixels, the R_s in non-impervious cover was modeled entirely using the forest soil flux factor. In residential pixel classes (HD Resid. and LD Resid.), the turfgrass soil flux factor was applied to the fractional turfgrass area. The landscaped soil flux factor was applied to the fractional barren area. In the sub-canopy pervious area 50% of the area was modeled with the turfgrass soil flux factor the other 50% with the landscaped soil flux factor. This application scheme for soil flux factors was similar to the calculations performed for residential areas in Decina et al. (2016). This scheme assumed non-photosynthetic pervious area to be better described as primarily under active landscaping management rather than left as bare soil, while also assuming an even lawn/landscaped division for un-observed pervious area beneath tree canopy. For Developed and Other Vegetated classed pixels, the fractional barren area (including areas such as cleared industrial land and sand beaches) was applied an emissions factor of 0 kgC m^{-2} yr^{-1}. Emissions factors for tufgrass- and sub-canopy pervious areas were applied similarly to residential classes. In all cases, impervious cover and open water was treated as having R_s flux of 0 kgC m^{-2} yr^{-1}.

Turfgrass net productivity was estimated by applying an annual C uptake factor to fractional lawn area. This factor was centered at a mean of 0.903 kgC m^{-2} yr^{-1} (SD 0.161), representing a conservative estimate of C uptake based reported GPP from eddy covariance monitoring of nominally managed turfgrass in Minnesota (Hiller et al., 2011; Miller et al., 2018). We further assumed a 62% ratio of NPP:GPP in turfgrass systems (Falk, 1980), and active growing season length of 240 days for the region (Peters and McFadden, 2012). Combined with the mean turfgrass R_s factor, this approach results in a central net estimate of C drawdown on the order of 0.1 kgC m^{-2} yr^{-1}, comparable to annual NEE measured in other studies of turfgrass C balance and productivity (Hiller et al., 2011; Peters and McFadden, 2012; see Supplemental for more complete discussion). Short-lived root growth and aboveground biomass clipping and removal were included in the total NPP estimate, which may represent a substantial fraction of annual production in turfgrass systems (Falk, 1980; Kaye et al., 2005). Changes in long-term total soil organic carbon storage were not included in total C drawdown in turfgrass since these fluxes are usually small and variable on an annual scale (Qian and Follett, 2012), and to remain consistent with the tree C fluxes accounted for in this study.

Annual NPP for trees was calculated as separate fluxes for C uptake via aboveground woody biomass increment, belowground coarse root increment, and annual (deciduous) foliar biomass production. Estimating production of fixed C via aboveground woody biomass increment followed Trlica et al. (2020) using estimated C drawdown to woody biomass growth based on local tree growth measurements scaled spatially with maps of canopy and biomass in the Boston area. For the component of NPP allocated to aboveground woody biomass in open- and street grown trees, allometric equations for wood volume (m^3) increment based on DBH change and were paired when possible with species-specific factors for wood density (kg m^{-3}) to estimate aboveground incremental biomass gain (Table 4.S2; McPherson et al., 2016). To estimate the equivalent NPP C flux to aboveground woody biomass for trees in Forest classed pixels, rural-derived species-specific allometric equations (Chojnacky et al., 2014; Jenkins et al., 2003) for aboveground biomass were bootstrapped 1,000 times to estimate plot-basis C uptake rate (kgC m^{-2}-canopy yr^{-1}) from their constituent stem biomass increments (see Trlica et al., 2020). The component of annual NPP C allocated to leaf production was estimated based on the total dry biomass of leaves per stem, estimated via allometric relationships with tree DBH, acting as a proxy for total leaf litter production (see Supplemental). For open- and street grown trees, species- and region-specific allometric equations for urban trees were used when available to predict the total foliar area (m^2), then species-specific factors for foliar dry weight (kg m^{-2}) were applied to estimate total annual foliar biomass production (Table 4.S2). For trees in Forest classed pixels trees, we used species-specific allometric equations for rural trees (Jenkins et al., 2003) to directly estimate foliar biomass via fraction of aboveground biomass. Foliar biomass C uptake on a plot-basis was predicted iteratively simultaneous with aboveground woody biomass in Forest-grown trees. Annual NPP allocated to coarse root growth was estimated as the annual increment in belowground coarse root biomass, predicted via allometry to determine the ratio of belowground coarse root biomass to aboveground biomass. For open-grown and street trees this ratio was set to a fixed factor of 0.28 times the aboveground biomass (MacPherson et al., 2016), while for urban forest-grown trees this ratio was predicted based on species-specific allometries for rural trees (Jenkins et al., 2003).

2.3 Statistical analysis

All processing and analyses were performed in the R software package (R Core Team, 2017) with the libraries *raster* (Hijmans, 2017) and *data.table* (Dowle and Srinivasan, 2017). To identify trends we fit Generalized Additive Models (GAM) based on cubic regression splines using the *mgcv* (Wood, 2011) library. We examined the relationship of NEE to corresponding metrics of Landsat multi-year summertime composite EVI and to LULC via GAM trend fits to examine the spatial correlates for biogenic C flux across the city. Unless noted, summary figures are reported as median values with the central 95% of estimates.

3 Results

Net biogenic ecosystem exchange (NEE) of C for the city of Boston was estimated as a small net sink -0.6 (-13.9 – 7.3) GgC yr^{-1} (Table 4.S3). The range of median per-pixel estimates for NEE was -10.6–12.2 MgC ha^{-1} yr^{-1}, with a median of 0.0 (-4.1–3.3)

MgC ha^{-1} yr^{-1} (Figure 4.1). Residential LULC classes were estimated to be net biogenic C sources of 1.49 (0.32 – 2.31) MgC ha^{-1} yr^{-1}, while forest fragments and large parks tended to act as net biogenic C sinks of -2.68 (-11.17 – 0.74) MgC ha^{-1} yr^{-1} (Table 4.1). Normalized across the city, we estimated a very low non-significant annual net sink of -0.05 (-1.13 – 0.59) MgC ha^{-1} yr^{-1}. Differences in NEE between LULC classes were related to broad differences in underlying distributions of available pervious soil, turfgrass area, and tree biomass (Table 4.S1).

The most potent net sink was estimated in Forest-classed land, with smaller contributions from Other Vegetated land and possibly Developed land. Forest and Other Vegetated cover types made up a relatively small fraction of the total urban area, but their larger proportion of tree and turfgrass cover resulted in a relatively large net sink city-wide. Somewhat surprisingly, Developed land cover was also predicted to be a small but non-significant total net C sink. The net sink in Developed land may have been due to a C sink effect operating in a minority of pixels in which some presence of net C uptake (presumably primarily tree NPP), paired with low soil efflux rate due to a high degree of impervious cover. This effect may also be related to the modeling assumption of 0 kgC m^{-2} yr^{-1} R_S efflux from non-vegetated ("barren") soil in Developed areas. The relatively large area of Developed land cover in the city of Boston thus permitted this small minority of net-C-sink pixels to sum to a modest potential sink overall. In contrast, the two extensive Residential land cover classes were estimated as relatively strong net biogenic C sources, hosting NEE fluxes that offset nearly the net annual C sink generated in the other classes.

The net C sinks estimated in Forest LULC was due primarily to high tree net C uptake occurring within large areas of unmanaged soil with relatively low soil C efflux rates. Metrics of modeled tree NPP components in densely forested pixels showed general agreement with field measurements made in undisturbed forest (see Supplemental). Developed areas were predicted to be relatively biologically inert, with comparatively low component C fluxes and a non-significant net C sink, due to low vegetation abundance and high degree of impervious cover. In contrast, while the median estimate of NEE for Other Vegetated areas was predicted as a small non-significant negative C flux, in this LULC relatively large C uptake (primarily turfgrass NPP) tended to be balanced by relatively large soil C fluxes in managed lawn and landscaped soils with moderate- to high soil respiration efflux rates. The unexpectedly strong net C release in the HD- and LD Residential classes was mainly a product of moderate C uptake (primarily tree NPP, but including some turfgrass NPP) being paired with even more intense soil respiration C efflux from the large area of available highly-managed landscaped and lawn soils.

Forest-class areas showed relatively strong C uptake due to correspondingly high levels of tree NPP, but Residential-class neighborhoods also showed moderate tree NPP C uptake due to elevated open-grown tree productivity paired with moderate biomass density in these areas (Trlica et al., 2020). Turfgrass NPP C uptake tended to be stronger in LD Residential and Other Vegetation categories, classes that also contained a greater fraction of open lawn areas (Table 4.S1). Soil respiration flux strength was negligible in Developed LULC, moderate in Forest, and relatively high in Other Vegetated, HD- and LD Residential. This separation was due to the low availability of pervious soil in Developed areas, compared to Forest LULC with little impervious cover but with relatively low soil respiration rate. In HD Residential areas, higher soil respiration factors per m^2 (landscaped and lawn) tended to potentially be mitigated by the lower availability of open pervious soil, while these constraints were reduced in LD Residential and Other Vegetated LULC, resulting in their relatively high soil respiration flux.

Variability in the estimates of city-wide NEE was due mainly to uncertainty in the underlying models used for estimating component C fluxes. In contrast, variability in pixel-median estimates of NEE was wider and driven mainly by underlying land cover heterogeneity at the sub-pixel scale (Figure 4.1). Median estimated NEE at the pixel level showed a high degree of variability across short spatial scales, but also displayed some coherent patches of net C sinks (e.g. large parks), net C sources (e.g. LD-Residential dominated neighborhoods in southeast Boston), and large areas of net 0 C exchange (e.g. downtown financial district). Developed pixels tended towards low median NEE, with 77% operating as modest net C sinks (no greater than -1.0 MgC ha^{-1} yr^{-1}) (Figure 4.2). Other Vegetated pixels showed a range of NEE extending into both relatively large sources and sinks of C (-8.6 to 5.4 MgC ha^{-1} yr^{-1}), while 62% were modest sinks due to the balancing effect of moderate soil respiration sources paired with turfgrass NPP-driven sinks. In HD- and LD-Residential 67% pixels were net C sources, with 1% of pixels acting as relatively potent biogenic C sources (at least 5 MgC ha^{-1} yr^{-1}). Even Forest pixels, where the 92% of pixels were net C sinks, showed a range extending from large net sinks to net sources (-10.1 to 5.5 MgC ha^{-1} yr^{-1}) depending on underlying cover and vegetation.

Biogenic C fluxes showed ambiguous relationships to traditional remotely sensed measures of vegetation at 30 m. Pixel median NPP (including tree and turfgrass NPP) was positively correlated with median summertime Landsat EVI. For each class GAM explained 5.6%, 54.1%, 41.1%, 35.5%, and 35.2% for Forest, Developed, HD Residential, LD Residential, and Other Vegetated LULC of deviance, respectively (not shown). Pixel median NEE estimates were not well predicted by EVI, though different land cover classes did cluster along different ranges of EVI and median NEE (Figure 4.3). GAM fits to the relationship explained a maximum of 9.1% of deviance in NEE. This lack of correlation between NEE and EVI is likely due in part to the wide range of variability in urban vegetation productivity and open sub-canopy pervious surface present at any given level of EVI. This lack of correlation is also likely a product of the lack of a clear radiometric signal associated with fine-scale management-related influences on R_S processes.

4 Discussion

Total scope 1 fossil fuel C flux was recently estimated at approximately 1290 GgC yr^{-1} for the Boston study domain (Gately and Hutyra, 2017). We estimate that NEE in the same area would only offset a maximum of approximately 1.1% of fossil C emissions annually (assuming 95th percentile of estimated NEE), with a median estimate of approximately 0.05%. However, though city-wide NEE flux on an annual basis may be much smaller than fossil fuel C emissions, on a finer spatial and temporal scale the component biogenic fluxes may be comparable in magnitude to co-located fossil fuel C flux contributions to the local atmosphere (Hardiman et al., 2017; Sargent et al., 2018). In this study, each 30 m pixel incorporated a range of constituent NEE C fluxes. The fluxes vary temporally versus one another depending on the timing of seasonal conditions like temperature, moisture, light availability, and plant phenology (Kozlowski, 1992; Mahadevan et al., 2008; Melaas et al., 2016). Soil respiration is influenced by temperature and moisture changes, while in trees the timing of C-exchanging processes like leaf emergence, photosynthesis, and woody biomass production respond to seasonal cues in temperature, moisture, and light availability, and can also vary temporarily relative to one another (Curtis et al., 2005; Gough et al., 2008; Klein and Hoch, 2015; Paembonan et al., 1992). Our results therefore imply geographically concentrated area like Boston could act as spatially heterogenous sources or sinks of atmospheric C at varying periods of the year. These spatio-temporally bounded fluxes create very large uncertainties in summertime atmospheric inversion (Sargent et al., 2018), even if annual integrated NEE flux is locally low. Our results also offer a counterpoint to that reported in Decina et al., (2016), who showed that across a transect of urbanization intensity in the Boston region, soil respiration flux could reach as high as co-located fossil C fluxes in moderate-density areas. Our results imply that R_s C fluxes in these same types of residential settings may also be as large or larger than local vegetation C drawdown.

Components of urban biogenic C flux have been estimated or used in other studies, but to our knowledge no other study has estimated complete urban biogenic C fluxes. Across 28 North American cities, Nowak et al. (2013) using the UFORE forest productivity model estimated tree C uptake of roughly <0.1–0.9 MgC ha^{-1} yr^{-1} to long-lived biomass (adjusting for city-wide tree canopy cover), with an estimate of approximately 0.5 MgC ha^{-1} yr^{-1} for Boston. Similarly, in estimating changes in the strength of the C sink due to forest NPP in Massachusetts, Reinmann et al. (2016) assumed a C uptake rate of up to approximately 0.5 MgC ha^{-1} yr^{-1} for core city areas with canopy cover of 25%, based on growth trends measured in local FIA plots. Our median estimate was considerably higher at approximately 2.1 MgC ha^{-1} yr^{-1}, but our study included long-lived aboveground biomass and estimates for foliage and coarse root growth. The fraction of per-pixel flux of C to production of foliar biomass was estimated at median of 41% (20–62%) of total net tree photosynthetic C uptake. We also modeled C uptake based on higher local measurements of growth in open- and edge-grown trees rather than using models of growth based on rural forests. Churkina (2016) used an estimated NEE net C drawdown of -3.19 to -3.35 MgC ha^{-1} yr^{-1} as a component of their global modeling study on C flux in urban areas, but these factors were based on stereotyped values of urban vegetation and soil fraction and used GPP and ecosystem respiration estimates derived from measurements of rural humid deciduous forests. Pataki et al. (2011) made a simplified prediction that in a city like Los Angeles with productive but limited vegetation cover the magnitude of C uptake compared to local fossil fuel C emissions would be close to negligible. Our estimates accord with their prediction, but add critical detail and nuance. The inclusion of R_S C efflux shows that true net biogenic C sequestration is likely considerably smaller than vegetation NPP, but we find very large spatial variation across the city that likely changes depending on time of day and season.

Crawford and Christen (2015) estimated the vegetation and soil C flux components of C flux measured via eddy covariance over a residential neighborhood in Vancouver, British Columbia. Using a light-use efficiency approach, they estimated approximately 4.6

MgC ha^{-1} yr^{-1} gross C assimilation via photosynthesis in trees and turfgrass, and 3.5 MgC ha^{-1} yr^{-1} in ecosystem respiration (implying NEE of 1.1 MgC ha^{-1} yr^{-1}). Based on these observations, Kellett et al. (2013) similarly estimated NEE of 1.6 MgC MgC ha^{-1} yr^{-1} in this area, of which up to about 50% were expected to be exported as green waste. Our estimated vegetation NPP of approximately 3 MgC ha^{-1} yr^{-1} across the city imply gross C assimilation somewhat higher than reported in Vancouver, assuming a reasonable fraction of C loss as vegetation respiration (DeLucia et al., 2007; Falk, 1980). However, our estimated R_s rates were likely also higher than the soil component of ecosystem respiration estimated in Crawford and Christen (2015), which were based in part on soil respiration flux measurements from local lawn areas. Soil management preferences may differ between Vancouver and Boston, and soil temperature is likely considerably lower in Boston. It is also possible that flux partitioning based on soil respiration rates measured in Vancouver lawns did not capture higher respiration rates in landscaped areas, as was seen in Decina et al. (2016), and as was possibly implied by high nighttime biogenic C fluxes measured in Crawford and Cristen (2015).

Hardiman et al., (2017) estimated biogenic C fluxes using the satellite-driven UrbanVPRM model for the greater Boston area to be -10.3 MgC ha^{-1} yr^{-1} in gross C uptake and 8.9 MgC ha^{-1} yr^{-1} in ecosystem respiration (implying NEE of approximately -1.4 MgC ha^{-1} yr^{-1}). In contrast, our study did not predict a significant NEE C sink. This difference may be related to difference in study domain, which in Hardiman et al. (2017) included considerable sub- and ex-urban area outside of Boston’s city limits presumably with greater vegetation and soil cover. It is not straightforward to compare our estimate of R_s to their ecosystem respiration totals, however we note their modeled soil respiration was not based on local flux measurements and did not attempt to model respiration sensitivity to soil management context. In addition, NPP C uptake in Hardiman et al., (2017) was modeled based on New England rural forests, and did not capture differential turfgrass NPP or the effect of urban tree growth rates; all green vegetation was presumed to behave as trees. They estimated 75% less tree biomass in the most urbanized sub-region of their study (including Boston), but estimated gross C uptake was only reduced by 32%. It is unclear to what extent the vegetation C assimilation rates predicted by Hardiman et al. (2017) via satellite EVI were related to a previously noted enhancement of EVI in urbanized areas (Jia et al., 2018), or to the contribution of turfgrass to the overall EVI signal.

In the urban ecosystem of this study, 30 m pixel-sized areas showed wide variability in NPP related to the presence of different vegetation types and biomass densities at the sub-30 m scale. Variable NPP rates were further combined with a high degree of spatial heterogeneity of R_s, the controls of which (such as impervious cover distribution or soil management tendencies) may not have an obvious radiometric signature. These sub-pixels effects on biogenic C flux processes are not likely readily captured in simple satellite vegetation or regional temperature (Hardiman et al., 2017). The lack of clear correlation between satellite remote-sensing based measures of vegetation function, broad soil respiration controlling factors like temperature, and pixel median NEE estimates urges caution in applying these models in the unique, fragmented, and heterogeneous growing environment of urban areas.

Terrestrial ecosystems in long-timescale equilibrium should maintain an approximately steady stock of carbon in soil and biomass, with NPP and R_s in balance after sufficient time post-disturbance (Odum, 1969). The considerable positive and negative mismatches we estimate in parts of the urban landscape imply that this equilibrium is not maintained in the urban biogenic C cycle. In Forest areas, a predicted net C uptake may imply that these comparatively "young" systems are still in a phase of C acquisition. Other areas, such as Developed areas, support little open soil or vegetation, and appear to have an impoverished C cycle in general. However, in residential areas, the effect of human activities, including the import or export of nutrient or additional organic C (Templer et al., 2015), may help fuel ongoing soil C flux in excess of local vegetation C fixation (Decina et al., 2016).

Studies of ecosystem C dynamics in rural forests offer instructive contrasts to our results. Gough et al. (2008) reported tree NPP of approximately 6-7 MgC ha^{-1} yr^{-1} in a mixed deciduous forest in Michigan, comparable to our Forest NPP estimates, though the Michigan values include a 41% component of fine root turnover (not estimated in this study). Soil respiration averaged approximately 5 MgC ha^{-1} yr^{-1}, comparable to our Forest estimates but somewhat lower than areas like LD Residential and Other Vegetated containing a greater fraction of managed soils. Reported NEE in their study was approximately -1.5 MgC ha^{-1} yr^{-1}. The contrast with our results may reflect a combination of lower soil respiration C efflux in the Michigan study, generally lower biomass and NPP per ha in our study domain, and the exclusion of C allocation to fine root turnover in our study. Showing similar findings, a study of a mixed deciduous forest at the Bartlett experimental forest in New Hampshire reported approximately 6.2 MgC ha^{-1} yr^{-1} in NPP (with 44% as belowground NPP, including fine root turnover), heterotrophic soil respiration (above and belowground) of approximately 5 MgC ha^{-1} yr^{-1}, and NEE of 1.2–1.3 MgC ha^{-1} yr^{-1} (Ouimette et al., 2018). Reports from the nearby Hubbard Brook experimental forest in New Hampshire reported similar findings, with estimated aboveground NPP of approximately 4 MgC ha^{-1} yr^{-1}, belowground NPP of 1.8 MgC ha^{-1} yr^{-1}, and soil respiration of approximately 4.7 (heterotrophic component) to 11.3 (roots + heterotrophs) MgC ha^{-1} yr^{-1} (Fahey et al., 2005). In contrast to other rural forests under study, the NEE for this site was estimated as essentially 0 MgC ha^{-1} yr^{-1}, possibly due to a variety of site-specific factors. In the mixed deciduous forest of the Harvard Forest located 100 km from Boston, NEE measured by eddy covariance ranged from -1.0 to -4.7 MgC ha^{-1} yr^{-1} (mean -2.5 MgC ha^{-1} yr^{-1}), aboveground woody increment (excluding mortalities) was 1.0 to 2.5 MgC ha^{-1} yr^{-1}, and total ecosystem respiration (soil + aboveground autotrophic tissues) ranged from 10–13 MgC ha^{-1} yr^{-1} (Urbanski et al., 2007). Rural forests show somewhat lower soil respiration and higher NPP, tending towards a significant NEE C sink of several MgC ha^{-1} yr^{-1}. Though most of the Boston study area supports less dense tree biomass than nearby rural forests, it is also possible that our tree NPP values were underestimated as a result omitting fine root turnover fluxes. Our soil respiration estimates in some LULC classes may be higher as a result of enhanced heterotrophic C efflux with greater nutrient and organic matter input in urban soils. The net result of these broad differences likely explains the lack of a clear NEE C drawdown in our model of Boston's biogenic C fluxes. It remains unclear if the addition of fine root NPP to our model would meaningfully change our estimated city-wide NEE C sink.

At present, more is understood about biological C exchange processes in surrounding rural forests than in urbanized areas (Hutyra et al., 2014). However, in constructing a larger urban biogenic C budget, we acknowledge the logical difficulties accounting for C fluxes due to organic materials of possibly unknown outside origin (for instance, imported mulch and compost), or from biomass produced in the city but them moved elsewhere (for instance, exported leaf litter and woody debris [Templer et al., 2015]). In our approach, we have attempted only to spatially model the average annual C fluxes across this dynamic landscape. Our results imply that the city is not likely to be taking up C on net through photosynthesis, but we cannot ascertain whether or not total ecosystem C stocks are changing as a result of direct organic matter importation or broad-scale changes in soil carbon stocks. A comparison of scope 1 fossil C emissions across the same area with our results implies that net biological C uptake is unlikely to significantly offset anthropogenic emissions, unless soil respiration processes are left entirely out of the accounting. Even under such an erroneous assumption, local long-term tree biomass C uptake is not likely to offset more than roughly 1% of annual emissions (Trlica et al., 2020).

In the approximately 60% of the city of Boston outside of densely developed non-residential areas, biogenic C fluxes to and from the atmosphere from these areas could complicate the interpretation of locally measured atmospheric CO_2 mixing ratios used for surface network- (Sargent et al., 2018) or satellite-based atmospheric inversions (Wu et al., 2018). Uncertainties in urban biogenic C fluxes could be reduced with improved local data such as regular aerial surveys of canopy extent and height via leaf-on LiDAR and multi-spectral photography. Further high resolution (<10 m) regular monitoring of impervious surface extent and land development (or abandonment) would allow researchers to better discern the fine-scale processes that drive urban-specific biogenic C fluxes (Trlica et al, 2020; Decina et al., 2016). Regular measurements of growth and mortality in city-owned street trees would provide an independent source of information on C uptake in the urban forest. We also note a paucity of studies on the productivity and C dynamics of urban turfgrass lawns, particularly in the New England region. Additional information on land management practices or economic data on organic waste management could also enhance our ability to estimate lateral movements of biogenic C across the urban landscape and estimate C efflux from managed soils (Decina et al., 2016; Short Gianotti et al., 2016; Templer et al., 2015). More intensive study of the underlying processes of plant productivity and ecosystem respiration, particularly at the field scale through vegetation and soil monitoring, would also improve our understanding and capacity to estimate these biogenic C fluxes in time and space.

Cities can potentially manage their urban ecosystems to increase C uptake, for instance by maintaining and enhancing tree cover in street plantings and greenspaces, increasing tree cover in non-forested open space such as golf courses and playing fields to greater tree cover, and incentivizing landowner tree preservation (Trlica et al., 2020). However, reducing soil respiration C efflux is less straightforward, as decisions on soil management and reduction of organic inputs is implemented by individual actors and households. Further, reductions in mulch application may raise environmental impacts related to irrigation requirements or seedling establishment success (Chalker-Scott, 2007) Strategies to offset fossil C emissions via net biogenic C uptake are unlikely to be very effective, given the high rates of R_S in our study area, and the necessarily physical space requirements for trees in dense urban neighborhoods. We note, however, that the potential public benefits of urban ecosystem services beside C sequestration are manifold, including moderating excessive temperatures, improving air quality, increasing soil water infiltration, reducing noise, supporting biodiversity, and providing social and psychological benefits (Gómez-Baggethun and Barton, 2013; Lovell and Taylor, 2013; Roy et al., 2012). Advancement of the goals of enhanced urban "green infrastructure" will require improvement in our understanding of ecosystem functions in their specific contexts and locations, and the ecosystem services and disservices they produce (Escobedo et al., 2011; Pataki et al., 2011). A better understanding of these processes will also support of the goal of accurately monitoring and reducing fossil C emissions, where the bulk of public effort must be focused.

Acknowledgments

The author wishes to acknowledge the USGS for use of the Landsat archive, Dr. Steve Raciti for use of his biomass and canopy map for the city of Boston and advice on details of its preparation; Dr. Steve Decina and co-authors for the use of their local soil respiration flux data; Dr. Andy Reinmann for the use of his field DBH measurements; David Miller for helpful commentary on his turf grass findings; and Ian Smith for the use of his data and findings on street tree growth. The author also wishes to acknowledge the members of his dissertation committee — Mark Friedl, Lucy Hutyra, Nathan Philips, Pamela Templer, and the late Anthony Janetos — for helpful input on strategy and approach during construction of this C budget. The author also wishes to acknowledge Dr. Valerie Pasquarella for helpful input during the writing and editing process.

Figure 4.1: Median pixel estimate for NEE in city of Boston, MgC ha^{-1} yr^{-1}. Negative values indicate net C uptake, positive values indicate net C emissions. Pixel size is 30 m.

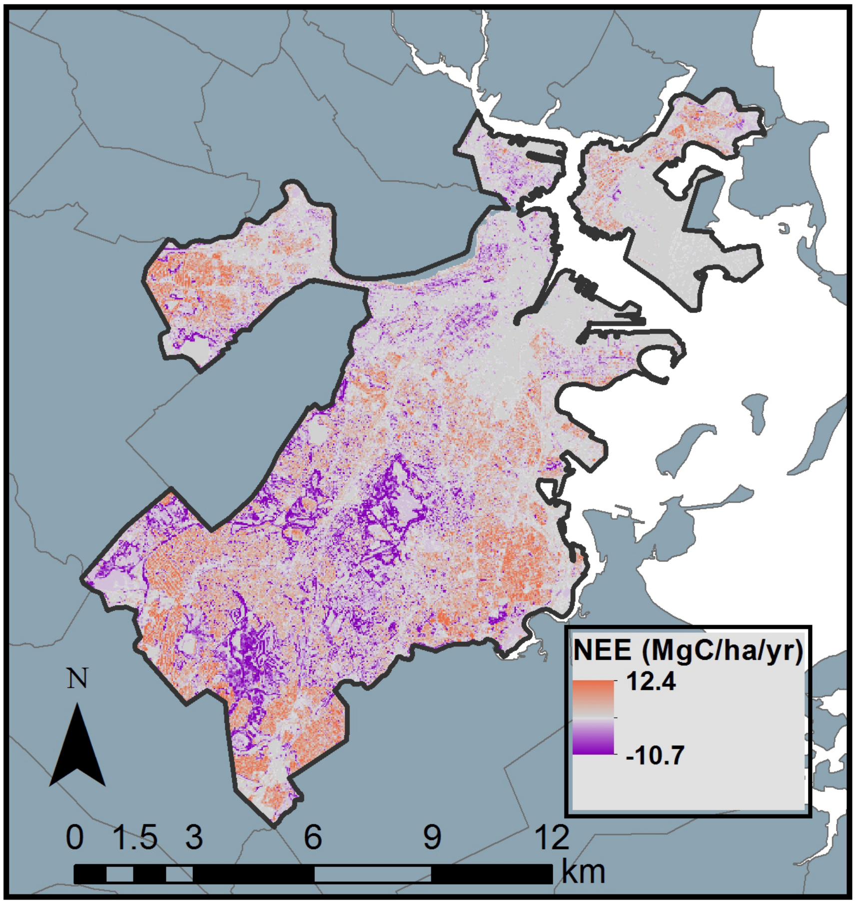

Figure 4.2: Distribution of per-pixel median estimated NEE (MgC ha^{-1} yr^{-1}). Inset shows relative areas of different LULC classes, and boxplot widths are also proportional to areas (Water values not shown).

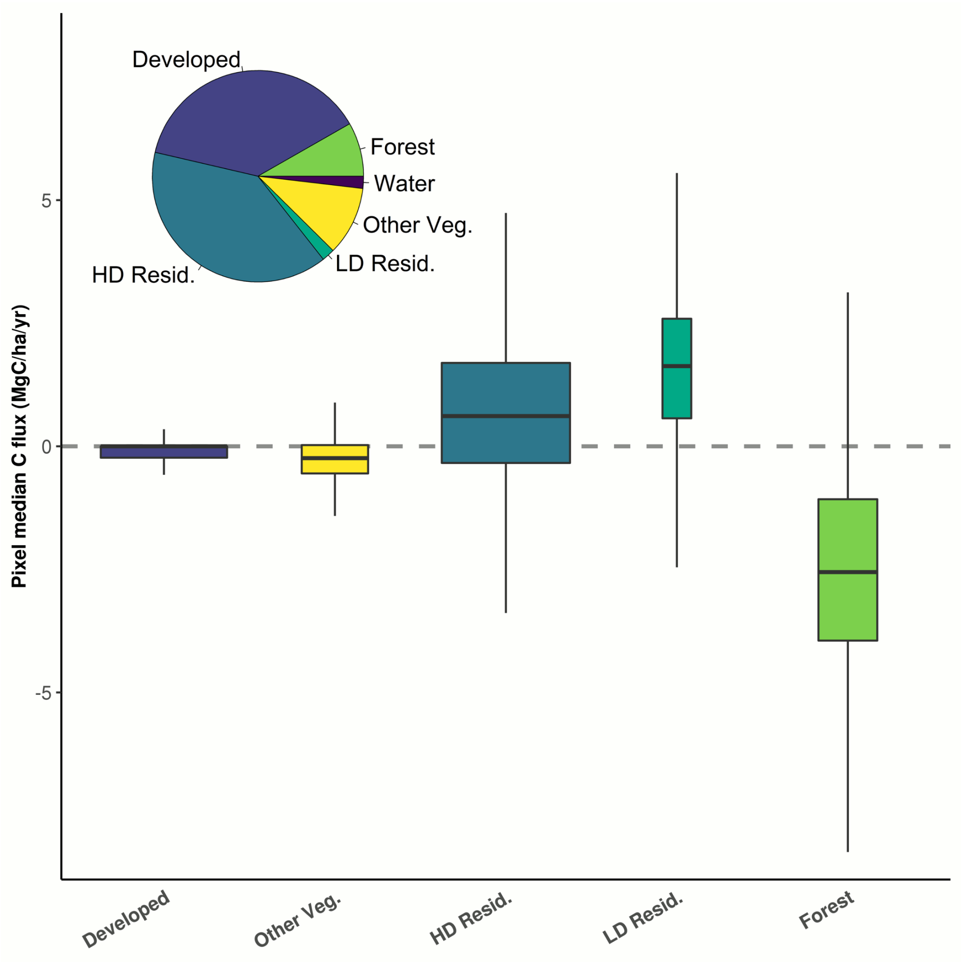

Figure 4.3: Median pixel Landsat July EVI (2010–2012) versus median pixel NEE estimate (MgC ha^{-1} yr^{-1}), by LULC. Color shading indicates concentration of pixel frequency. GAM prediction line shown in red. Bottom right shows histogram of pixel median NEE estimates for all LULC classes.

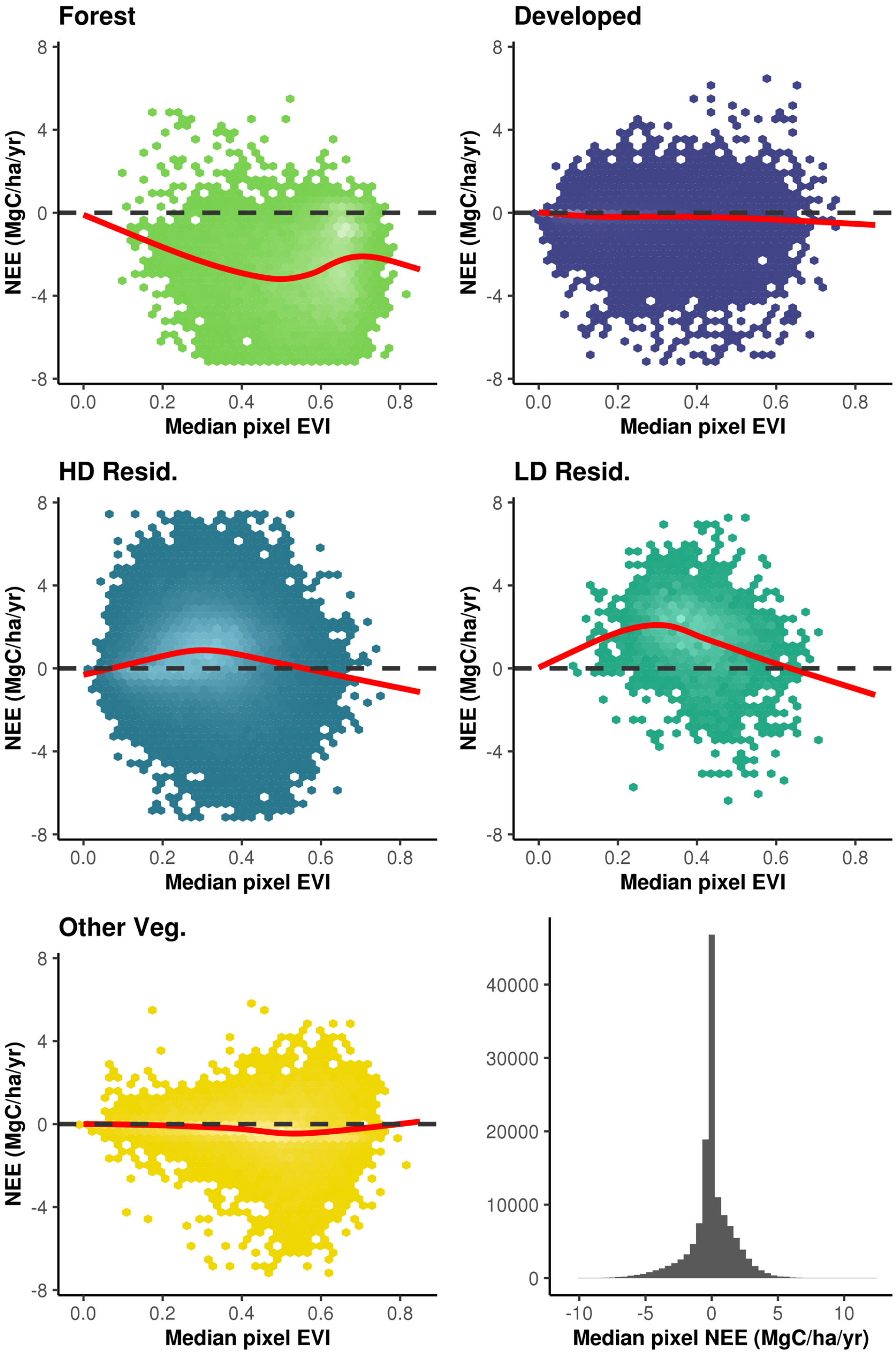

Table 4.1: Estimated map-wide biogenic C flux strength by LULC in Boston (median and central 95%). All figures in MgC ha^{-1} yr^{-1}, representing the sum of C flux for pixels of a given LULC divided by LULC area, summarized across model realizations. Negative values indicate flux of C from atmosphere, positive values represent flux of C to atmosphere.

LULC	**Tree NPP**	**Turfgrass NPP**	**Soil Respiration**	**NEE**
Forest	-6.09 (-2.62– -14.82)	-1.13 (-0.74 – -1.53)	4.54 (4.52 – 4.57)	-2.68 (-11.17 – 0.74)
Developed	-0.84 (-0.74 – -1.00)	-0.49 (-0.32 – -0.66)	1.17 (1.17 – 1.18)	-0.16 (-0.37 – 0.04)
HD Resid.	-2.54 (-2.15 – -3.10)	-0.81 (-0.53 – -1.10)	3.97 (3.96 – 3.99)	0.64 (0.01 – 1.09)
LD Resid.	-3.79 (-3.04 – -4.89)	-1.49 (-0.98 – -2.02)	6.76 (6.74 – 6.78)	1.49 (0.32 – 2.31)
Other Veg.	-1.79 (-1.40 – -2.37)	-3.81 (-2.50 – -5.17)	5.31 (5.29 – 5.33)	-0.32 (-1.71 – 1.10)
Total	**-2.09** **(-1.57 – -3.12)**	**-1.03** **(-0.68 – -1.40)**	**3.09** **(3.08 – 3.10)**	**-0.05** **(-1.13 – 0.59)**

Supplemental Information for *Annual biogenic C exchange in an urban landscape*

4.S1 Carbon uptake and allocation in trees

We compared metrics of biogenic C dynamics modeled in this study to in pixels with near-complete (85% or greater) canopy coverage to comparable annual measurements from 2000–2014 taken at the Harvard Forest (HF) Environmental Measurement Station (EMS) (Table 4.S4). These highly canopied pixels tended to have somewhat higher median biomass density (139 MgC ha^{-1} compared to 100–127 MgC ha^{-1} at HF), and higher estimated annual aboveground woody biomass increment (AGWI; 2.4 MgC ha^{-1} yr^{-1} versus 1.4–1.8 MgC ha^{-1} yr^{-1} at HF). This higher predicted AGWI in Boston is likely the result of modeling based on faster measured rates of growth in Boston's urban trees compared to nearby rural trees (Trlica et al, 2020). Similarly, aboveground NPP (the sum of AGWI and annual foliar biomass production, measured as litterfall at HF) was also higher in the full-canopy pixels than HF. The ratio of AGWI to ANPP (the sum of AGWI and foliar biomass production, which was measured as litterfall in HF) was somewhat lower in the modeled Boston pixel than at HF (0.39 AGWI:ANPP, versus 0.44–0.52 in HF), suggesting that the method of predicting annual foliar biomass production in mostly forested urban pixels based on allometric equations for foliar biomass resulted in somewhat higher estimates of ANPP overall, though the empirical and modeled ratios are comparable. In contrast, similar comparison of HF measurements to Boston pixels with more scattered tree canopy and modeled using a different approach and urban-specific allometric equations ("Street tree" pixels) showed lower biomass density, NPP, and AGWI, but comparable AGWI:ANPP ratios. This Street tree modeling approach was applied to the majority of pixels in the study area, and these results more broadly indicate that allometric predictions were generally in line with tree C allocations observed in the non-urban HF context.

Trees fix carbon during photosynthesis and allocate these compounds to support growth or maintenance respiration in different tissues and at potentially different times (Amthor and Baldocchi, 2001; Gough et al., 2008), storing some as non-structural carbohydrates (NSC) (Kozlowski, 1992). These NSCs may be built up in the prior year and stored to fuel spring leaf growth, temporarily exceeding immediate new C fixation, though NSC reserves to do not appear to fluctuate greatly over the growing season, implying that respiration overshoot is temporary in the early growing season (Körner, 2003). At the end of the growing season, up to 16–26% of foliar C may be reabsorbed prior to leaf fall (Fahey et al., 2005), presumably to be stored as NSC reserves. On longer time scales, tree respiration, including respiration to fuel growth, is limited by gross carbon uptake (GPP) (Arneth et al., 1998; DeLucia et al., 2007). Aside from some transient early-season pulses and other temporary asymmetries between C assimilation and growth, release or export, growth-related respiration also appears to be linked relatively tightly to current NPP (Klein and Hoch, 2015), while maintenance respiration remains relatively constant though responsive to temperature, implying that reasonably constant fraction of C uptake is partitioned to new tissue growth during the growing season (Paembonan et al., 1992; Piao et al., 2010).

The fraction of leaf biomass to total tree mass for woody angiosperms is typically well below 0.3, and below 0.03 for full grown trees (Poorter et al., 2012), implying that estimates of annual biomass increment determined from allometric functions relating aboveground biomass to DBH will be dominated by woody biomass increment. However, allocation of a single year's C uptake to foliage, flowers, and seeds has been measured in the region of 60% of NPP allocation to woody biomass growth in the Bartlett experimental forest in New Hampshire (Ouimette et al., 2018), approximately 86% of annual aboveground woody increment in a forest in Michigan (Gough et al., 2008), and up to 60–90% of aboveground woody increment in Hubbard Brook Forest (Fahey et al., 2005). At Harvard Forest, and in our predictions for Boston based on stem-level allometries, somewhat more aboveground production was annually allocated to foliar biomass than woody biomass (Table 4.S3). In all cases, empirical study suggests that both foliar biomass production and woody biomass increment are both large and roughly comparable fractions of annual aboveground productivity.

Many forest studies have used fine litterfall to measure C assimilation allocated to annual foliar biomass production (Fahey et al., 2005; Gough et al., 2008; Klein and Hoch, 2015). In this study we estimated annual foliar biomass production via allometric predictions using stem DBH, either predicting leaf area or leaf biomass fraction (Jenkins et al., 2003; McPherson et al., 2016). As outlined above, the live foliar biomass in any one year may be expected to include C fixed in the previous year, and some amount of live foliar biomass C may be reabsorbed prior to leaf fall at the end of the growing season. However, as indicated above, we expect that over multi-year time scales these processes are in general equilibrium. Given that the allometric approach on a per-stem basis predicts C assimilation to foliar biomass roughly comparable to field measurements in rural forests, we have used predicted live-leaf foliar biomass as a proxy for C assimilation to foliage in our tree growth model.

4.S2 Carbon uptake and allocation in turfgrass

A fraction of total urban vegetation area and C exchange can be expected to take place in managed grass turf or lawn areas, which form a variable portion of urban vegetation in the landscape (Kremer et al., 2016). These areas often receive irrigation and fertilizer inputs as well as regular disturbances in the form of soil aeration and maintenance clipping and removal of aboveground biomass (Qian and Follett, 2012). The main pools of C in turf systems include clipped and removed aboveground biomass, an equilibrium “stubble” pool of aboveground living and dead biomass with high rate of turnover, belowground root biomass, and the associated soil organic carbon pool (Falk, 1976).

The intensive management of urban turf grass complicates any assessment of the spatiotemporal distribution of its biogenic C fluxes. Under regular maintenance the aboveground pool can be expected to be occasionally removed and redistributed into other human-mediated C flows such as waste management or composting that likely result in relatively rapid re-release as CO_2 (Kellett et al., 2013). However, this aboveground growth increment still represents an annual net uptake atmospheric of C to new biomass similar to annual woody biomass and leaf production in urban trees. Like urban tree litter, clipped aboveground vegetation in turf systems is also likely to be largely removed and processed or released in disjunct times and locations (Templer et al., 2015). Both tree leaf litter and lawn clippings represent a net biogenic capture of C which on an annual basis is presumably retained for some period before re-release. As such, we estimate net C uptake based on the net production of aboveground biomass in both turf grass and urban trees, irrespective of the relative longevity or depositional fate of this biomass.

Several studies have focused on C uptake and storage of SOC in turf grass. Studies have reported consistent gains to SOC in turf grass systems of 0.03 up to 0.14 kgC m^{-2} yr^{-1} within the first several years of conversion, but which are sensitive to local climate and intensive management such as in residential lawns and golf courses (Pouyat et al., 2006; Qian et al., 2010; Qian and Follett, 2012). Addition of compost can increase long-term turf grass SOC stocks (Beesley, 2012), though it is unclear how SOC change with direct C inputs should be counted in terms of in-situ C fixation and release. The aboveground biomass C pool and net C allocation to aboveground tissues may often amount to a small fraction of belowground C storage and allocation, including SOC (L. Kong et al., 2014).

Studies have also demonstrated that turfgrasses can be a net source or sink of C dependent on seasonal soil temperature and precipitation (Hiller et al., 2011; Zhou et al., 2012). However, only a handful of studies have directly measured annual net C uptake and its specific allocation in urban turf grass tissues, demonstrating considerable variability between sites and typically focused on the aboveground portion of NPP only. Falk (1980) reported NPP (assuming 44% C per dry gram biomass) of approximately 0.73 kgC m^{-2} yr^{-1} in irrigated and fertilized and un-irrigated/fertilized lawns in suburban Washington DC, accounting for allocation to both belowground root and aboveground clipping- and stubble C pools. Kaye et al. (2005) measured aboveground NPP of approximately 0.2 kgC m^{-2} yr^{-1} in herbaceous lawn vegetation under nominal irrigation, fertilization, and clipping in Ft. Collins, Colorado.. Golubiewski (2006) studied vegetation C storage in residential yards in the Front Range region of Colorado, finding a mean of 0.14 kgC m^{-2} yr^{-1}aboveground production in clippings and stubble, with greater production under more intensive management. Milesi et al. (2005) compiled field studies of urban turf grass showing approximately 0.05–0.25 kgC m^{-2} yr^{-1}in total aboveground biomass productivity. Aboveground NPP in minimally managed turf in tropical Singapore was measured up to 0.38 kgC m^{-2} yr^{-1}, assuming no dormancy period (Ng et al., 2015). Wilsey and Polley (2006) measured peak aboveground productivity of 0.27 kgC m^{-2} yr^{-1} in Texas grasslands dominated by introduced C4 grass species. Treating removed aboveground biomass as an annual C source, Jo and McPherson (1995) estimated net annual C uptake in above- and below-ground biomass in urban turf in Chicago at approximately 0.09 kgC m^{-2} yr^{-1}.

Other studies have examined gas flux to infer net productivity in urban turf grass. Miller et al., (2018) used eddy covariance measures in non-irrigated or fertilized lawn and an intensively managed golf course in Minneapolis, Minnesota, to estimate mid-summer mean gross primary production (GPP) of 6–12 gC m^{-2} d^{-1}. Assuming NPP is 62% of GPP in managed lawn systems (Falk, 1980) and a 240 day growing season (Peters and McFadden, 2012), this figure implies a maximum net above- and belowground production of approximately 0.9–1.8 kgC m^{-2} yr^{-1}but the authors also cite measured annual C flux in the lawn site of 0.09 (net source) to -0.07 kgC m^{-2} yr^{-1}due in part to rapid losses of lawn clippings left to decay on site (Hiller et al., 2011). Peters and McFadden (2012) reporting on the same site showed growing season (April–November) net ecosystem C uptake of 0.21 kgC m^{-2} yr^{-1}in irrigated golf course and 0.12 kgC m^{-2} yr^{-1}in non-irrigated lawn. Wu and Bauer (2012) used high-resolution satellite imagery over Roseville, Minnesota, in concert with a light use efficiency model to estimate similar net primary productivity (above- and belowground) of 0.77 kgC m^{-2} yr^{-1}for nominal lawn grass and 1.1 kgC m^{-2} yr^{-1} for golf course grass. Sod grown under warmer conditions in Georgia showed somewhat stronger annual net ecosystem uptake of 0.31–0.52 kgC m^{-2} yr^{-1}based on eddy covariance measurements (Pahari et al., 2018). Christen et al. (2011) estimated soil and lawn vegetation respiration of 0.28 kgC m^{-2} yr^{-1} in Vancouver, British Columbia, considerably lower than the approximately 0.82 kgC m^{-2} yr^{-1} reported in urban and suburban lawns in the Boston region (Decina et al., 2016).

This study did not attempt to estimate annual C flux due to changes in SOC stock, which may be considerable in the first several years after lawn establishment (Qian et al., 2010) but on an annual basis tend to be very small in urban soils compared to C allocation to plant tissues (Qian and Follett, 2012). We infer from the previous atmospheric and field studies of lawn C uptake that a large fraction of annual NPP in these systems is allocated belowground, but that relatively high soil respiration rates tend to lead to overall smaller NEE than forest systems. We assumed mean turfgrass NPP (above- and belowground) of 0.903 (SD 0.161) to roughly accord with the findings of Miller et al. (2018) on GPP, Hiller et al. (2011) on NEE, and Decina et al. (2016) on lawn soil respiration rate (see Methods).

Table 4.S1: Total area (ha) of different cover types in the LULC classes used in this study. Fraction of total study area shown in parentheses. Tree biomass not shown.

LULC	**Area**	**Canopy**	**Impervious**	**Pervious classes**		
				Turfgrass	Sub-canopy	Barren
Forest	1020	805	101	128	794	20
Developed	4710	484	3688	258	311	437
HD Resid.	4827	1454	2949	436	969	460
LD Resid.	245	110	81	41	94	29
Other Veg.	1315	274	284	553	224	263
Water	247	29	10	--	--	--
Total	**12455**	**3164 (25%)**	**7143 (57%)**	**1420 (11%)**	**2392 (19%)**	**1209 (10%)**

Table 4.S2: Factors used to calculate components of biomass growth in open-grown and street tree records used in annual growth simulations (see Trlica et al. [2020]). Taxon-specific allometric equations (Northeast region) for aboveground wood volume, foliar biomass and factors for foliar dry weight (dw) were taken from McPherson et al. (2016), and wood density factors were taken from Zanne et al. (2009), except where noted. Root biomass was set to default of 0.28 of predicted aboveground biomass, following McPherson et al. (2016). Aboveground biomass was calculated via wood volume, predicted as volume (m^3) = $B0*DBH^{B1}$, with DBH in cm, except where noted.

Taxon	# in record	Leaf dw (g m^{-2})	Wood density (kg m^{-3})	Wood Volume B_0	Wood Volume B_1
Acer campestre[d,e]	29	102.03[a]	508[a]	0.000284	2.310647
Acer platanoides	575	62.05	520	0.001942	1.785
Acer pseudoplatanus[d,e]	1	102.03[a]	508[a]	0.000284	2.310647
Acer rubrum[c]	79	72.68	490	0.1970	2.1933
Acer saccharum[d]	13	80.77	560	0.000284	2.310647
Aesculus hippocastanum[d]	3	85.38	500[b]	0.000284	2.310647
Carya ovata[d,e]	1	102.03[a]	640	0.000284	2.310647
Catalpa[d,e]	1	102.03[a]	380[b]	0.000284	2.310647
Celtis occidentalis[e]	2	102.03[a]	490	0.001416	1.928
Crataegus spp.[d,e]	1	102.03[a]	520[b]	0.000284	2.310647
Fagus grandifolia[c,e]	3	102.03[a]	585[b]	0.1957	2.3916
Fraxinus pennsylvanica	187	109.44	530	0.000589	2.206
Ginkgo biloba[d]	55	130.59	520[b]	0.000284	2.310647
Gleditsia triacanthos[e]	319	124.66	600	0.000506	2.22
Koelreuteria amurensis[d,e]	1	102.03[a]	508[a]	0.000284	2.310647
Koelreuteria paniculata[d,e]	1	102.03[a]	620[b]	0.000284	2.310647
Liquidambar styraciflua	5	93.78	460	7.99E-05	2.560469
Maackia amurensis[d,e]	3	102.03[a]	508[a]	0.000284	2.310647
Magnolia[d,e]	1	102.03[a]	508[a]	0.000284	2.310647
Malus spp[d]	46	109.68	610[b]	0.000284	2.310647
Platanus acerifolia	124	110.02	500	5.90E-05	2.673578
Prunus serrulata[d]	60	99.32	560[b]	0.000284	2.310647
Pyrus calleryana[d]	81	130.15	600[b]	0.000284	2.310647

Quercus macrocarpa[e]	7	102.03[a]	580	0.000243	2.415
Quercus michauxii[d,e]	1	102.03[a]	600	0.000284	2.310647
Quercus palustris[d]	23	88.17	580	0.000284	2.310647
Quercus rubra[d]	62	96.79	560	0.000284	2.310647
Robinia pseudoacacia[d,e]	1	102.03[a]	660	0.000284	2.310647
Sophora japonica[d,e]	1	102.03[a]	508[a]	0.000284	2.310647
Syringa reticulata[d]	11	102.03[a]	508[a]	0.000284	2.310647
Tilia americana[d,e]	16	141.78	320	0.000284	2.310647
Tilia cordata	629	141.78	420	0.000936	2.042
Ulmus[d,e]	55	99.77	460[b]	0.000284	2.310647
Ulmus crassifolia[d,e]	2	102.03[a]	590	0.000284	2.310647
Ulmus european[d,e]	5	102.03[a]	508[a]	0.000284	2.310647
Unknown spp[d,e]	1	102.03[a]	508[a]	0.000284	2.310647
Zelkova serrata	186	73.05	520	5.02E-05	2.674757

[a] uses default wood density value equal to the weighted average of taxa with known foliar weight or wood density.

[b] taken from McPherson et al. (2016), Table 11.

[c] uses direct aboveground biomass equation taken from MacPherson et al. (2016), Table 8 – volume and biomass equations from rural: Biomass (kg) = B_0*DBH^{B1}, DBH in cm.

[d] uses aboveground wood volume equation for Urban General Broadleaf (McPherson et al., 2016).

[e] foliar biomass predicted based on foliar biomass fraction (foliar biomass:aboveground biomass) calculated from empirical equation fit from foliar- and aboveground biomass predicted for other trees in the data set with foliar biomass allometries: $\log(y) = B_0 + B_1*\log(x)$ where x = predicted aboveground biomass and y = foliar biomass, $B_0 = -1.539$, and $B_1 = -0.287$

Table 4.S3: Total city-wide C flux by LULC (median and central 95% of estimates), GgC yr^{-1}. Negative values indicate net C sink, positive values indicate net C source.

LULC	Tree NPP	Turfgrass NPP	Soil Respiration	NEE
Forest	-6.2 (-2.7 – 15)	-1.1 (-0.7 – -1.5)	4.6 (4.6 – 4.6)	-2.7 (-11.3 – 0.7)
Developed	-3.9 (-3.5 – -4.7)	-2.3 (-1.5 – -3.1)	5.5 (5.4 – 5.5)	-0.7 (-1.7 – 0.2)
HD Resid.	-12.2 (-10.4 – -15)	-3.9 (-2.6 – -5.3)	19.2 (19.1 – 19.3)	3.1 (0 – 5.3)
LD Resid.	-0.9 (-0.7 – -1.2)	-0.4 (-0.2 – -0.5)	1.6 (1.6 – 1.6)	0.4 (0.1 – 0.6)
Other Veg.	-2.3 (-1.8 – -3.1)	-4.9 (-3.2 – -6.6)	6.8 (6.8 – 6.9)	-0.4 (-2.2 – 1.4)
Total	**-25.7 (-19.3 – -38.4)**	**-12.7 (-8.3 – -17.2)**	**38 (37.8 – 38.1)**	**-0.6 (-13.9 – 7.3)**

Table 4.S4: Summary of metrics comparing forest biogenic C dynamics in >85% canopy covered pixels in Boston study region compared (by LULC and for Total map area), and results of 15 years of field monitoring at Harvard Forest (HF) EMS site. Street refers to pixels modeled using alternative urban-specific allometric equations. Figures indicate median and central 95% of data except for HF, which shows mean and total range of reported observations.

LULC	Aboveground Biomass (MgC ha^{-1})	Aboveground NPP (MgC ha^{-1} yr^{-1})	Aboveground Woody Increment (MgC ha^{-1} yr^{-1})	AGWI:ANPP
Forest	141.9 (74.1–221.1)	5.7 (3.9–9.7)	2.2 (1.1–3.5)	0.37 (0.27–0.49)
Developed	132.6 (59.8–204.4)	8.0 (4.0–11.0)	3.2 (1.7–3.9)	0.38 (0.3–0.54)
HD Resid.	136.0 (90.5–191.0)	8.9 (5.7–11.4)	3.3 (2.2–4)	0.37 (0.31–0.53)
LD Resid.	132.5 (92.0–186.0)	8.5 (5.3–0.9)	3.3 (2.2–3.9)	0.38 (0.31–0.53)
Other Veg.	135.1 (61–198.6)	7.9 (4.4–10.9)	3.1 (1.7–3.9)	0.37 (0.3–0.53)
Total	138.9 (69.1–218.1)	6.2 (3.9–10.6)	2.4 (1.1–3.8)	0.37 (0.270.53)
Street	8.2 (0–89.4)	0.7 (0–5.5)	0.4 (0–2.6)	0.54 (0.37–0.76)
HF	110.1 (118.0–127.0)	3.4 (3.1–3.8)	1.7 (1.4–2.0)	0.50 (0.44–0.52)

CHAPTER FIVE: Conclusions

The preceding chapters are either already published in the peer-reviewed literature (Chapter 2), are provisionally accepted for publication (Chapter 3), or are in the process of being set into manuscript form for submission for peer review (Chapter 4). Each dissertation chapter presents either the original text of the published or submitted work or a reasonable facsimile to the work that will be submitted, including figures, tables, and supplemental information. Figures, tables, and supplemental information have been renumbered from their originals to better organize them within this document. For manuscripts either in review or yet to be submitted, the final published material will supersede results and discussions included in the current dissertation.

To put this work in context, we note that urban landscapes are some of the only ecosystems — along with perhaps cultivated agricultural land (Tilman et al., 2001) and desertified land (Zeng and Yoon, 2009) — expected to grow in extent over the coming decades (Seto et al., 2012). Fitting with the advent of the Anthropocene era, these sorts of human-defined and human-managed ecosystem will come to occupy an increasingly important role in the workings of the earth system. This transition to human-mediated landscapes is also occurring within the context of the increasingly dramatic effects of human activity on the earth's climate. Managing the simultaneous shift to an urbanized world of increasingly human-mediated landscapes, while preparing for and mitigating the effects of anthropogenic climate change for the people in those landscapes, will be one of the defining social problems of the 21st century.

Municipal authorities have begun to consider policy responses to climate change mitigation and adaptation within the context of their urban landscapes (Broto and Bulkeley, 2013), including not only reduction in local climate changing emissions but also optimizing activity patterns, the built environment, or the local production of “green infrastructure” services to act as a buffer for climate change effects. However, considerable ignorance remains about the workings of urban ecosystems (Groffman et al., 2017; Hutyra et al., 2014). Dependence upon imperfectly understood socio-ecological systems that may respond unpredictably to policy intervention or to future change bodes ill for mounting a successful response to the challenges ahead. To address these shortcomings in our knowledge, the theme of the preceding work has been to examine selected landscape-scale ecosystem functions of an urban ecosystem that may prove relevant to climate change responses at the city scale.

5.1 Summary of work

This research quantifies albedo variation across the urbanized Boston metropolitan region at a 30 m resolution estimated via a Landsat-MODIS data fusion approach (Shuai et al., 2011), capturing the spatial covariation of albedo with other prominent land cover characteristics. Our work implies that attempting to quantify albedo as a feature of urban land cover via low-resolution MODIS-only data is likely to contain significant artifacts due to adjacent open water features that are not straightforward to correct. In accord with general intuition about drivers of the urban heat island effect, we show lower albedo with increasing urbanization intensity, though the effect is mainly present at the scale of large landscape areas and is not large relative to variation in metrics like fraction of impervious cover or tree canopy. These results empirically validate the idea that extreme urban summertime temperatures might in principle be moderated by artificially raising the albedo of built surfaces (Mackey et al., 2012). However, our findings also raise the question as to whether or not this decline in albedo is a common gradient of land cover character in urbanized areas more generally, given the high variability noted in the handful of studies that have measured urban surface albedos in other areas (Taha, 1997). Moreover, in providing a preliminary empirical boundary on the albedo of urban landcover and its variability from nearby rural areas, our finding also argues for deeper research into the appropriateness of modeling assumptions used in urban climate numerical models (Vahmani and Ban-Weiss, 2016).

Recent research suggests that urban areas may be host to substantial amounts of forest biomass (Raciti et al., 2012a; Rao et al., 2013b), and that tree growth in the city may be enhanced under some urban growing conditions and with enhanced light availability (Briber et al., 2015; Reinmann and Hutyra, 2017; Smith et al., 2019). Our work shows that trees in the city of Boston may assimilate up to approximately 50% more C annually than expected under assumptions of rural growth rates, much of it taking place in otherwise densely developed residential areas in addition to the expected uptake in remaining forest fragments. Our future projections of urban forest function under alternate tree management policy further suggest that different prescriptions may maximize some functions over others. Limiting mortality in the rarer large trees may tend to preserve or even expand canopy cover and standing biomass, which could better aid in temperature moderation as well as other desirable services. Alternatively, expanded tree planting in available road buffers may tend to maximize total C uptake potential. In all cases, a policy of non-intervention under current trends suggests that some ecosystem functions like canopy cover may decline over time. Recent shortcomings in Boston in increasing tree cover through new planting highlight the potential difficulties in meeting goals related to optimizing ecosystem services in the city. Our work provides a Boston-specific estimate of the potential scope for interventions along these lines, and emphasizes the importance of prioritizing these efforts towards meeting local climate and quality of life protections. At the same time, our results suggest that the potential for significant offsetting of local fossil fuel emissions via local tree C uptake may be minimal, given the scale of ongoing emissions. Furthermore, our work sheds light on a persistent difficulty with estimating ecosystem functions related to forests as a municipal asset, namely the lack of a coherent monitoring system for the urban forest. Data on canopy extent or standing biomass at sufficient spatial resolution, or regular surveys of tree growth, health, and location, are decidedly bespoke and infrequently collected in Boston and in many other cities.

As urban municipalities have begun to take local steps to prepare for and mitigate climate change effects, interest in finding potential pathways for reducing local CO_2 emissions have grown. In service of these goals, research is actively underway towards more precisely and routinely monitoring ongoing CO_2 emissions from the urban surface (Gurney et al., 2015; Sargent et al., 2018). A key remaining difficulty in monitoring urban CO_2 emissions is the disentanglement of biogenic C fluxes co-occurring with fossil CO_2 emissions, particularly during the growing season in temperate areas. Our work and other recent research has furthermore suggested that some biogenic fluxes, such as soil respiration from highly-managed areas, may locally exceed fossil C emissions in certain places and times (Decina et al., 2016). Our research, scaling up 1 m data on soil cover and land use, as well as predictions of tree and lawn C uptake, shows that high soil respiration may essentially negate any net C uptake to vegetation in the city on an annual basis. At the same time, the size of these fluxes and their potential for temporal offset from one another suggests that the localized C fluxes (both to and from the atmosphere) may be substantial, and capable of obscuring the atmospheric signal of fossil C release. Rounding out the picture of the preceding chapter, our results further argue that local biogenic C uptake is unlikely to provide a substantial C offset opportunity compared to the scale of local fossil C emissions, on the order of at most a few percent per year even if discounting the net C efflux from soil respiration. The essentially balanced biogenic C flux of Boston's urban ecosystem more concretely underlines the need to address local greenhouse gas emissions abatement from the direction of energy efficiency in housing and transportation, rather than reliance on biogenic C offsetting. We acknowledge, however, the paucity of local and measurements of many of the critical components of biogenic C flux in the city, and offer our C budget as a first attempt at an estimation of scale.

5.2 Directions for future work

The research of this dissertation specifically targets Boston and its surrounding region as a case study of urban ecosystems more generally. This region, however, is hardly to be taken as an exhaustive exemplar of all the potential variation in urban ecosystems or the factors that may critically influence their function, including biophysical setting, land use modalities and policy, or development history (Ossola and Hopton, 2018a). In many ways this work was conceived out of the necessities of data availability, as an unusual amount of prior research has occurred at Boston-area institutions, leaving behind an unusual depth of empirical data on the area, including field and remote sensing data (e.g. Decina et al., 2016; Raciti et al., 2014; Reinmann and Hutyra, 2017; Smith et al., 2019).

Research into "natural" (less directly human influenced) ecosystems in North America has benefitted greatly from the availability of data from long-term and comparative research, such as through the Long-Term Ecological Research (LTER), Ameriflux, and NEON research networks (Hargrove et al., 2003; Hobbie et al., 2003; Schimel et al., 2007). The two LTER urban sites in Phoenix, Arizona, and Baltimore, Maryland, have produced a wealth of insight over the years on the commonalities and differences between these urban ecosystems across very different climatic settings (Cadenasso et al., 2006; Grimm and Redman, 2004). Of necessity the research in these areas has been focused on differing aspects of the urban ecosystem, including for instance the formation of the urban heat- or "cool"-island in Phoenix (Connors et al., 2013) and stream ecosystem function in Baltimore (Kaushal et al., 2014). The topic of albedo variation has not received as much attention in general, as evidenced by the relatively few empirical studies of the matter to date. Carbon flux research in the urban context has been advanced recently with the advent of the CO2-USA network with active research in Salt Lake City, Boston, Baltimore, Indianapolis, San Francisco, and Los Angeles. This research has primarily been focused on development of methods for the measurement of fossil C flux rather than specifics of urban forest biogeochemistry or biogenic C flux (Gurney et al., 2015). Alternatively, there exist publicly available and spatially extensive archives of satellite earth observations from, for instance, Landsat and MODIS (Davis et al., 2015), capable of discerning key features of land cover that have proved useful in estimating some aspects of ecosystem function in the urban context (Hardiman et al., 2017). However, most of the readily available remote sensing data for the earth's surface is collected at coarse to moderate resolution (km-scale to 30 m) that necessarily obscures key features shown in this study to have important effects on ecosystem function in urban areas, where smaller-scale spatial heterogeneity dominates.

Between the growing interest at the municipal scale in strategies for minimizing the local causes and consequences of climate change, and the current state of research into and understanding of the functioning of urban ecosystems, is a critical gap in both empirical data and comparative study. Urban ecosystems likely have broadly comparable features and commonalities that both unite and set them apart just as other ecosystems do, such as the persistence of the urban heat island effect that has been noted by observers for more than a century (Meyer, 1991). On the other hand, the biophysical and climatic context of each city (Ossola and Hopton, 2018a), as well as factors under direct and indirect human influence such as its community of native and imported indwelling species (Alberti, 2015), development history (Dietzel et al., 2005), and management practices (Polsky et al., 2014), likely also play determinative roles in the structure and function of these ecosystems. Beside the emergence of specifically urban-focused research networks, less research has been done to directly quantitatively compare metrics of and controls on ecosystem function across cities. Furthermore, little institutional support appears to exist at any scale of government to frequently or systematically collect key high-quality and spatially explicit data on aspects of ecosystem function such as tree canopy coverage, near-surface meteorology (Wang et al., 2017), or air quality — or indeed the lived experience of the people therein. In the absence of current and spatio-temporally resolved data on the state of the urban ecosystem, policy towards adapting or modifying these landscapes to the needs of its inhabitants or the rigors of a changing climate appear to be, at least occasionally, disconcertingly speculative.

New global-coverage satellite remote sensing data is becoming available at resolutions of 10–20 m, which may help to better resolve some of the small spatial-scale processes at work in urban ecosystems (Lefebvre et al., 2016). However, the point must be underlined that in order to better predict urban ecosystem response to climate change or to policy intervention, a more refined empirically based understanding is needed. Either (or both) a more generalizable model of urban ecosystem function must be obtained through more inter-city comparative research, or efforts at the local level to routinely collect and synthesize data on the status of key functional metrics such as canopy cover, impervious surface extent, and temperature will be required. For example, while techniques such as aerial LiDAR and multispectral photometry during the leaf-off period have become more commonly used in urban areas to obtain information on land surface elevation and change in development extent (Yan et al., 2015), such techniques are not routinely applied during the leaf-on period to obtain critical canopy height and extent data (King and Locke, 2013; Raciti et al., 2014; Walton et al., 2008). Moreover, a continued exclusive focus on management of ecosystem function solely in identifiable “green spaces”, as this work has shown, will necessarily miss a large portion of the activity in the urban ecosystem or its impact on the well-being of the inhabitants of cities.

As we progress through the 21st century, the human species will have to grapple with its emerging role as a controlling factor on the functioning of the earth system. How we manage the landscape of our cities, for good or for ill, will likely prove to be one of the most important determinants of our success or failure in our task of caring for our own well-being, as well as the continued health of our hybridized human-natural world.

BIBLIOGRAPHY

Akbari, H., Damon Matthews, H., Seto, D., 2012. The long-term effect of increasing the albedo of urban areas. Environmental Research Letters 7, 024004. https://doi.org/10.1088/1748-9326/7/2/024004

Akbari, H., Menon, S., Rosenfeld, A., 2009. Global cooling: Increasing world-wide urban albedos to offset CO_2. Climatic Change 94, 275–286. https://doi.org/10.1007/s10584-008-9515-9

Alberti, M., 2015. Eco-evolutionary dynamics in an urbanizing planet. Trends in Ecology and Evolution 30, 114–126. https://doi.org/10.1016/j.tree.2014.11.007

Amthor, J.S., Baldocchi, D.D., 2001. Terrestrial Higher Plant Respiration and Net Primary Production, in: Terrestrial Global Productivity. pp. 33–59. https://doi.org/10.1016/b978-012505290-0/50004-1

Argüeso, D., Evans, J.P., Fita, L., Bormann, K.J., 2014. Temperature response to future urbanization and climate change. Climate Dynamics 42, 2183–2199. https://doi.org/10.1007/s00382-013-1789-6

Arneth, A., Kelliher, F.M., McSeveny, T.M., Byers, J.N., 1998. Net ecosystem productivity, net primary productivity and ecosystem carbon sequestration in a Pinus radiata plantation subject to soil water deficit. Tree Physiology 18, 785–793. https://doi.org/10.1093/treephys/18.12.785

Arnfield, A.J., 2003. Two decades of urban climate research: A review of turbulence, exchanges of energy and water, and the urban heat island. International Journal of Climatology 23, 1–26. https://doi.org/10.1002/joc.859

Bai, X., 2016. Eight energy and material flow characteristics of urban ecosystems. Ambio 45, 819–830. https://doi.org/10.1007/s13280-016-0785-6

Ban-Weiss, G.A., Woods, J., Levinson, R., 2015. Using remote sensing to quantify albedo of roofs in seven California cities, Part 1: Methods. Solar Energy 115, 777–790. https://doi.org/10.1016/j.solener.2014.10.022

Barnes, C.A., Roy, D.P., 2010. Radiative forcing over the conterminous United States due to contemporary land cover land use change and sensitivity to snow and interannual albedo variability. Journal of Geophysical Research: Biogeosciences 115, 1–14. https://doi.org/10.1029/2010JG001428

Barsi, J.A., Schott, J.R., Palluconi, F.D., Hook, S.J., 2005. Validation of a web-based atmospheric correction tool for single thermal band instruments, in: Proceedings of the International Society for Optics and Photonics.

Bates, D., Maechler, M., Bolker, B., Walker, S.,2015. Fitting Linear Mixed-Effects Models Using lme4. Journal of Statistical Software 67, 1-48. https://doi.org/10.18637/jss.v067.i01.

Beesley, L., 2012. Carbon storage and fluxes in existing and newly created urban soils. Journal of Environmental Management 104, 158–165. https://doi.org/10.1016/j.jenvman.2012.03.024

Bellucco, V., Marras, S., Grimmond, C.S.B., Järvi, L., Sirca, C., Spano, D., 2017. Modelling the biogenic CO_2 exchange in urban and non-urban ecosystems through the assessment of light-response curve parameters. Agricultural and Forest Meteorology 236, 113–122. https://doi.org/10.1016/j.agrformet.2016.12.011

Benson-Lira, V., Georgescu, M., Kaplan, S., Vivoni, E.R., 2016. Loss of a lake system in a megacity: The impact of urban expansion on seasonal meteorology in Mexico City. Journal of Geophysical Research: Atmospheres 121, 3079–3099. https://doi.org/10.1002/2015JD024102

Bivand, R., Rundel, C., 2015. rgeos: Interface to Geometry Engine – Open Source (GEOS). R package version 0.3-11. http://CRAN.R-project.org/package=rgeos

Bivand, R., Keitt, T., Rowlingson, B., 2015. rgdal: Bindings for the Geospatial Data Abstraction Library. R package version 1.0-4. http://CRAN.R-project.org/package=rgdal

Bounoua, L., Zhang, P., Mostovoy, G., Thome, K., Masek, J., Imhoff, M., Shepherd, M., Quattrochi, D., Santanello, J., Silva, J., Wolfe, R., Toure, A.M., 2015. Impact of urbanization on US surface climate. Environmental Research Letters 10, 084010. https://doi.org/10.1088/1748-9326/10/8/084010

Brack, C.L., 2002. Pollution mitigation and carbon sequestration by an urban forest. Environmental Pollution 116, S195–S200. https://doi.org/10.1016/S0269-7491(01)00251-2

Brest, C.L., 1987. Seasonal albedo of an urban/rural landscape from satellite observations. https://doi.org/10.1175/1520-0450(1987)026<1169:SAOAUL>2.0.CO;2

Briber, B.M., Hutyra, L.R., Reinmann, A.B., Raciti, S.M., Dearborn, V.K., Holden, C.E., Dunn, A.L., 2015. Tree productivity enhanced with conversion from forest to urban land covers. PLoS ONE 10, 1–19. https://doi.org/10.1371/journal.pone.0136237

Bright, E.A., Rose, A.N., Urban, M.L., 2013. Landscan 2012. UT-Battelle, LLC, operator of Oak Ridge National Laboratory under Contract No. DE-AC05-00OR22725 with the United States Department of Energy. http://www.ornl.gov/landscan

Broto, V.C., Bulkeley, H., 2013. A survey of urban climate change experiments in 100 cities. Global Environmental Change 23, 92–102. https://doi.org/10.1016/j.gloenvcha.2012.07.005

Cadenasso, M.L., Pickett, S.T.A., Grove, M.J., 2006. Integrative approaches to investigating human-natural systems: the Baltimore ecosystem study. Natures Sciences Sociétés 14, 4–14. https://doi.org/10.1051/nss:2006002

Campagnolo, M.L., Sun, Q., Liu, Y., Schaaf, C., Wang, Z., Román, M.O., 2016. Estimating the effective spatial resolution of the operational BRDF, albedo, and nadir reflectance products from MODIS and VIIRS. Remote Sensing of Environment 175, 52–64. https://doi.org/10.1016/J.RSE.2015.12.033

Castán Broto, V., 2017. Urban governance and the politics of climate change. World Development 93, 1–15. https://doi.org/10.1016/j.worlddev.2016.12.031

Chalker-Scott, L., 2007. Impact of mulches on landscape plants and the environment—A review. Journal of Environmental Horticulture 25, 239–249.

Chave, J., Coomes, D., Jansen, S., Lewis, S.L., Swenson, N.G., Zanne, A.E., 2009. Towards a worldwide wood economics spectrum. Ecology Letters 12, 351–366. https://doi.org/10.1111/j.1461-0248.2009.01285.x

Chen, X.L., Zhao, H.M., Li, P.X., Yin, Z.Y., 2006. Remote sensing image-based analysis of the relationship between urban heat island and land use/cover changes. Remote Sensing of Environment 104, 133–146. https://doi.org/10.1016/j.rse.2005.11.016

Cheng, F.-Y., Byun, D.W., 2008. Application of high resolution land use and land cover data for atmospheric modeling in the Houston–Galveston metropolitan area, Part I: Meteorological simulation results. Atmospheric Environment 42, 7795–7811. https://doi.org/10.1016/j.atmosenv.2008.04.055

Chojnacky, D.C., Heath, L.S., Jenkins, J.C., 2014. Updated generalized biomass equations for North American tree species. Forestry 87, 129–151. https://doi.org/10.1093/forestry/cpt053

Christen, A., Coops, N.C., Crawford, B.R., Kellett, R., Liss, K.N., Olchovski, I., Tooke, T.R., Van Der Laan, M., Voogt, J.A., 2011. Validation of modeled carbon-dioxide emissions from an urban neighborhood with direct eddy-covariance measurements. Atmospheric Environment 45, 6057–6069. https://doi.org/10.1016/j.atmosenv.2011.07.040

Christen, A., Vogt, R., 2004. Energy and radiation balance of a central European City. International Journal of Climatology 24, 1395–1421. https://doi.org/10.1002/joc.1074

Churkina, G., 2016. The role of urbanization in the global carbon cycle. Frontiers in Ecology and Evolution 3, 144. https://doi.org/10.3389/fevo.2015.00144

City of Boston, 2016. City of Boston Greenhouse Gas Emissions Inventory 2005–2016. https://www.boston.gov/sites/default/files/imce-uploads/2018-09/boston_ghg_inventory_2005-2016.pdf

Connors, J.P., Galletti, C.S., Chow, W.T.L., 2013. Landscape configuration and urban heat island effects: assessing the relationship between landscape characteristics and land surface temperature in Phoenix, Arizona. Landscape Ecology 28, 271–283. https://doi.org/10.1007/s10980-012-9833-1

Crawford, B., Christen, A., 2015. Spatial source attribution of measured urban eddy covariance CO_2 fluxes. Theoretical and Applied Climatology 119, 733–755. https://doi.org/10.1007/s00704-014-1124-0

Crawford, B., Grimmond, C.S.B., Christen, A., 2011. Five years of carbon dioxide fluxes measurements in a highly vegetated suburban area. Atmospheric Environment 45, 896–905. https://doi.org/10.1016/j.atmosenv.2010.11.017

Curtis, P.S., Vogel, C.S., Gough, C.M., Schmid, H.P., Su, H.B., Bovard, B.D., 2005. Respiratory carbon losses and the carbon-use efficiency of a northern hardwood forest, 1999–2003. New Phytologist 167, 437–456. https://doi.org/10.1111/j.1469-8137.2005.01438.x

Danford, R.S., Strohbach, M.W., Ryan, R., Nicolson, C., Warren, P.S., 2014. What does it take to achieve equitable urban tree canopy distribution? A Boston case study. Cities and the Environment 7, Article 2.

Davies, Z.G., Edmondson, J.L., Heinemeyer, A., Leake, J.R., Gaston, K.J., 2011. Mapping an urban ecosystem service: Quantifying above-ground carbon storage at a city-wide scale. Journal of Applied Ecology 48, 1125–1134. https://doi.org/10.1111/j.1365-2664.2011.02021.x

Davis, B.N., Werpy, J., Friesz, A., Impecoven, K., Quenzer, R.L., Maiersperger, T., Meyer, D.J., 2015. Interactive access to LP DAAC satellite data archives through a combination of open-source and custom middleware web services. IEEE Geoscience and Remote Sensing Magazine 3, 8–20. https://doi.org/10.1109/MGRS.2015.2505999

Decina, S.M., Hutyra, L.R., Gately, C.K., Getson, J.M., Reinmann, A.B., Short Gianotti, A.G., Templer, P.H., 2016. Soil respiration contributes substantially to urban carbon fluxes in the greater Boston area. Environmental Pollution 212, 433–439. https://doi.org/10.1016/j.envpol.2016.01.012

Decina, S.M., Templer, P.H., Hutyra, L.R., 2018. Atmospheric inputs of nitrogen, carbon, and phosphorus across an urban area: Unaccounted fluxes and canopy influences. Earth's Future 6, 134–148. https://doi.org/10.1002/2017EF000653

DeFries, R.S., Rudel, T., Uriarte, M., Hansen, M., 2010. Deforestation driven by urban population growth and agricultural trade in the twenty-first century. Nature Geoscience 3, 178–181. https://doi.org/10.1038/ngeo756

DeLucia, E.H., Drake, J.E., Thomas, R.B., Gonzalez-Meler, M., 2007. Forest carbon use efficiency: Is respiration a constant fraction of gross primary production? Global Change Biology 13, 1157–1167. https://doi.org/10.1111/j.1365-2486.2007.01365.x

Dhakal, S., 2010. GHG emissions from urbanization and opportunities for urban carbon mitigation. Current Opinion in Environmental Sustainability 2, 277–283. https://doi.org/10.1016/j.cosust.2010.05.007

Dietzel, C., Herold, M., Hemphill, J.J., Clarke, K.C., 2005. Spatio-temporal dynamics in California's Central Valley: Empirical links to urban theory. International Journal of Geographical Information Science 19, 175–195. https://doi.org/10.1080/13658810410001713407

Dixon, P.G., Mote, T.L., 2003. Patterns and causes of Atlanta's urban heat island—initiated precipitation. Journal of Applied Meteorology 42, 1273–1284. https://doi.org/10.1175/1520-0450(2003)042<1273:PACOAU>2.0.CO;2

Dobbs, C., Nitschke, C., Kendal, D., 2017. Assessing the drivers shaping global patterns of urban vegetation landscape structure. Science of the Total Environment 592, 171–177. https://doi.org/10.1016/j.scitotenv.2017.03.058

Dowle M., Srinivasan, M., 2017. data.table: Extension of 'data.frame'. R package version 1.10.4-3. https://CRAN.R-project.org/package=data.table

Dwyer, J.L., Roy, D.P., Sauer, B., Jenkerson, C.B., Zhang, H.K., Lymburner, L., 2018. Analysis ready data: Enabling analysis of the landsat archive. Remote Sensing 10, 1363. https://doi.org/10.3390/rs10091363

Escobedo, F.J., Kroeger, T., Wagner, J.E., 2011. Urban forests and pollution mitigation: Analyzing ecosystem services and disservices. Environmental Pollution 159, 2078–2087. https://doi.org/10.1016/j.envpol.2011.01.010

Escobedo, F.J., Nowak, D.J., 2009. Spatial heterogeneity and air pollution removal by an urban forest. Landscape and Urban Planning 90, 102–110. https://doi.org/10.1016/j.landurbplan.2008.10.021

ESRI, 2014. ArcGIS Desktop: Release 10. Redlands, CA: Environmental Systems Research Institute.

Estoque, R.C., Murayama, Y., Myint, S.W., 2017. Effects of landscape composition and pattern on land surface temperature: An urban heat island study in the megacities of Southeast Asia. Science of the Total Environment 577, 349–359. https://doi.org/10.1016/j.scitotenv.2016.10.195

Fahey, T.J., Siccama, T.G., Driscoll, C.T., Likens, G.E., Campbell, J., Johnson, C.E., Battles, J.J., Aber, J.D., Cole, J.J., Fisk, M.C., Groffman, P.M., Hamburg, S.P., Holmes, R.T., Schwarz, P.A., Yanai, R.D., 2005. The biogeochemistry of carbon at Hubbard Brook. Biogeochemistry 75, 109–176. https://doi.org/10.1007/s10533-004-6321-y

Falasca, S., Catalano, F., Moroni, M., 2016. Numerical study of the daytime planetary boundary layer over an idealized urban area: Influence of surface properties, anthropogenic heat flux, and geostrophic wind intensity. Journal of Applied Meteorology and Climatology 55, 1021–1039. https://doi.org/10.1175/JAMC-D-15-0135.1

Falk, J.H., 1980. The primary productivity of lawns in a temperate environment. The Journal of Applied Ecology 17, 689–696. https://doi.org/10.2307/2402647

Falk, J.H., 1976. Energetics of a Suburban Lawn Ecosystem. Ecology 57, 141–150. https://doi.org/10.2307/1936405

Faraway, J.J., 2006. Extending the linear model with R: Generalized linear, mixed effects and nonparametric regression models. Chapman & Hall/CRC Taylor & Francis, Boca Raton, Florida.

Feng, S., Lauvaux, T., Newman, S., Rao, P., Ahmadov, R., Deng, A., Díaz-Isaac, L.I., Duren, R.M., Fischer, M.L., Gerbig, C., Gurney, K.R., Huang, J., Jeong, S., Li, Z., Miller, C.E., O'Keeffe, D., Patarasuk, R., Sander, S.P., Song, Y., Wong, K.W., Yung, Y.L., 2016. Los Angeles megacity: A high-resolution land-atmosphere modelling system for urban CO_2 emissions. Atmospheric Chemistry and Physics 16, 9019–9045. https://doi.org/10.5194/acp-16-9019-2016

Fortuniak, K., 2008. Numerical estimation of the effective albedo of an urban canyon. Theoretical and Applied Climatology 91, 245–258. https://doi.org/10.1007/s00704-007-0312-6

Frey, C.M., Parlow, E., 2009. Geometry effect on the estimation of band reflectance in an urban area. Theoretical and Applied Climatology 96, 395–406. https://doi.org/10.1007/s00704-008-0048-y

Gately, C.K., Hutyra, L.R., 2017. Large uncertainties in urban-scale carbon emissions. Journal of Geophysical Research: Atmospheres 11,242–11,260. https://doi.org/10.1002/2017JD027359

Gately, C.K., Hutyra, L.R., Wing, I.S., Brondfield, M.N., 2013. A bottom up approach to on-road CO_2 emissions estimates: Improved spatial accuracy and applications for regional planning. Environmental Science and Technology 47, 2423–2430. https://doi.org/10.1021/es304238v

Georgescu, M., Morefield, P.E., Bierwagen, B.G., Weaver, C.P., 2014. Urban adaptation can roll back warming of emerging megapolitan regions. Proceedings of the National Academy of Sciences 111, 2909–2914. https://doi.org/10.1073/pnas.1322280111

Georgescu, M., Moustaoui, M., Mahalov, A., Dudhia, J., 2012. Summer-time climate impacts of projected megapolitan expansion in Arizona. Nature Climate Change 3, 37–41. https://doi.org/10.1038/nclimate1656

Golubiewski, N., 2012. Is there a metabolism of an urban ecosystem? An ecological critique. Ambio 41, 751–764. https://doi.org/10.1007/s13280-011-0232-7

Golubiewski, N.E., 2006. Urbanization transforms prairie carbon pools: Effects of landscaping in Colorado’s Front Range. Ecological Applications 16, 555–571.

Gómez-Baggethun, E., Barton, D.N., 2013. Classifying and valuing ecosystem services for urban planning. Ecological Economics 86, 235–245. https://doi.org/10.1016/j.ecolecon.2012.08.019

Gough, C.M., Vogel, C.S., Schmid, H.P., Su, H.B., Curtis, P.S., 2008. Multi-year convergence of biometric and meteorological estimates of forest carbon storage. Agricultural and Forest Meteorology 148, 158–170. https://doi.org/10.1016/j.agrformet.2007.08.004

Gregg, J.W., Jones, C.G., Dawson, T.E., 2003. Urbanization effects on tree growth in the vicinity of New York City. Nature 424, 183–7. https://doi.org/10.1038/nature01728

Grimm, N.B., Redman, C.L., 2004. Approaches to the study of urban ecosystems: The case of Central Arizona—Phoenix. Urban Ecosystems 7, 199–213. https://doi.org/10.1023/B:UECO.0000044036.59953.a1

Groffman, P.M., Cadenasso, M.L., Cavender-Bares, J., Childers, D.L., Grimm, N.B., Grove, J.M., Hobbie, S.E., Hutyra, L.R., Darrel Jenerette, G., McPhearson, T., Pataki, D.E., Pickett, S.T.A., Pouyat, R. V., Rosi-Marshall, E., Ruddell, B.L., 2017. Moving towards a new urban systems science. Ecosystems 20, 38–43. https://doi.org/10.1007/s10021-016-0053-4

Groffman, P.M., Law, N.L., Belt, K.T., Band, L.E., Fisher, G.T., 2004. Nitrogen fluxes and retention in urban watershed ecosystems. Ecosystems 7, 393–403. https://doi.org/10.1007/s10021-003-0039-x

Groleau, D., Mestayer, P.G., 2013. Urban morphology influence on urban albedo: A revisit with the SOLENE model. Boundary-Layer Meteorology 147, 301–327. https://doi.org/10.1007/s10546-012-9786-6

Gurney, K.R., Mendoza, D.L., Zhou, Y., Fischer, M.L., Miller, C.C., Geethakumar, S., de la Rue du Can, S., 2009. High resolution fossil fuel combustion CO_2 emission fluxes for the United States. Environmental Science & Technology 43, 5535–5541. https://doi.org/10.1021/es900806c

Gurney, K.R., Romero-Lankao, P., Seto, K.C., Hutyra, L.R., Duren, R., Kennedy, C., Grimm, N.B., Ehleringer, J.R., Marcotullio, P., Hughes, S., Pincetl, S., Chester, M. V., Runfola, D.M., Feddema, J.J., Sperling, J., 2015. Climate change: Track urban emissions on a human scale. Nature 525, 179–181. https://doi.org/10.1038/525179a

Haashemi, S., Weng, Q., Darvishi, A., Alavipanah, S.K., 2016. Seasonal variations of the surface urban heat Island in a semi-arid city. Remote Sensing 8, 352. https://doi.org/10.3390/rs8040352

Hafner, J., Kidder, S.Q., 1999. Urban heat island modeling in conjunction with satellite-derived surface/soil parameters. Journal of Applied Meteorology 38, 448–465. https://doi.org/10.1175/1520-0450(1999)038<0448:UHIMIC>2.0.CO;2

Hardiman, B.S., Wang, J.A., Hutyra, L.R., Gately, C.K., Getson, J.M., Friedl, M.A., 2017. Accounting for urban biogenic fluxes in regional carbon budgets. Science of the Total Environment 592, 366–372. https://doi.org/10.1016/j.scitotenv.2017.03.028

Hargrove, W.W., Hoffman, F.M., Law, B.E., 2003. New analysis reveals representativeness of the AmeriFlux network. Eos, Transactions American Geophysical Union 84, 529. https://doi.org/10.1029/2003EO480001

Herold, M., Couclelis, H., Clarke, K.C., 2005. The role of spatial metrics in the analysis and modeling of urban land use change. Computers, Environment and Urban Systems 29, 369–399. https://doi.org/10.1016/j.compenvurbsys.2003.12.001

Hijmans, R.J., 2017. raster: Geographic Data Analysis and Modeling. R package version 2.6-7. http://CRAN.R-project.org/package=raster

Hiller, R. V., McFadden, J.P., Kljun, N., 2011. Interpreting CO_2 fluxes over a suburban lawn: The influence of traffic emissions. Boundary-Layer Meteorology 138, 215–230. https://doi.org/10.1007/s10546-010-9558-0

Hobbie, J.E., Carpenter, S.R., Grimm, N.B., Gosz, J.R., Seastedt, T.R., 2003. The US Long Term Ecological Research Program. BioScience 53, 21–32. https://doi.org/10.1641/0006-3568(2003)053[0021:TULTER]2.0.CO;2

Homer, C., Dewitz, J., Yang, L., Jin, S., Danielson, P., Xian, G., Coulston, J., Herold, N., Wickham, J., Megown, K., 2015. Completion of the 2011 national land cover database for the conterminous United States – Representing a decade of land cover change information. Photogrammetric Engineering and Remote Sensing 81, 345–354. https://doi.org/10.1016/S0099-1112(15)30100-2

Hu, L., Brunsell, N.A., 2013. The impact of temporal aggregation of land surface temperature data for surface urban heat island (SUHI) monitoring. Remote Sensing of Environment 134, 162–174. https://doi.org/10.1016/j.rse.2013.02.022

Huete, A., Didan, K., Miura, T., Rodriguez, E.P., Gao, X., Ferreira, L.G., 2002. Overview of the radiometric and biophysical performance of the MODIS vegetation indices 83, 195–213.

Hutyra, L.R., Duren, R., Gurney, K.R., Grimm, N., Kort, E.A., Larson, E., Shrestha, G., 2014. Urbanization and the carbon cycle: Current capabilities and research outlook from the natural sciences perspective. Earth’s Future 2, 473–495. https://doi.org/10.1002/2014EF000255

Hutyra, L.R., Yoon, B., Hepinstall-Cymerman, J., Alberti, M., 2011. Carbon consequences of land cover change and expansion of urban lands: A case study in the Seattle metropolitan region. Landscape and Urban Planning 103, 83–93. https://doi.org/10.1016/j.landurbplan.2011.06.004

Imhoff, M.L., Bounoua, L., DeFries, R., Lawrence, W.T., Stutzer, D., Tucker, C.J., Ricketts, T., 2004. The consequences of urban land transformation on net primary productivity in the United States. Remote Sensing of Environment 89, 434–443. https://doi.org/10.1016/j.rse.2003.10.015

Jacobson, M.Z., Ten Hoeve, J.E., 2012. Effects of Urban Surfaces and White Roofs on Global and Regional Climate. Journal of Climate 25, 1028–1044. https://doi.org/10.1175/JCLI-D-11-00032.1

Jelinski, D.E., Wu, J., 1996. The modifiable areal unit problem and implications for landscape ecology. Landscape Ecology 11, 129–140. https://doi.org/10.1007/BF02447512

Jenerette, G.D., Harlan, S.L., Buyantuev, A., Stefanov, W.L., Declet-Barreto, J., Ruddell, B.L., Myint, S.W., Kaplan, S., Li, X., 2016. Micro-scale urban surface temperatures are related to land-cover features and residential heat related health impacts in Phoenix, AZ USA. Landscape Ecology 31, 745–760.

https://doi.org/10.1007/s10980-015-0284-3

Jenkins, J.C., Chojnacky, D.C., Heath, L.S., Birdsey, R.A., 2003. National-scale biomass estimators for United States tree species. Forest Science 49, 12–35.

Jia, W., Zhao, S., Liu, S., 2018. Vegetation growth enhancement in urban environments of the Conterminous United States. Global Change Biology 24, 4084–4094. https://doi.org/10.1111/gcb.14317

Jin, Y., Roy, D.P., 2005. Fire-induced albedo change and its radiative forcing at the surface in northern Australia. Geophysical Research Letters 32, 1–4. https://doi.org/10.1029/2005GL022822

Jo, H.K., McPherson, E.G., 1995. Carbon storage and flux in urban residential greenspace. Journal of Environmental Management 45, 109–133. https://doi.org/10.1006/jema.1995.0062

Johnson, D.P., Wilson, J.S., 2009. The socio-spatial dynamics of extreme urban heat events: The case of heat-related deaths in Philadelphia. Applied Geography 29, 419–434. https://doi.org/10.1016/j.apgeog.2008.11.004

Kaplan, S., Galletti, C.S., Chow, W.T.L., Myint, S.W., 2016. First order approximation of broadband directional albedo with high resolution Quickbird imagery: a case study for arid urban areas. GIScience and Remote Sensing 53, 303–319. https://doi.org/10.1080/15481603.2016.1153944

Kaushal, S.S., Delaney-Newcomb, K., Findlay, S.E.G., Newcomer, T.A., Duan, S., Pennino, M.J., Sivirichi, G.M., Sides-Raley, A.M., Walbridge, M.R., Belt, K.T., 2014. Longitudinal patterns in carbon and nitrogen fluxes and stream metabolism along an urban watershed continuum. Biogeochemistry 121, 23–44. https://doi.org/10.1007/s10533-014-9979-9

Kaye, J.P., McCulley, R.L., Burke, I.C., 2005. Carbon fluxes, nitrogen cycling, and soil microbial communities in adjacent urban, native and agricultural ecosystems. Global Change Biology 11, 575–587. https://doi.org/10.1111/j.1365-2486.2005.00921.x

Kellett, R., Christen, A., Coops, N.C., van der Laan, M., Crawford, B., Tooke, T.R., Olchovski, I., 2013. A systems approach to carbon cycling and emissions modeling at an urban neighborhood scale. Landscape and Urban Planning 110, 48–58. https://doi.org/10.1016/j.landurbplan.2012.10.002

Kennedy, C., Baker, L., Dhakal, S., Ramaswami, A., 2012. Sustainable urban systems: An integrated approach. Journal of Industrial Ecology 16, 775–779. https://doi.org/10.1111/j.1530-9290.2012.00564.x

Kennedy, C., Steinberger, J., Gasson, B., Hansen, Y., Hillman, T., Havránek, M., Pataki, D., Phdungsilp, A., Ramaswami, A., Mendez, G.V., 2009. Greenhouse gas emissions from global cities. Environmental Science & Technology 43, 7297–7302. https://doi.org/doi: 10.1021/es900213p

King, K.L., Locke, D.H., 2013. A comparison of three methods for measuring local urban tree canopy cover. Arboriculture and Urban Forestry 39, 62–67.

Klein, T., Hoch, G., 2015. Tree carbon allocation dynamics determined using a carbon mass balance approach. New Phytologist 205, 147–159. https://doi.org/10.1111/nph.12993

Kondo, A., Ueno, M., Kaga, A., Yamaguchi, K., 2001. The influence of urban canopy configuration on urban albedo. Boundary-Layer Meteorology 100, 225–242. https://doi.org/10.1023/A:1019243326464

Kong, F., Yin, H., James, P., Hutyra, L.R., He, H.S., 2014. Effects of spatial pattern of greenspace on urban cooling in a large metropolitan area of eastern China. Landscape and Urban Planning 128, 35–47. https://doi.org/10.1016/j.landurbplan.2014.04.018

Kong, L., Shi, Z., Chu, L.M., 2014. Carbon emission and sequestration of urban turfgrass systems in Hong Kong. Science of the Total Environment 473–474, 132–138. https://doi.org/10.1016/j.scitotenv.2013.12.012

Körner, C., 2003. Carbon limitation in trees. Journal of Ecology 91, 4–17. https://doi.org/10.1046/j.1365-2745.2003.00742.x

Kozlowski, T.T., 1992. Carbohydrate sources and sinks in woody plants. The Botanical Review 58, 107–222. https://doi.org/10.1007/BF02858600

Krayenhoff, E.S., Voogt, J.A., 2010. Impacts of urban albedo increase on local air temperature at daily-annual time scales: Model results and synthesis of previous work. Journal of Applied Meteorology and Climatology 49, 1634–1648. https://doi.org/10.1175/2010JAMC2356.1

Krehbiel, C., Henebry, G.M., 2016. A comparison of multiple datasets for monitoring thermal time in urban areas over the U.S. upper midwest. Remote Sensing 8. https://doi.org/10.3390/rs8040297

Kremer, P., Hamstead, Z.A., McPhearson, T., 2016. The value of urban ecosystem services in New York City: A spatially explicit multicriteria analysis of landscape scale valuation scenarios. Environmental Science and Policy 62, 57–68. https://doi.org/10.1016/j.envsci.2016.04.012

Larondelle, N., Haase, D., 2013. Urban ecosystem services assessment along a rural-urban gradient: A cross-analysis of European cities. Ecological Indicators 29, 179–190. https://doi.org/10.1016/j.ecolind.2012.12.022

Lauvaux, T., Miles, N.L., Deng, A., Richardson, S.J., Cambaliza, M.O., Davis, K.J., Gaudet, B., Gurney, K.R., Huang, J., O'Keefe, D., Song, Y., Karion, A., Oda, T., Patarasuk, R., Razlivanov, I., Sarmiento, D., Shepson, P., Sweeney, C., Turnbull, J., Wu, K., 2016. High-resolution atmospheric inversion of urban CO_2 emissions during the dormant season of the Indianapolis Flux Experiment (INFLUX). Journal of Geophysical Research: Atmospheres 121, 5213–5236. https://doi.org/10.1002/2015JD024473

Lefebvre, A., Sannier, C., Corpetti, T., 2016. Monitoring urban areas with Sentinel-2A data: Application to the update of the Copernicus high resolution layer imperviousness degree. Remote Sensing 8, 606. https://doi.org/10.3390/rs8070606

Li, D., Bou-Zeid, E., Oppenheimer, M., 2014. The effectiveness of cool and green roofs as urban heat island mitigation strategies. Environmental Research Letters 9, 055002. https://doi.org/10.1088/1748-9326/9/5/055002

Li, G., Weng, Q., 2005. Using Landsat ETM+ imagery to measure population density in Indianapolis , USA. Photogrammetric Engineering & Remote Sensing 71, 947–958.

Liang, S., 2001. Narrowband to broadband conversions of land surface albedo I: Algorithms. Remote Sensing of Environment 76, 213–238. https://doi.org/10.1016/S0034-4257(00)00205-4

Lovell, S.T., Taylor, J.R., 2013. Supplying urban ecosystem services through multifunctional green infrastructure in the United States. Landscape Ecology 28, 1447–1463. https://doi.org/10.1007/s10980-013-9912-y

Mackey, C.W., Lee, X., Smith, R.B., 2012. Remotely sensing the cooling effects of city scale efforts to reduce urban heat island. Building and Environment 49, 348–358. https://doi.org/10.1016/j.buildenv.2011.08.004

Magill, A.H., Aber, J.D., Currie, W.S., Nadelhoffer, K.J., Martin, M.E., McDowell, W.H., Melillo, J.M., Steudler, P., 2004. Ecosystem response to 15 years of chronic nitrogen additions at the Harvard Forest LTER, Massachusetts, USA. Forest Ecology and Management 196, 7–28. https://doi.org/10.1016/j.foreco.2004.03.033

Mahadevan, P., Wofsy, S.C., Matross, D.M., Xiao, X., Dunn, A.L., Lin, J.C., Gerbig, C., Munger, J.W., Chow, V.Y., Gottlieb, E.W., 2008. A satellite-based biosphere parameterization for net ecosystem CO_2 exchange: Vegetation Photosynthesis and Respiration Model (VPRM). Global Biogeochemical Cycles 22, GB2005. https://doi.org/10.1029/2006GB002735

Masek, J.G., Vermote, E.F., Saleous, N.E., Wolfe, R., Hall, F.G., Huemmrich, K.F., Gao, F., Kutler, J., Lim, T.-K., 2006. A Landsat surface reflectance dataset for North America, 1990–2000. IEEE Geoscience and Remote Sensing Letters 3, 68–72. https://doi.org/10.1109/LGRS.2005.857030

MassGIS, 2005. MassGIS datalayers. http://www.mass.gov/anf/research- and-tech/it-serv-and- support/application-serv/office-of-geographic-information-massgis/datalayers/layerlist.html

Mays, K.L., Shepson, P.B., Stirm, B.H., Karion, A., Sweeney, C., Gurney, K.R., 2009. Aircraft-based measurements of the carbon footprint of Indianapolis. Environmental Science & Technology 43, 7816–7823.

McDonald, R.I., Kroeger, T., Zhang, P., Hamel, P., 2019. The value of US urban tree cover for reducing heat-related health impacts and electricity consumption. Ecosystems. https://doi.org/10.1007/s10021-019-00395-5

McKain, K., Wofsy, S.C., Nehrkorn, T., Eluszkiewicz, J., Ehleringer, J.R., Stephens, B.B., 2012. Assessment of ground-based atmospheric observations for verification of greenhouse gas emissions from an urban region. Proceedings of the National Academy of Sciences 109, 8423–8428. https://doi.org/10.1073/pnas.1116645109

McPherson, E.G., Peper, P., 2012. Urban tree growth modeling. Journal of Arboriculture & Urban Forestry 38, 175–183.

McPherson, E.G., Qingfu, X., Elena, A., 2013. A new approach to quantify and map carbon stored , sequestered and emissions avoided by urban forests. Landscape and Urban Planning 120, 70–84. https://doi.org/10.1016/j.landurbplan.2013.08.005

McPherson, E.G., Van Doorn, N.S., Peper, P.J., 2016. Urban Tree Database and Allometric Equations. United States Department of Agriculture. https://doi.org/10.2737/RDS-2016-0005

Meehl, G.A., Tebaldi, C., 2004. More intense, more frequent, and longer lasting heat waves in the 21st century. Science 305, 994–997. https://doi.org/10.1126/science.1098704

Melaas, E.K., Wang, J.A., Miller, D.L., Friedl, M.A., 2016. Interactions between urban vegetation and surface urban heat islands: a case study in the Boston metropolitan region. Environmental Research Letters 11, 054020. https://doi.org/10.1088/1748-9326/11/5/054020

Menon, S., Akbari, H., Mahanama, S., Sednev, I., Levinson, R., 2010. Radiative forcing and temperature response to changes in urban albedos and associated CO_2 offsets. Environmental Research Letters 5, 014005. https://doi.org/10.1088/1748-

9326/5/1/014005

Meyer, W.B., 1991. Urban heat island and urban health: Early American perspectives. The Professional Geographer 43, 38–48. https://doi.org/10.1111/j.0033-0124.1991.00038.x

Milesi, C., Running, S.W., Elvidge, C.D., Dietz, J.B., Tuttle, B.T., Nemani, R.R., 2005. Mapping and modeling the biogeochemical cycling of turf grasses in the United States. Environmental Management 36, 426–438. https://doi.org/10.1007/s00267-004-0316-2

Miller, D.L., Roberts, D.A., Clarke, K.C., Lin, Y., Menzer, O., Peters, E.B., McFadden, J.P., 2018. Gross primary productivity of a large metropolitan region in midsummer using high spatial resolution satellite imagery. Urban Ecosystems 21, 831–850. https://doi.org/10.1007/s11252-018-0769-3

Moran, D., Kanemoto, K., Jiborn, M., Wood, R., Többen, J., Seto, K.C., 2018. Carbon footprints of 13,000 cities. Environmental Research Letters 13, 064041. https://doi.org/10.1088/1748-9326/aac72a

Nathan, B.J., Lauvaux, T., Turnbull, J.C., Richardson, S.J., Miles, N.L., Gurney, K.R., 2018. Source sector attribution of CO_2 emissions using an urban CO/CO_2 Bayesian inversion system. Journal of Geophysical Research: Atmospheres 123, 13,611-13,621. https://doi.org/10.1029/2018JD029231

National Solar Radiation Database (NSRDB), 2010. USAF #725090 — Boston Logan International Airport, MA (Class I) http://rredc.nrel.gov/solar/old_data/nsrdb/1991-2010/hourly/siteonthefly.cgi?id=725090

Newman, S., Jeong, S., Fischer, M.L., Xu, X., Haman, C.L., Lefer, B., Alvarez, S., Rappenglueck, B., Kort, E.A., Andrews, A.E., Peischl, J., Gurney, K.R., Miller, C.E., Yung, Y.L., 2013. Diurnal tracking of anthropogenic CO_2 emissions in the Los Angeles basin megacity during spring 2010. Atmospheric Chemistry and Physics 13, 4359–4372. https://doi.org/10.5194/acp-13-4359-2013

Ng, B.J.L., Hutyra, L.R., Nguyen, H., Cobb, A.R., Kai, F.M., Harvey, C., Gandois, L., 2015. Carbon fluxes from an urban tropical grassland. Environmental Pollution 203, 227–234. https://doi.org/10.1016/j.envpol.2014.06.009

Niemelä, J., 2014. Ecology of urban green spaces: The way forward in answering major research questions. Landscape and Urban Planning 125, 298–303. https://doi.org/10.1016/j.landurbplan.2013.07.014

Nowak, D.J., Crane, D.E., Stevens, J.C., Hoehn, R.E., Walton, J.T., Bond, J., 2008. A ground-based method of assessing urban forest structure and ecosystem services. Arboriculture and Urban Forestry 34, 347–358. https://doi.org/10.1039/b712015j

Nowak, D.J., Greenfield, E.J., 2012. Tree and impervious cover in the United States. Landscape and Urban Planning 107, 21–30. https://doi.org/10.1016/j.landurbplan.2012.04.005

Nowak, D.J., Greenfield, E.J., Hoehn, R.E., Lapoint, E., 2013. Carbon storage and sequestration by trees in urban and community areas of the United States. Environmental Pollution 178, 229–236. https://doi.org/10.1016/j.envpol.2013.03.019

O'Brien, A.M., Ettinger, A.K., HilleRisLambers, J., 2012. Conifer growth and reproduction in urban forest fragments: Predictors of future responses to global change? Urban Ecosystems 15, 879–891. https://doi.org/10.1007/s11252-012-0250-7

O'Neil-Dunne, J., 2017. An Assessment of Boston's Tree Canopy, USDA Urban Tree Canopy Assessment.

Odum, E.P., 1969. The strategy of ecosystem development. Science 164, 262–270. https://doi.org/10.1126/science.164.3877.262

Oleson, K.W., Bonan, G.B., Feddema, J., Vertenstein, M., Grimmond, C.S.B., 2008. An urban parameterization for a global climate model. Part I: formulation and evaluation for two cities. Journal of Applied Meteorology and Climatology 47, 1038–1060. https://doi.org/10.1175/2007JAMC1597.1

Ollinger, S. V., Aber, J.D., Reich, P.B., Freuder, R.J., 2002. Interactive effects of nitrogen deposition, tropospheric ozone, elevated CO_2 and land use history on the carbon dynamics of northern hardwood forests. Global Change Biology 8, 545–562. https://doi.org/10.1046/j.1365-2486.2002.00482.x

Olofsson, P., Holden, C.E., Bullock, E.L., Woodcock, C.E., 2016. Time series analysis of satellite data reveals continuous deforestation of New England since the 1980s. Environmental Research Letters In review, 1–8. https://doi.org/10.1088/1748-9326/11/6/064002

Ossola, A., Hopton, M.E., 2018a. Climate differentiates forest structure across a residential macrosystem. Science of the Total Environment 639, 1164–1174. https://doi.org/10.1016/j.scitotenv.2018.05.237

Ossola, A., Hopton, M.E., 2018b. Measuring urban tree loss dynamics across residential landscapes. Science of the Total Environment 612, 940–949. https://doi.org/10.1016/j.scitotenv.2017.08.103

Ouimette, A.P., Ollinger, S. V., Richardson, A.D., Hollinger, D.Y., Keenan, T.F., Lepine, L.C., Vadeboncoeur, M.A., 2018. Carbon fluxes and interannual drivers in a temperate forest ecosystem assessed through comparison of top-down and bottom-up approaches. Agricultural and Forest Meteorology 256–257, 420–430. https://doi.org/10.1016/j.agrformet.2018.03.017

Paembonan, S.A., Hagihara, A., Hozumi, K., 1992. Long-term respiration in relation to growth and maintenance processes of the aboveground parts of a hinoki forest tree. Tree Physiology 10, 21–31. https://doi.org/10.1093/treephys/10.1.101

Pahari, R., Leclerc, M.Y., Zhang, G., Nahrawi, H., Raymer, P., 2018. Carbon dynamics of a warm season turfgrass using the eddy-covariance technique. Agriculture, Ecosystems and Environment 251, 11–25. https://doi.org/10.1016/j.agee.2017.09.015

Pataki, D.E., 2013. Urban greening needs better data. Nature 502, 624.

Pataki, D.E., Alig, R.J., Fung, A.S., Golubiewski, N.E., Kennedy, C.A., McPherson, E.G., Nowak, D.J., Pouyat, R. V., Romero Lankao, P., 2006. Urban ecosystems and the North American carbon cycle. Global Change Biology 12, 2092–2102. https://doi.org/10.1111/j.1365-2486.2006.01242.x

Pataki, D.E., Carreiro, M.M., Cherrier, J., Grulke, N.E., Jennings, V., Pincetl, S., Pouyat, R. V., Whitlow, T.H., Zipperer, W.C., 2011. Coupling biogeochemical cycles in urban environments: Ecosystem services, green solutions, and misconceptions. Frontiers in Ecology and the Environment 9, 27–36. https://doi.org/10.1890/090220

Pataki, D.E., Emmi, P.C., Forster, C.B., Mills, J.I., Pardyjak, E.R., Peterson, T.R., Thompson, J.D., Dudley-Murphy, E., 2009. An integrated approach to improving fossil fuel emissions scenarios with urban ecosystem studies. Ecological Complexity 6, 1–14. https://doi.org/10.1016/j.ecocom.2008.09.003

Patz, J.A., Campbell-Lendrum, D., Holloway, T., Foley, J.A., 2005. Impact of regional climate change on human health. Nature 438, 310–317. https://doi.org/10.1038/nature04188

Peng, S., Piao, S., Ciais, P., Friedlingstein, P., Ottle, C., Bréon, F.-M., Nan, H., Zhou, L., Myneni, R.B., 2012. Surface urban heat island across 419 global big cities. Environmental Science & Technology 46, 696–703. https://doi.org/10.1021/es2030438

Peters, E.B., McFadden, J.P., 2012. Continuous measurements of net CO_2 exchange by vegetation and soils in a suburban landscape. Journal of Geophysical Research: Biogeosciences 117, G03005. https://doi.org/10.1029/2011JG001933

Piao, S., Luyssaert, S., Ciais, P., Janssens, I.A., Cao, C., Fang, J., Friedlingstein, P., Luo, Y., Wang, S., Piao, S., Luyssaert, S., Ciais, P., Janssens, I.A., Chen, A., Cao, C., Fang, J., Friedlingstein, P., Luo, Y., Wang, S., 2010. Forest annual carbon cost: a global-scale analysis of autotrophic respiration. Ecology 91, 652–661.

Pichler, P.P., Zwickel, T., Chavez, A., Kretschmer, T., Seddon, J., Weisz, H., 2017. Reducing urban greenhouse gas footprints. Scientific Reports 7, 14659. https://doi.org/10.1038/s41598-017-15303-x

Pincetl, S., Gillespie, T., Pataki, D.E., Saatchi, S., Saphores, J.D., 2013. Urban tree planting programs, function or fashion? Los Angeles and urban tree planting campaigns. GeoJournal 78, 475–493. https://doi.org/10.1007/s10708-012-9446-x

Polsky, C., Grove, J.M., Knudson, C., Groffman, P.M., Bettez, N., Cavender-Bares, J., Hall, S.J., Heffernan, J.B., Hobbie, S.E., Larson, K.L., Morse, J.L., Neill, C., Nelson, K.C., Ogden, L.A., O'Neil-Dunne, J., Pataki, D.E., Roy Chowdhury, R., Steele, M.K., 2014. Assessing the homogenization of urban land management with an application to US residential lawn care. Proceedings of the National Academy of Sciences 111, 4432–4437. https://doi.org/10.1073/pnas.1323995111

Poorter, H., Niklas, K.J., Reich, P.B., Oleksyn, J., Poot, P., Mommer, L., 2012. Biomass allocation to leaves, stems and roots: meta-analyses of interspecific variation and environmental control. New Phytologist 193, 30–50. https://doi.org/10.1111/j.1469-8137.2011.03952.x

Poudyal, N.C., Siry, J.P., Bowker, J.M., 2010. Urban forests' potential to supply marketable carbon emission offsets: A survey of municipal governments in the United States. Forest Policy and Economics 12, 432–438. https://doi.org/10.1016/j.forpol.2010.05.002

Pouyat, R. V., Yesilonis, I.D., Nowak, D.J., 2006. Carbon storage by urban soils in the United States. Journal of Environment Quality 35, 1566–1575. https://doi.org/10.2134/jeq2005.0215

Pretzsch, H., Biber, P., Uhl, E., Dahlhausen, J., Rötzer, T., Caldentey, J., Koike, T., van Con, T., Chavanne, A., Seifert, T., Toit, B. du, Farnden, C., Pauleit, S., 2015. Crown size and growing space requirement of common tree species in urban centres, parks, and forests. Urban Forestry and Urban Greening 14, 466–479. https://doi.org/10.1016/j.ufug.2015.04.006

Pretzsch, H., Biber, P., Uhl, E., Dahlhausen, J., Schütze, G., Perkins, D., Rötzer, T., Caldentey, J., Koike, T., Con, T. Van, Chavanne, A., Toit, B. Du, Foster, K., Lefer, B., 2017. Climate change accelerates growth of urban trees in metropolises worldwide. Scientific Reports 7, 15403. https://doi.org/10.1038/s41598-017-14831-w

Qian, Y., Follett, R., 2012. Carbon Dynamics and Sequestration in Urban Turfgrass Ecosystems, in: Lal, R., Augustin, B. (Eds.), Carbon Sequestration in Urban Ecosystems. Springer Netherlands, Dordrecht, pp. 161–172. https://doi.org/10.1007/978-94-007-2366-5_8

Qian, Y., Follett, R.F., Kimble, J.M., 2010. Soil organic carbon input from urban turfgrasses. Soil Science Society of America Journal 74, 366–371. https://doi.org/10.2136/sssaj2009.0075

Quigley, M.F., 2004. Street trees and rural conspecifics: Will long-lived trees reach full size in urban conditions? Urban Ecosystems 7, 29–39. https://doi.org/10.1023/B:UECO.0000020170.58404.e9

R Core Team, 2017. R: A language and environment for statistical computing. R Foundation for Statistical Computing, Vienna, Austria. http://www.R-project.org/.

Raciti, S.M., Fahey, T.J., Thomas, R.Q., Woodbury, P.B., Driscoll, C.T., Carranti, F.J., Foster, D.R., Gwyther, P.S., Hall, B.R., Hamburg, S.P., Jenkins, J.C., Neill, C., Peery, B.W., Quigley, E.E., Sherman, R., Vadeboncoeur, M.A., Weinstein, D.A., Wilson, G., 2012a. Local-scale carbon budgets and mitigation opportunities for the northeastern United States. BioScience 62, 23–38. https://doi.org/10.1525/bio.2012.62.1.7

Raciti, S.M., Hutyra, L.R., Finzi, A.C., 2012b. Depleted soil carbon and nitrogen pools beneath impervious surfaces. Environmental Pollution 164, 248–251. https://doi.org/10.1016/j.envpol.2012.01.046

Raciti, S.M., Hutyra, L.R., Newell, J.D., 2014. Mapping carbon storage in urban trees with multi-source remote sensing data: Relationships between biomass, land use, and demographics in Boston neighborhoods. Science of The Total Environment 500–501, 72–83. https://doi.org/10.1016/j.scitotenv.2014.08.070

Raciti, S.M., Hutyra, L.R., Rao, P., Finzi, A.C., 2012c. Inconsistent definitions of “urban” result in different conclusions about the size of urban carbon and nitrogen stocks. Ecological Applications 22, 1015–1035. https://doi.org/10.1890/11-1250.1

Rao, P., Hutyra, L.R., Raciti, S.M., Finzi, A.C., 2013a. Field and remotely sensed measures of soil and vegetation carbon and nitrogen across an urbanization gradient in the Boston metropolitan area. Urban Ecosystems 16, 593–616. https://doi.org/10.1007/s11252-013-0291-6

Rao, P., Hutyra, L.R., Raciti, S.M., Templer, P.H., 2013b. Atmospheric nitrogen inputs and losses along an urbanization gradient from Boston to Harvard Forest, MA. Biogeochemistry 1–17. https://doi.org/10.1007/s10533-013-9861-1

Reinmann, A.B., Hutyra, L.R., 2017. Edge effects enhance carbon uptake and its vulnerability to climate change in temperate broadleaf forests. Proceedings of the National Academy of Sciences 114, 107–112. https://doi.org/10.1073/pnas.1612369114

Reinmann, A.B., Hutyra, L.R., Trlica, A., Olofsson, P., 2016. Assessing the global warming potential of human settlement expansion in a mesic temperate landscape from 2005 to 2050. Science of The Total Environment 545–546, 512–524. https://doi.org/10.1016/j.scitotenv.2015.12.033

Rizwan, A.M., Dennis, L.Y.C., Liu, C., 2008. A review on the generation, determination and mitigation of Urban Heat Island. Journal of Environmental Sciences 20, 120–128. https://doi.org/10.1016/S1001-0742(08)60019-4

Rogan, J., Ziemer, M., Martin, D., Ratick, S., Cuba, N., DeLauer, V., 2013. The impact of tree cover loss on land surface temperature: A case study of central Massachusetts using Landsat Thematic Mapper thermal data. Applied Geography 45, 49–57. https://doi.org/10.1016/j.apgeog.2013.07.004

Roman, L.A., Battles, J.J., McBride, J.R., 2014. The balance of planting and mortality in a street tree population. Urban Ecosystems 17, 387–404. https://doi.org/10.1007/s11252-013-0320-5

Roman, L.A., Pearsall, H., Eisenman, T.S., Conway, T.M., Fahey, R.T., Landry, S., Vogt, J., Doorn, N.S. Van, Grove, J.M., Locke, D.H., Bardekjian, A.C., Battles, J.J., Cadenasso, M.L., Konijnendijk, C.C., Bosch, V. Den, Avolio, M., Berland, A., Jenerette, G.D., Mincey, S.K., Pataki, D.E., Staudhammer, C., van Doorn, N.S., Grove, J.M., Locke, D.H., Bardekjian, A.C., Battles, J.J., Cadenasso, M.L., van den Bosch, C.C.K., Avolio, M., Berland, A., Jenerette, G.D., Mincey, S.K., Pataki, D.E., Staudhammer, C., 2018. Human and biophysical legacies shape contemporary urban forests: A literature synthesis. Urban Forestry and Urban Greening 31, 157–168. https://doi.org/10.1016/j.ufug.2018.03.004

Román, M.O., Gatebe, C.K., Shuai, Y., Wang, Z., Gao, F., Masek, J.G., He, T., Liang, S., Schaaf, C.B., 2013. Use of in situ and airborne multiangle data to assess MODIS- and Landsat-based estimates of directional reflectance and albedo. IEEE Transactions on Geoscience and Remote Sensing 51, 1393–1404. https://doi.org/10.1109/TGRS.2013.2243457

Rosenfeld, A.H., Akbari, H., Bretz, S., Fishman, B.L., Kurn, D.M., Sailor, D., Taha, H., 1995. Mitigation of urban heat islands: materials, utility programs, updates. Energy and Buildings 22, 255–265. https://doi.org/10.1016/0378-7788(95)00927-P

Roy, S., Byrne, J., Pickering, C., 2012. A systematic quantitative review of urban tree benefits, costs, and assessment methods across cities in different climatic zones.

Urban Forestry and Urban Greening 11, 351–363. https://doi.org/10.1016/j.ufug.2012.06.006

Russo, A., Escobedo, F.J., Timilsina, N., Schmitt, A.O., Varela, S., Zerbe, S., 2014. Assessing urban tree carbon storage and sequestration in Bolzano, Italy. International Journal of Biodiversity Science, Ecosystem Services and Management 10, 54–70. https://doi.org/10.1080/21513732.2013.873822

Ryan, M.G., Binkley, D., Fownes, J.H., 1997. Age-related decline in forest productivity: Pattern and process, in: Advances in Ecological Research. pp. 213–262. https://doi.org/10.1016/S0065-2504(08)60009-4

Sargent, M., Barrera, Y., Nehrkorn, T., Hutyra, L.R., Gately, C.K., Jones, T., McKain, K., Sweeney, C., Hegarty, J., Hardiman, B., Wang, J.A., Wofsy, S.C., 2018. Anthropogenic and biogenic CO_2 fluxes in the Boston urban region. Proceedings of the National Academy of Sciences 115, 7491–7496. https://doi.org/10.1073/pnas.1803715115

Schaaf, C.B., Gao, F., Strahler, A.H., Lucht, W., Li, X., Tsang, T., Strugnell, N.C., Zhang, X., Jin, Y., Muller, J.P., Lewis, P., Barnsley, M., Hobson, P., Disney, M., Roberts, G., Dunderdale, M., Doll, C., D'Entremont, R.P., Hu, B., Liang, S., Privette, J.L., Roy, D., 2002. First operational BRDF, albedo nadir reflectance products from MODIS. Remote Sensing of Environment 83, 135–148. https://doi.org/10.1016/S0034-4257(02)00091-3

Schaaf, C., Wang, Z., 2015. MCD43A3 MODIS/Terra+Aqua BRDF/Albedo Daily L3 Global - 500m V006 [data set]. NASA EOSDIS Land Processes DAAC. https://doi.org/10.5067/MODIS/MCD43A3.006

Schimel, D., Hargrove, W., Hoffman, F., MacMahon, J., 2007. NEON: a hierarchically designed national ecological network. Frontiers in Ecology and the Environment 5, 59. https://doi.org/10.1890/1540-9295(2007)5[59:NAHDNE]2.0.CO;2

Searle, S.Y., Turnbull, M.H., Boelman, N.T., Schuster, W.S.F.F., Yakir, D., Griffin, K.L., 2012. Urban environment of New York City promotes growth in northern red oak seedlings. Tree Physiology 32, 389–400. https://doi.org/10.1093/treephys/tps027

Seto, K.C., Guneralp, B., Hutyra, L.R., 2012. Global forecasts of urban expansion to 2030 and direct impacts on biodiversity and carbon pools. Proceedings of the National Academy of Sciences 109, 16083–16088. https://doi.org/10.1073/pnas.1211658109

Short Gianotti, A.G., Getson, J.M., Hutyra, L.R., Kittredge, D.B., 2016. Defining urban, suburban, and rural: a method to link perceptual definitions with geospatial measures of urbanization in central and eastern Massachusetts. Urban Ecosystems

19, 823–833. https://doi.org/10.1007/s11252-016-0535-3

Shuai, Y., Masek, J.G., Gao, F., Schaaf, C.B., 2011. An algorithm for the retrieval of 30-m snow-free albedo from Landsat surface reflectance and MODIS BRDF. Remote Sensing of Environment 115, 2204–2216. https://doi.org/10.1016/j.rse.2011.04.019

Shuai, Y., Schaaf, C.B., Strahler, A.H., Liu, J., Jiao, Z., 2008. Quality assessment of BRDF/albedo retrievals in MODIS operational system. Geophysical Research Letters 35, 1–5. https://doi.org/10.1029/2007GL032568

Small, C., 2006. Comparative analysis of urban reflectance and surface temperature. Remote Sensing of Environment 104, 168–189. https://doi.org/10.1016/j.rse.2005.10.029

Smith, I.A., Dearborn, V.K., Hutyra, L.R., 2019. Live fast, die young: Accelerated growth, mortality, and turnover in street trees. Plos One 14, e0215846. https://doi.org/10.1371/journal.pone.0215846

Sobrino, J.A., Jiménez-Muñoz, J.C., Paolini, L., 2004. Land surface temperature retrieval from LANDSAT TM 5. Remote Sensing of Environment 90, 434–440. https://doi.org/10.1016/j.rse.2004.02.003

Song, J., Du, S., Feng, X., Guo, L., 2014. The relationships between landscape compositions and land surface temperature: Quantifying their resolution sensitivity with spatial regression models. Landscape and Urban Planning 123, 145–157. https://doi.org/10.1016/j.landurbplan.2013.11.014

Steeneveld, G.J., Koopmans, S., Heusinkveld, B.G., Theeuwes, N.E., 2014. Refreshing the role of open water surfaces on mitigating the maximum urban heat island effect. Landscape and Urban Planning 121, 92–96. https://doi.org/10.1016/j.landurbplan.2013.09.001

Strohbach, M.W., Arnold, E., Haase, D., 2012. The carbon footprint of urban green space—A life cycle approach. Landscape and Urban Planning 104, 220–229. https://doi.org/10.1016/j.landurbplan.2011.10.013

Strugnell, N.C., Lucht, W., 2001. An algorithm to infer continental-scale albedo from AVHRR data, land over class, and field observation of typical BRDFs. Journal of Climate 14, 1360–1376. https://doi.org/10.1175/1520-0442(2001)014<1360:AATICS>2.0.CO;2

Sun, R., Chen, L., 2012. How can urban water bodies be designed for climate adaptation? Landscape and Urban Planning 105, 27–33. https://doi.org/10.1016/j.landurbplan.2011.11.018

Taha, H., 2008. Meso-urban meteorological and photochemical modeling of heat island mitigation. Atmospheric Environment 42, 8795–8809. https://doi.org/10.1016/j.atmosenv.2008.06.036

Taha, H., 1997. Urban climates and heat islands: albedo, evapotranspiration, and anthropogenic heat. Energy and Buildings 25, 99–103. https://doi.org/10.1016/S0378-7788(96)00999-1

Takagi, M., Gyokusen, K., 2004. Light and atmospheric pollution affect photosynthesis of street trees in urban environments. Urban Forestry and Urban Greening 2, 167–171. https://doi.org/10.1078/1618-8667-00033

Templer, P.H., Toll, J.W., Hutyra, L.R., Raciti, S.M., 2015. Nitrogen and carbon export from urban areas through removal and export of litterfall. Environmental Pollution 197, 256–261. https://doi.org/10.1016/j.envpol.2014.11.016

Tilman, D., Fargione, J., Wolff, B., D'Antonio, C., Dobson, A., Howarth, R., Schindler, D., Schlesinger, W.H., Swackhamer, D., 2001. Forecasting agriculturally driven global environmental change. Science 292, 281–284. https://doi.org/10.1126/science.1057544

Trlica, A., Hutyra, L.R., Morreale, L.M., Smith, I.A., Reinmann, A.B. 2020. Current and future biomass carbon uptake in Boston's urban forest. Science of the Total Environment (accepted with revisions).

Trlica, A., Hutyra, L.R., Schaaf, C.L., Erb, A., Wang, J.A., 2017. Albedo, land cover, and daytime surface temperature variation across an urbanized landscape. Earth's Future 5, 1084–1101. https://doi.org/10.1002/2017EF000569

Turnbull, J.C., Sweeney, C., Karion, A., Newberger, T., Lehman, S.J., Tans, P.P., Davis, K.J., Lauvaux, T., Miles, N.L., Richardson, S.J., Cambaliza, M.O., Shepson, P.B., Gurney, K., Patarasuk, R., Razlivanov, I., 2015. Toward quantification and source sector identification of fossil fuel CO_2 emissions from an urban area: Results from the INFLUX experiment. Journal of Geophysical Research: Atmospheres 120, 292–312. https://doi.org/10.1002/2014JD022555

Urbanski, S., Barford, C., Wofsy, S., Kucharik, C., Pyle, E., Budney, J., McKain, K., Fitzjarrald, D., Czikowsky, M., Munger, J.W., 2007. Factors controlling CO_2 exchange on timescales from hourly to decadal at Harvard Forest. Journal of Geophysical Research: Biogeosciences 112, 1–25. https://doi.org/10.1029/2006JG000293

U.S. Census, 2010. Cartographic Boundary Shapefiles – Places (Incorporated Places and Census Designated Places). State of Massachusetts. https://www.census.gov/geo/maps-data/data/cbf/cbf_place.html

USDA (United States Department of Agriculture) Forest Service, 2019. Database description and User Guide for Phase 2. https://www.fia.fs.fed.us/library/database-documentation/current/ver80/FIADB%20User%20Guide%20P2_8-0.pdf

United Nations, 2012. World urbanization prospects, the 2011 revision: Highlights. United Nations Department of Economic and Social Affairs, Population Division, New York, NY. http://www.un.org/en/development/desa/publications/ world-urbanization-

prospects-the-2011-revision.html

Vahmani, P., Ban-Weiss, G.A., 2016. Impact of remotely sensed albedo and vegetation fraction on simulation of urban climate in WRF-urban canopy model: A case study of the urban heat island in Los Angeles 121, 1511–1531. https://doi.org/10.1002/2015JD023718

Vahmani, P., Hogue, T.S., 2014. High-resolution land surface modeling utilizing remote sensing parameters and the Noah UCM : a case study in the 4791–4806. https://doi.org/10.5194/hess-18-4791-2014

van Doorn, N.S., McPherson, E.G., 2018. Demographic trends in Claremont California's street tree population. Urban Forestry and Urban Greening 29, 200–211. https://doi.org/10.1016/j.ufug.2017.11.018

Velasco, E., Perrusquia, R., Jiménez, E., Hernández, F., Camacho, P., Rodríguez, S., Retama, A., Molina, L.T., 2014. Sources and sinks of carbon dioxide in a neighborhood of Mexico City. Atmospheric Environment 97, 226–238. https://doi.org/10.1016/j.atmosenv.2014.08.018

Velasco, E., Roth, M., 2010. Cities as net sources of CO_2: Review of atmospheric CO_2 exchange in urban environments measured by eddy covariance technique. Geography Compass 4, 1238–1259. https://doi.org/10.1111/j.1749-8198.2010.00384.x

Walsh, M.J., 2014. Greenovate Boston: 2014 climate action plan update. https://www.boston.gov/sites/default/files/greenovate_boston_2014_cap_update.pdf

Walton, J.T., Nowak, D.J., Greenfield, E.J., 2008. Assessing urban forest canopy cover using airborne or satellite imagery. Arboriculture and Urban Forestry 34, 334–340.

Wang, J.A., Hutyra, L.R., Li, D., Friedl, M.A., 2017. Gradients of atmospheric temperature and humidity controlled by local urban land-use intensity in Boston. Journal of Applied Meteorology and Climatology 56, 817–831. https://doi.org/10.1175/JAMC-D-16-0325.1

Weng, Q., Lu, D., Schubring, J., 2004. Estimation of land surface temperature-vegetation abundance relationship for urban heat island studies. Remote Sensing of Environment 89, 467–483. https://doi.org/10.1016/j.rse.2003.11.005

Wilsey, B.J., Polley, H.W., 2006. Aboveground productivity and root-shoot allocation differ between native and introduced grass species. Oecologia 150, 300–309. https://doi.org/10.1007/s00442-006-0515-z

Windahl, E., de Beurs, K., 2016. An intercomparison of Landsat land surface temperature retrieval methods under variable atmospheric conditions using in situ skin temperature. International Journal of Applied Earth Observation and Geoinformation 51, 11–27. https://doi.org/10.1016/j.jag.2016.04.003

Wood, S.N., 2011. Fast stable restricted maximum likelihood and marginal likelihood estimation of semiparametric generalized linear models. Journal of the Royal Statistical Society B (Statistical Methodology), 73, 3–36.

Wu, C., 2004. Normalized spectral mixture analysis for monitoring urban composition using ETM+ imagery. Remote Sensing of Environment 93, 480–492. https://doi.org/10.1016/j.rse.2004.08.003

Wu, D., Lin, J.C., Fasoli, B., Oda, T., Ye, X., Lauvaux, T., Yang, E.G., Kort, E.A., 2018. A Lagrangian approach towards extracting signals of urban CO_2 emissions from satellite observations of atmospheric column CO_2 (XCO_2): X-Stochastic Time-Inverted Lagrangian Transport model ("X-STILT v1"). Geoscientific Model Development 11, 4843–4871. https://doi.org/10.5194/gmd-11-4843-2018

Wu, J., Bauer, M.E., 2012. Estimating net primary production of turfgrass in an urban-suburban landscape with quickbird imagery. Remote Sensing 4, 849–866. https://doi.org/10.3390/rs4040849

Yan, W.Y., Shaker, A., El-Ashmawy, N., 2015. Urban land cover classification using airborne LiDAR data: A review. Remote Sensing of Environment 158, 295–310. https://doi.org/10.1016/j.rse.2014.11.001

Zalasiewicz, J.A.N., Williams, M., Steffen, W., Crutzen, P., 2010. The new world of the anthropocene. Environmental Science and Technology 44, 2228–2231. https://doi.org/10.1021/es903118j

Zanne, A.E., Lopez-Gonzalez, G., Coomes, D.A.A., Ilic, J., Jansen, S., Lewis, S.L.S.L., Miller, R.B.B., Swenson, N.G.G., Wiemann, M.C.C., Chave, J., 2009. Data from: Towards a worldwide wood economics spectrum. Dryad Digital Repository. Dryad. https://doi.org/10.5061/dryad.234

Zeng, N., Yoon, J., 2009. Expansion of the world's deserts due to vegetation-albedo feedback under global warming. Geophysical Research Letters 36, 1–5. https://doi.org/10.1029/2009GL039699

Zhang, H., Jing, X.M., Chen, J.Y., Li, J.J., Schwegler, B., 2016. Characterizing urban fabric properties and their thermal effect using QuickBird image and Landsat 8 thermal infrared (TIR) data: The case of downtown Shanghai, China. Remote Sensing 8, 541. https://doi.org/10.3390/rs8070541

Zhang, X., Friedl, M.A., Schaaf, C.B., Strahler, A.H., Schneider, A., 2004. The footprint of urban climates on vegetation phenology. Geophysical Research Letters 31, 10–13. https://doi.org/10.1029/2004GL020137

Zhao, S., Liu, S., Zhou, D., 2016. Prevalent vegetation growth enhancement in urban environment. Proceedings of the National Academy of Sciences 113, 201602312. https://doi.org/10.1073/pnas.1602312113

Zhao, T., Brown, D.G., Bergen, K.M., 2007. Increasing Gross Primary Production (GPP) in the urbanizing landscapes of southeastern Michigan. Photogrammetric Engineering & Remote Sensing 73, 1159–1167. https://doi.org/10.14358/PERS.73.10.1159

Zhao, T., Brown, D.G., Fang, H., Theobald, D.M., Liu, T., Zhang, T., 2012. Vegetation productivity consequences of human settlement growth in the eastern United States. Landscape Ecology 27, 1149–1165. https://doi.org/10.1007/s10980-012-9766-8

Zheng, B., Myint, S.W., Fan, C., 2014. Spatial configuration of anthropogenic land cover impacts on urban warming. Landscape and Urban Planning 130, 104–111. https://doi.org/10.1016/j.landurbplan.2014.07.001

Zhou, D., Zhao, S., Liu, S., Zhang, L., Zhu, C., 2014. Surface urban heat island in China's 32 major cities: Spatial patterns and drivers. Remote Sensing of Environment 152, 51–61. https://doi.org/10.1016/j.rse.2014.05.017

Zhou, W., Fisher, B., Pickett, S.T., 2019. Cities are hungry for actionable ecological knowledge. Frontiers in Ecology and the Environment 17, 135–135. https://doi.org/10.1002/fee.2021

Zhou, X., Wang, X., Tong, L., Zhang, H., Lu, F., Zheng, F., Hou, P., Song, W., Ouyang, Z., 2012. Soil warming effect on net ecosystem exchange of carbon dioxide during the transition from winter carbon source to spring carbon sink in a temperate urban lawn. Journal of Environmental Sciences (China) 24, 2104–2112. https://doi.org/10.1016/S1001-0742(11)61057-7

Zhu, Z., Wang, S., Woodcock, C.E., 2015. Improvement and expansion of the Fmask algorithm: cloud, cloud shadow, and snow detection for Landsats 4–7, 8, and

Sentinel 2 images. Remote Sensing of Environment 159, 269–277. https://doi.org/10.1016/j.rse.2014.12.014

Ziter, C.D., Pedersen, E.J., Kucharik, C.J., Turner, M.G., 2019. Scale-dependent interactions between tree canopy cover and impervious surfaces reduce daytime urban heat during summer. Proceedings of the National Academy of Sciences 116, 7575–7580. https://doi.org/10.1073/pnas.1817561116

Zurr, A., Ieno, E.N., Walker, N., Savliev, A.A., Smith, G.M., 2009. Mixed Effects Models and Extensions in Ecology with R. Springer Science+Business Media, LLC. https://doi.org/10.1007/978-0-387-87458-6_19

CURRICULUM VITAE

[redacted]

[redacted]

[redacted]

[redacted]

[redacted]